

**Investigation into the Formation of Nanoparticles of Tetravalent Neptunium in Slightly  
Alkaline Aqueous Solution**

# **DISSERTATION**

**Zur Erlangung des akademischen Grades**

**Doktor rerum naturalium**

**(Dr. rer. nat.)**

**vorgelegt**

**der Fakultät Mathematik und Naturwissenschaften**

**der Technischen Universität Dresden**

**von**

**Richard Husar**

**Geboren am 02.11.1985 in Dresden**

**Eingereicht am: 07.07.2015**

**Die Dissertation wurde in der Zeit von Juni 2011 bis Dezember 2014 am  
Helmholtz-Zentrum Dresden-Rossendorf, Institut für  
Ressourcenökologie, angefertigt.**



Gutachter: Prof. Dr. Thorsten Stumpf  
Prof. Dr. Alexander Eychmüller

Tag der Verteidigung: 20.08.2015



## Kurzfassung

Die Errichtung von geologischen Tiefenlagern stellt eine weltweit verfolgte Strategie zur Verwahrung hochradioaktiver Abfälle dar. Auf Grund der Toxizität in diesen Abfällen enthaltenen langlebigen Radionuklide ist eine Sicherheitsanalyse über einen Zeitraum von mehreren Hunderttausend Jahren notwendig. Im Falle des Radionuklids  $^{237}\text{Np}$  mit einer Halbwertszeit von  $2.14 \cdot 10^6$  Jahren sind daher grundlegende Kenntnisse über dessen Migrationspotential insbesondere unter aquatischen Umweltbedingungen nötig. Im Nah-Feld eines Endlagers, wo überwiegend reduzierende Bedingungen angenommen werden müssen, ist dabei das Migrationsverhalten von vierwertigen Np von besonderem Interesse. Auf Grund der geringen Löslichkeiten ( $\sim 10^{-8}$  M) von Np(IV) Verbindungen wurde bislang die Mobilität dieses Ions in wässrigen Systemen überwiegend als sehr gering eingeschätzt. In Feldstudien konnte jedoch für Actinid(IV)-Verbindungen eine erhöhte, meist durch kolloidalen Transport induzierte Mobilität nachgewiesen werden, was weitergehende Untersuchungen zu Bildungsmechanismen von kolloidalen Actinid-Systemen und deren Verhalten unter umweltrelevanten Bedingungen erfordert.

Die vorliegende Studie befasst sich daher mit der Bildung von Np(IV) Nanopartikeln in schwach-alkalischem Milieu unter Karbonat-haltigen Bedingungen wie sie im Nah-Feld eines zukünftigen Endlagers auftreten können. Des weiteren wird der Einfluss von ubiquitär auftretendem Silikat auf das Präzipitationsverhalten von Np(IV), sowie die Bildung von Np(IV)-Silikat-Kolloiden untersucht.

Die Bildung von nanokristallinem  $\text{NpO}_2$  wird durch die Dissoziation des Komplexes  $[\text{Np(IV)(CO}_3)_5]^{6-}$  in wässriger Phase durch einfaches Verdünnen induziert. Mittels hochauflösender Transmissionselektronenmikroskopie (HR-TEM) konnte eine Fluoritstruktur (Raumgruppe  $Fm\bar{3}m$ ) und eine durchschnittliche Partikelgröße von 4 nm der erhaltenen Nanokristalle nachgewiesen werden, welche *in situ* zu Aggregaten mit einem Durchmesser im Mikrometerbereich agglomerieren können. In Lösung wurde zudem die Existenz vereinzelter Aggregate kleinerer Dimensionen ( $\sim 12$  nm) bestätigt, die sich aus bis zu fünf Nanokristall-Einheiten zusammensetzen. Das intensive Agglomerationsverhalten wird durch einen Mangel an effektiver Oberflächenladung (Zetapotential  $\zeta \sim 0$  mV) bei einem Isoelektrischen Punkt ( $\text{pH}_{\text{IEP}}$ ) von  $\text{pH}_{\text{IEP}} 8$  begünstigt. Zudem konnten Hinweise auf polynukleare Np(IV)-Verbindungen als Vorstufe der  $\text{NpO}_2$ -Nanokristall-Bildung beobachtet werden, deren Struktur bisher unbekannt ist.

In Gegenwart von Silikat wird die Bildung von nanokristallinem  $\text{NpO}_2$  durch die Bildung von Np(IV)-Silikat-Partikel unterbunden. Dafür formieren sich hierbei – in Abhängigkeit des molaren Si/Np-Verhältnis – Np(IV)-Silikat-Partikel unterschiedlicher Morphologie und



kolloidalen Stabilität. Bei einem initialen Si/Np-Verhältnis von  $\sim 2$ , präzipitiert Np(IV) gemeinsam mit Silikat als Partikel von der Größe  $>1 \mu\text{m}$ , welche aus unregelmäßig quervernetzten Np(IV)-Silikat-Kompartimenten mit Porengrößen von  $\sim 2\text{-}15 \text{ nm}$  bestehen. Aufgrund gering ausgeprägter effektiver Oberflächenladung und einem  $\text{pH}_{\text{IEP}} \sim 6$ , sind diese Partikel nicht als Kolloid-Dispersion stabilisiert und sedimentieren innerhalb von 1 Monat. Bei einem deutlich höheren Si/Np-Verhältnis von  $\sim 9$ , entstehen dagegen Np(IV)-Silikat-Kolloide mit einer durchschnittlichen Partikelgröße von  $\sim 45 \text{ nm}$ , welche auch über einen längeren Zeitraum ( $>1 \text{ Jahr}$ ) nicht sedimentieren. Diese Kolloide mit amorpher Partikelstruktur sind durch eine geschlossene Oberfläche charakterisiert, an der möglicherweise Silikate adsorbiert werden können. Mittels Röntgenabsorptionsspektroskopie (EXAFS) wurde der Einbau von Si in diese Kolloide mit einem Np-Si Abstand zu  $\sim 3.1 \text{ \AA}$  in der Partikelstruktur bestimmt.

Neben der nanoskaligen Größe und Form spielt für die kolloidale Stabilisierung dieses Np(IV)-Silikat-Systems die effektive hydrodynamische Oberflächenladung eine entscheidende Rolle: aufgrund von Silikat-Anreicherung sind diese Partikel – vergleichbar zu kolloidalem  $\text{SiO}_2$  – zwischen pH 5 und pH 9 mit signifikant negativer Oberflächenladung ( $\zeta = (-) 15$  bis  $(-) 24 \text{ mV}$ ) und einem  $\text{pH}_{\text{IEP}}$  von 2.6 elektrostatisch in Dispersion stabilisiert. Damit können diese Partikel unter umweltrelevanten Grundwasserbedingungen potentiell langzeit-stabile Kolloid-Dispersion erzeugen. In Alterungsversuchen wurde die partielle Bildung von kristallinen Np-Oxidverbindungen innerhalb der amorphen Np(IV)-Silikat-Matrix beobachtet, was auf ein dynamisches System hindeutet.

Die vorliegende Arbeit demonstriert, dass in Gegenwart von Silikat das Hydrolyseverhalten von Np(IV) signifikant beeinflusst wird: beim Überschreiten der Löslichkeitsgrenze von Np(IV) ( $<10^{-8} \text{ M}$  in ultrapurem Wasser) um den Faktor 10.000 kann Silikat vierwertiges Np im wassergetragenen Zustand mit Konzentration zu  $[\text{Np}] = 1 \cdot 10^{-3} \text{ M}$  in Form von Np(IV)-Silikat-Kolloiden stabilisieren. Das Generieren von Np(IV)-Nanopartikel, das durch Verdünnung von Np(IV)-Karbonat-Lösung induziert werden kann, skizziert somit einen potentiellen Grenzfall der Freisetzung von Np aus einem nuklearen Endlager unter den vorherrschenden Umweltbedingungen: den aquatischen Transport von der zementhaltigen geotechnischen Barriere mit ihren alkalischen Bedingungen im Nah-Feld hin zu eher pH neutralen, niederkonzentrierten Bedingungen im Fern-Feld. Damit wird ein potentielles Migrationsverhalten von Np(IV) in geologischen Tiefenlagern beschrieben. Zudem liefern die hier erbrachten Nachweise der intrinsischen Bildung von sowohl nanokristallinen  $\text{NpO}_2$  im Np(IV)-Karbonat-System als auch von Np(IV)-Silikat-Kolloiden im ternären Np(IV)-Silikat-Karbonat-System wichtige Hinweise für kolloid-induzierte Transportmechanismen von Actiniden unter Umweltbedingungen, die es in einem noch zu erbringenden Langzeitsicherheitsnachweis für ein Endlager zu berücksichtigen gilt.





---

## Contents

<b>LIST OF ABBREVIATIONS AND SYMBOLS.....</b>	<b>III</b>
<b>1 Introduction and Objectives.....</b>	<b>1</b>
1.1 Introduction.....	1
1.2 Solution and solid-state structure of An(IV) hydrates and An(IV) colloids.....	3
1.3 Research aspects and objectives.....	5
<b>2 Stabilization of Np(IV) in aqueous solution at near-neutral pH.....</b>	<b>7</b>
<b>3 The Np(IV)-carbonate system.....</b>	<b>13</b>
3.1 Local structure of Np(IV) in carbonate solution.....	14
3.2 Morphology of Np(IV) precipitate at near-neutral pH.....	19
3.3 Electronic structure of Np(IV) precipitate obtained at near-neutral pH.....	22
3.4 Insights into the formation of NpO <sub>2</sub> nanocrystals.....	26
3.4.1 <i>In situ</i> monitoring of the Np(IV) hydrolysis and agglomeration of NpO <sub>2</sub> nanocrystals.....	26
3.4.2 Oligomeric Np(IV) species in the sub-nanometer scale as intermediate structures of NpO <sub>2</sub> cluster formation.....	33
3.4 Implication of the intrinsic formation of NpO <sub>2</sub> NCs under ambient conditions.....	36
<b>4 The Np(IV)-silicate system in bicarbonate solution.....</b>	<b>40</b>
4.1 Precipitation of Np(IV) silica particles versus silicate polymerization.....	40
4.2 Influence of the initial silica concentration in solution on resulting Np(IV) silica colloid characteristics.....	42
4.2.1 Chemical composition of Np(IV) silica particles.....	42
4.2.2 Particle growth behavior and long-term stability.....	43
4.2.3 Colloidal stability of Np(IV) particles in dependence on silica incorporation into the solid phase.....	49
4.3 Internal structure of Np(IV) silica nanoparticles.....	52
4.4 Electronic structure of long-term stabilized Np(IV) silica colloids.....	55
4.5 Morphology of Np(IV) silica colloids.....	58
4.5.1 Effect of initial silica concentration on the morphology of Np(IV) silica colloids.....	58
4.5.2 Morphology of long-term stabilized Np(IV) silica colloids.....	63
4.6 The stabilization of Np(IV) silica colloids - Implication for potential migration behavior of An(IV) 67	
<b>5 Summary.....</b>	<b>68</b>
<b>6 Experimental details.....</b>	<b>70</b>
6.1 Solutions.....	70
6.1.1 Neptunium stock solutions.....	70
6.1.2 Silicate stock solution.....	72
6.1.3 Np(IV) silicate samples.....	72
6.1.3.1 Np(IV) silica colloids above the MWSA.....	72
6.1.3.2 Np(IV) silica colloids below the MWSA.....	72
6.2 Chemical and physical characterization of solutions, colloidal solutions and isolated nanoparticles.....	73
6.2.1 Electrolysis setup - electrochemical preparation of Np solutions.....	73
6.2.2 UV-vis spectroscopy.....	74

---

6.2.3	Photon correlation spectroscopy – particle size distribution in solution.....	74
6.2.4	Laser Doppler velocimetry – determination of particle surface charge at the shear plane.....	74
6.2.5	Transmission electron microscopy .....	76
6.2.6	X-ray absorption spectroscopy - neptunium valency and internal structure .....	76
6.2.7	X-ray photoelectron spectroscopy – binding energies of Np and oxygen core levels .....	79
6.2.8	Element analysis .....	80
6.2.9	Determination pH and $E_h$ .....	80
<b>Appendix.....</b>		<b>81</b>
<b>References.....</b>		<b>84</b>
<b>List of Figures.....</b>		<b>94</b>
<b>List of tables.....</b>		<b>97</b>
<b>Publications .....</b>		<b>98</b>
<b>Acknowledgements .....</b>		<b>99</b>
<b>Versicherung .....</b>		<b>101</b>

---

## LIST OF ABBREVIATIONS AND SYMBOLS

a.u.	arbitrary units
BE	binding energy
CE	counter electrode
CN	coordination number
DLVO	Derjaguin-Landau-Verwey-Overbeek
An(IV)	tetravalent actinide
EDX	energy-dispersive X-ray spectroscopy
EFTEM	energy-filtered transmission electron microscopy
eV	electron volt
EXAFS	extended X-ray absorption fine structure
$E_0$	threshold energy of absorption edge
$E_h$	redox potential
fcc	face centered cubic
FT	fourier transformation
FFT	fast fourier transformation
FWHM	full width on the half-maximum
HAADF-STEM	high-angle annular dark-field scanning transmission electron microscopy
HLW	high-level waste
HOPG	highly ordered pyrolytic graphite
HR-TEM	high-resolution transmission electron microscopy
HZDR	Helmholtz-Zentrum Dresden-Rossendorf
ICP-MS	inductively coupled plasma – mass spectrometry
ICSD	inorganic crystal structure database
IEP	isoelectric point
K	Kelvin
kcps	kilo counts per second
KURT	KAERI underground research tunnel (Korea)
LDV	laser-Doppler-velocimetry
LSC	liquid scintillation counting
M	molar
MA	minor actinide
MOX	mixed oxide (Pu, U)O <sub>2</sub>
MWSA	mononuclear wall of silicic acid
NCs	nanocrystals
Np	neptunium
PCS	photon correlation spectroscopy
PSD	particle size distribution
RT	room temperature
SAED	selected area electron diffraction
SLI	scattered light intensity
$S_0^2$	amplitude reduction factor
t	time
T	temperature
$T_{1/2}$	half-life
TEM	transmission electron microscopy
UC	ultracentrifugation
UF	ultrafiltration
UPS	ultraviolet photoelectron spectroscopy
UV-vis	ultraviolet-visible spectroscopy

---

WE	working electrode
XAS	X-ray absorption spectroscopy
XANES	X-ray absorption near edge structure
XPS	X-ray photoelectron spectroscopy
$\chi(E), \chi(k)$	EXAFS structure function in energy and in wavenumber
$\chi_{\text{red}}^2$	reduced chi-squared value
$\delta(k)$	total phase shift
$\sigma^2$	local disorder of neighbor atoms, Debye-Waller factor
$\zeta$	zeta potential

---

# 1 Introduction and Objectives

## 1.1 Introduction

Conventional nuclear energy is inevitably accompanied by a long-lasting radioactivity inventory of spent fuel from nuclear power plants. After the decay of short-lived fission products, i.e.,  $^{90}\text{Sr}$  and  $^{137}\text{Cs}$ , the major radioactivity is attributed to transuranic elements, i.e., actinide isotopes  $^{237}\text{Np}$ ,  $^{239,240}\text{Pu}$ , and  $^{241,243}\text{Am}$ . [1] Herein, the  $\alpha$ -emitter  $^{237}\text{Np}$  is identified as a key long-term dose contributor to the total radiation in certain nuclear waste repository scenarios due to the long half-life of  $T_{1/2} = 2.14 \cdot 10^6$  a. [2, 3]

The majority of the global inventory of  $^{237}\text{Np}$  is pre-dominantly formed by neutron irradiation of nuclear fuel,  $\text{UO}_2$ , in pressurized water reactors - as a result of successive neutron capture reactions on  $^{235}\text{U}$  and  $^{238}\text{U}$  [4] and as a daughter nuclide of  $^{241}\text{Am}$  ( $T_{1/2} = 432$  a).

Due to the fact that no practical and commercial applications of nearly all inevitably accumulated Np exists [5], it is intended to be incorporated into high-level radioactive waste (HLW) and stored in deep geological disposal sites.

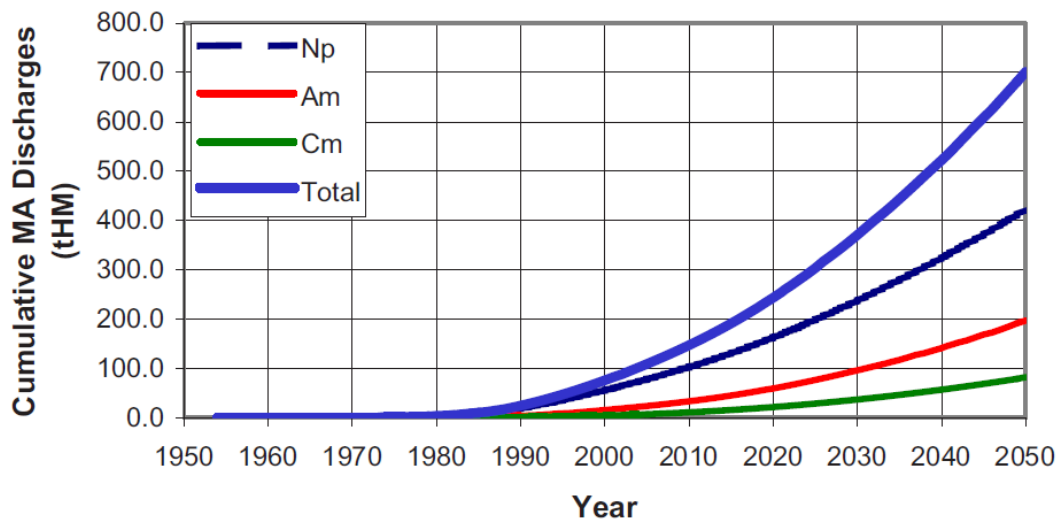


**Figure 1. Worldwide cumulative minor actinide discharges**

tHM = metric tons of heavy metal (figure taken from [6]; estimation based on model in [7]).

Of particular concern, due to long-term radiotoxicity and proliferation risk, is the approximately 1 wt% of spent fuel, composed of plutonium and the minor actinide (MA) isotopes (i.e. Np, Am and Cm). An estimate of the current inventory reveals a future of growth of MA inventory (Figure 1), especially of Np. [6, 7] In the year 2006, it was approximated that about 110 tons of minor actinides were being contained in spent fuel

storage worldwide, and additional 40 tons were contained in HLW products from reprocessing. In the absence of partitioning and transmutation, the amount will double by the year 2020.[6]

Despite the relatively small amount of about ~0.1 wt% in burned fuel,  $^{237}\text{Np}$  will contribute to the radiotoxicity in HLW over long time spans as a consequence of its half-life and play the major role in MA content.[2, 6, 8] The fractional dose attributed to  $^{237}\text{Np}$  will reach 67% within 75,000 a.[4] In addition to the potential radiological hazard, Np is expected to migrate if released into geosphere. Field-testing in the environment of nuclear tests facilities and nuclear reprocessing plants have revealed that  $^{237}\text{Np}$  is mobile in surface water and in groundwater.[5, 9-12] Therefore,  $^{237}\text{Np}$  is the most relevant Np isotope with regards to environmental contamination and long-term safety management.[2, 3, 8]

Concepts of safe HLW storage and economical design of deep geological HLW repository sites are still controversial debated topics. Nevertheless, all countries that developed nuclear fuel cycles focus on a general retention concept of utilizing a multiple barrier system that will be applied for shielding of the nuclear waste. Independent from the host rock formation in which a HLW repository will be implemented the model of the multiple barrier system consists of engineered, geo-engineered, and the geological sub-barriers. The engineered or technical barrier is represented by the conditioned, solidified, and preferably water insoluble waste. It contains highly concentrated actinide waste incorporated in molded silica glass coquilles, placed and filled with concrete in containments of steel or copper. Crushed host-rock material or backfill material, such as bentonite and borehole plugs, will define the geo-engineered barriers and swelling in the case of contact with groundwater, thus, offering an extra seal to minimize radionuclide leakage. The host-rock itself will serve as geological barrier. Possible host rocks for nuclear waste repositories are salt domes (Germany, USA), clay rock (Germany, France, Switzerland, Belgium), and granite (Germany, Sweden, Finland, Canada).

The variety of environmental parameters influencing the redox state and chemical behavior of actinide inventory is extremely complex and dependent on the storage and localization of HLW in the disposal site. The zone surrounding the HLW confined in engineered barriers in geological depths, the so-called near-field (A in Figure 2), is predominantly characterized by reducing anoxic and alkaline conditions. Depending on the site-specific conditions underground water chemistry is subject to variations in bicarbonate concentrations and pH[13-15] e.g. highly concentrated carbonate leakage water (alkaline pH in deep near-field) released from concrete-filling material (i.e., bentonite) which is converted to bicarbonate (near-neutral or slightly alkaline pH in far-field) from the dilution in groundwater flow. Continuous groundwater flows between the saturated (near-field) and unsaturated/vadose zone (far-field) influence the transport potential of actinides into the far-field environment, in soluble form and colloidal forms.[16, 17]

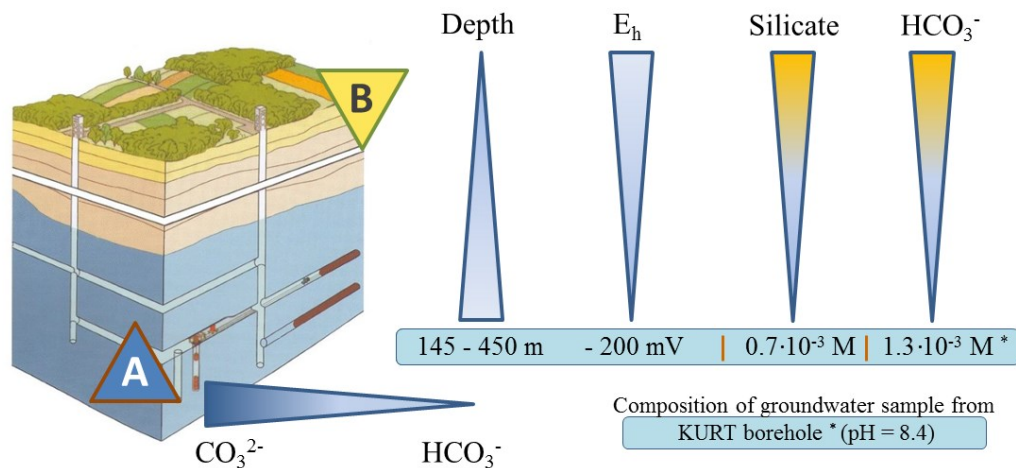


**Figure 2. Schematic illustration of model nuclear waste repository with example of environmental groundwater composition**

(A) anoxic deep zone (near-field) in blue and (B) oxic zone (far-field) in yellow; Ground water composition taken from [14].

The mobility of Np depends on the redox conditions of its environment[18]: Np can exist in several valence states in nature (e.g., III, IV, V, VI, VII) that exhibit remarkable differences in solubility behavior, which can have a dramatic effect on their migration potential.[19] Under oxidizing conditions of natural waters in the far-field (unsaturated zone), the predominant redox state Np(V) is highly mobile in oxygenated surface waters[9-12] due to its high solubility and weak affinity to mineral surfaces.[20] In contrast, under the anoxic and reducing conditions in the unsaturated zone of a near-field, the prevailing redox state of Np is the tetravalent, Np(IV). In general, tetravalent actinides (An(IV)) are considered immobile due to low solubility of An(IV) species and expected to remain as amorphous precipitated An(IV) oxyhydroxides or in the thermodynamically stabilized form of  $AnO_2$ .[15, 21-27]

Nevertheless, field studies of nuclear test sites or nuclear industry sites revealed enhanced actinide transport attributed to colloidal groundwater migration mechanisms[28-30], contradicting underestimated prediction models.[30, 31] Enhanced migration is attributed to the contribution of nanosized An(IV) species or  $AnO_2$  colloids.[30-35]

## 1.2 Solution and solid-state structure of An(IV) hydrates and An(IV) colloids

As a consequence of a highly oxophilic nature, the free single Np(IV) ions undergo hydrolysis with hydroxide ions, or are stabilized via oxygen-bridged complexation, e.g., stable carbonate complexation.[20] Under slightly alkaline conditions, both carbonate and hydroxide strongly interact with actinide ions and could affect the mobility of actinides in natural groundwater systems via ternary complexation.[36] Solution chemistry of the An(IV) system, especially for the

Np carbonate system, is extremely complex[37, 38] and corresponding thermodynamic data widely scattered[14, 36] by i.a. neglecting the formation of polynuclear An(IV) species, as well as colloid formation. New polynuclear An(IV) structures were identified in aqueous solution (Figure 3-(A)): i.e. dihydroxo-bridged ( $\mu_2$ -OH) Th-dimer[39, 40], hexanuclear Np(IV) cluster ( $(\mu_3$ -O)/( $\mu_3$ -OH)-bridged  $\text{Np}_6$  octahedron[41] and exclusively oxobridged  $\text{Pu}_{38}\text{O}_{64}^{+x}$  cluster[39, 42].

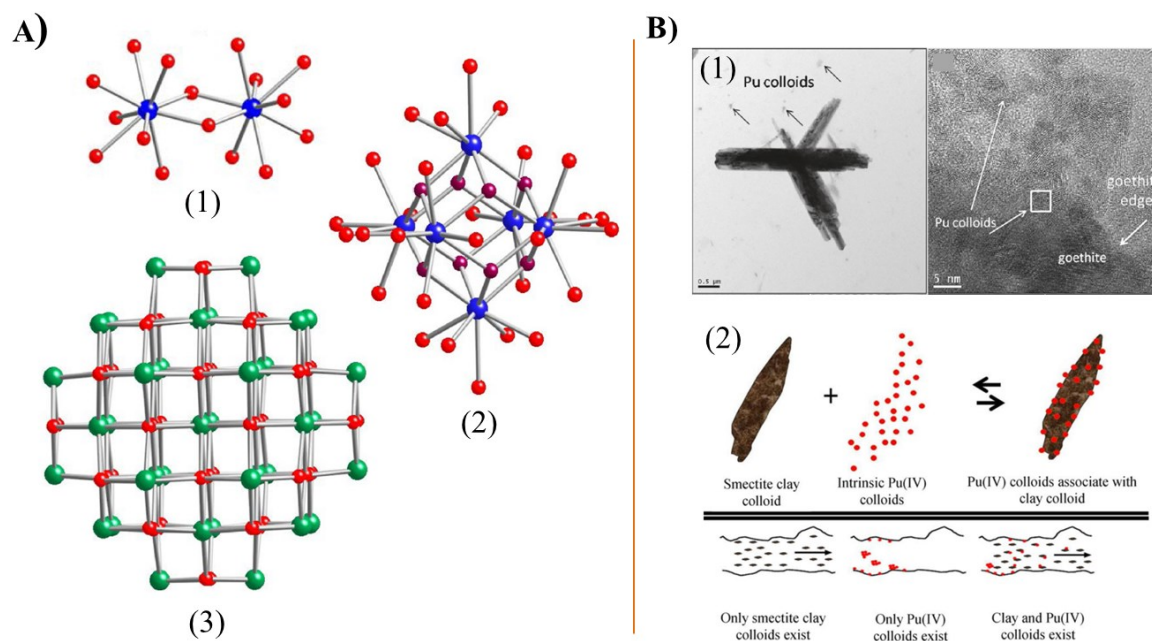


**Figure 3. An(IV) cluster structures (A) and An(IV) colloids (B) in the nanoscale.**

(A) structures of Th(IV) dimer (1), Np(IV) hexanuclear cluster (2) and  $\text{Pu}_{38}\text{O}_{64}^{+x}$  cluster (3) from [39];(B) TEM data of intrinsic fcc  $\text{PuO}_2$  nanocolloids and goethite (1) from [33] and schematic illustration of Pu(IV) pseudo-colloid stabilization with smectite clay colloids (2) from [43].

In the case of Np(IV), the fundamental understanding of its molecular solubility mechanisms and reactivity under slightly alkaline pH is incomplete, and data about the actual neptunium migration fate is scarce.[44, 45] In colloidal field tests, Np was determined to be mobile due to interactions with bentonite colloids as pseudo-colloids.[46] The carrier- or pseudo-colloids consist of mineral fragments of crystalline or amorphous solids that the particular element may be attached.[47] It was found by TEM that highly ordered fcc  $\text{PuO}_2$  nanoparticles (2-5 nm in size) were located on goethite mineral surfaces (Figure 3-(B1)).[33] The effective particle surface charge impacts Pu(IV) stability in suspension, negatively charged smectite colloids from Nevada test site coexists with weak positively charged intrinsic Pu(IV) particles. This emphasizes the expected An(IV) pseudo-colloid transport mechanism as illustrated in Figure 3-(B2).[43]

Regarding interactions with environmental compounds, an An(IV) release from HLW engineered barriers toward near-field aquifer conditions would be accompanied with the ubiquitous occurrence of silicate concentration up to  $2 \cdot 10^{-3}$  M[48] and a pH change towards near-neutral



conditions in solution (Figure 2). In consideration of silicate in solution, the formation of a new type of An(IV) colloids was observed: the An(IV) silica colloids.[49, 50] Metastable Th(IV) or U(IV) silica colloids are formed with silica in aqueous solution at  $\text{pH} > 7$ . Extended X-ray absorption fine structure (EXAFS) confirmed that An-O-Si bonds replace An-O-U bonds in internal particle structure with increasing silicate concentrations in solution. The rising silica content of the particles changes their effective surface charge in solution whereby the particles remain colloidal stabilized in dispersion over years due to electrostatic repulsion.[49]

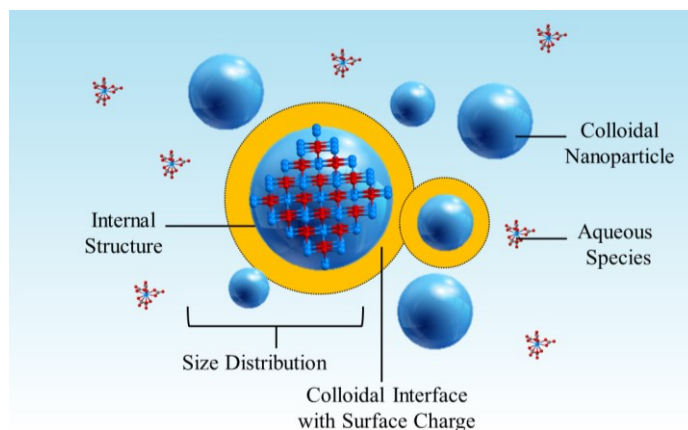


**Figure 4. Schematic illustration of dispersed nanoparticles with selected chemical and physical parameters**

In order to determine the possible impact of colloid facilitated transport as a contribution to the safety assessment of An(IV), knowledge of the key parameters inducing colloid formation and colloid stability is essential. The colloidal appearance of actinide bearing nanoparticles can be regarded as a sensitive counterbalanced ratio of surface net charge, particles size, colloid composition, solution properties and solution viscosity (demonstrated in schematic illustration in Figure 3). These parameters and the actual flow velocity in environmental aquifers control the stability and sorption behavior of colloids and the possible impact of colloid induced transport.[51-54] Therefore, these physicochemical characteristics, the key solution and in the solid state parameters of An(IV) particle stability as colloids at near-neutral pH, are of particular interest. Here within, the present study addresses fundamental factors that govern the stabilization of Np(IV) nanoparticles under ambient conditions in a colloidal borne state.

### 1.3 Research aspects and objectives

For actinides in the tetravalent state, the most significant transport would occur by colloidal particles. With a growing worldwide MA discharge and the current need for geological disposal facilities, this work is timely and focuses on the transport scenario of Np(IV), moving from alkaline cement conditions (near-field) to more neutral environmental conditions (far-field) that

are related to colloid formation. The mechanisms of nanoparticle formation and stabilization in two different environmental systems in solution are of particular interest: (i) in a carbonate environment and (ii) as the silica carbonate system. Thus, a novel isolation route of Np nanoparticles of environmental high relevance was investigated. Neutralization was induced by dilution for modeling environmental conditions as the concentration of radionuclides would decrease as they diffuse away from the site of a leak. By investigating the solubility behavior of Np(IV) after dilution in a simple Np(IV) and carbonate system, the intrinsic formation of nanocrystalline NpO<sub>2</sub> at near-neutral pH was investigated for the first time.

The admixture of silicate into the Np carbonate system simulates the influence of an additional ubiquitously occurring component in groundwater on the Np particle precipitation behavior. It also tests if Np(IV) might be stabilized in the ternary Np, silica and carbonate system as the waterborne form of the recently discovered new type of actinide colloids, the An(IV) silica colloids. Hence, evidence of the formation of Np(IV) silica colloids is the ultimate goal.

In order to understand the key parameters in stabilization of waterborne actinide bearing particles, the chemical and physical properties of Np-nanomaterials and the state of particles in colloidal solutions are of particular interest. The dispersed Np(IV) particles allow for characterization using *in situ* techniques such as photon correlation spectroscopy (PCS) for size calculation with cumulant expansion, and laser Doppler velocimetry (LDV) for characterization of the effective hydrodynamic surface charge at the particle-solution interface.

Transmission electron microscopy (TEM) in combination with energy dispersive X-ray spectroscopy (EDX) were applied to characterize the elemental composition and morphology characteristics in size, shape, and state of the crystallinity of isolated particles. Furthermore, the Np local structure was characterized in terms of the average coordination spheres of Np and its valency by X-ray absorption spectroscopy (XAS), and its electronic structure by determination of Np's core electron binding energies by X-ray photoelectron spectroscopy (XPS). Hints for different electronic structures of Np are derived by UV-vis spectroscopy (UV-vis).

The new insights into the formation of Np(IV) nanoparticles under ambient conditions herein were published in peer-reviewed journals in inorganic chemistry (Chemical Communications; 2015, 51(7): p. 1301-1304., IF<sub>2014</sub> 6.7) and environmental chemistry (Environmental Science and Technology, 2014, 49(1): p. 665-671., IF<sub>2014</sub> 5.4) and presented at actinide conferences and workshops e.g. speech on Migration Conference (2013, Brighton, U.K.), presentation on Plutonium Futures (2014, Las Vegas, U.S.A.), and presentations on Advanced Techniques in Actinide Spectroscopy (2012 and 2014, Dresden, Germany), rewarded with Best Poster Award by selection of the workshop participants.

---

## 2 Stabilization of Np(IV) in aqueous solution at near-neutral pH

As a first step, the environmental conditions, under which Np(IV) colloid formation is obtained, were evaluated. For this purpose, the influence of silica was simulated in model experiments close to near- and far-field scenarios in order to generate Np(IV) colloid formation in solutions of different composition at slightly alkaline pH.

In relevance to the near-field area of nuclear waste disposal sites characterized by an actinide and carbonate-enriched environment, one principle method for colloidal nanoparticle generation was utilized: precipitation by exceeding the solubility limit of the compound concerned. Two related strategies were considered: exceeding the solubility of (i) Np(IV) in dependence on carbonate concentration or of (ii) silica in dependence on its concentration around the mononuclear wall of silicic acid (MWSA) in solution. The MWSA represents the concentration limit above which silicic acid solutions are expected to contain polymers ( $[\text{Si}] \sim 2.5 \cdot 10^{-3} \text{ M}$ ). These polymers are decisive because of their interaction with actinides and the formation of polynuclear species. Typically, metal ions show higher affinities to polysilicic acid than to monosilicic acid.[55, 56]

Due to the fact that carbonate and bicarbonate ions are efficient complexing agents, tetravalent An can exist in the waterborne form in carbonate solutions in the near-field environment.[26, 57-59]

The solubility of Np(IV) in carbonate environments is limited due to two prevailing aqueous species: in low-enriched carbonate solutions, the ternary complex  $\text{Np}(\text{OH})_2(\text{CO}_3)_2^{2-}$  and in carbonate enriched solutions, the dominating binary complex  $\text{Np}(\text{CO}_3)_5^{6-}$ (Figure 5). The latter species was present in the precursor solution used in the model experiments, and the corresponding sample conditions are highlighted by the green dot in Figure 5.

The hydrolysis of the Np(IV) carbonate complex in the precursor solution due to mixing with water was initiated by dilution in the absence or presence of silicate. The formation of a solid phase (Np(IV) nanoparticles) was induced by decreasing the carbonate concentration upon mixing the solutions (conditions of samples revealing colloid formation are highlighted as blue dots in Figure 5). An overview of conditions tested for the absence or presence of Np(IV) colloids in solutions of different composition, based on scattered light intensity (SLI) measurements (nephelometry), is given in Table 1. No silicic acid was added to the solution in the case of Sample 1 that served as a reference sample.

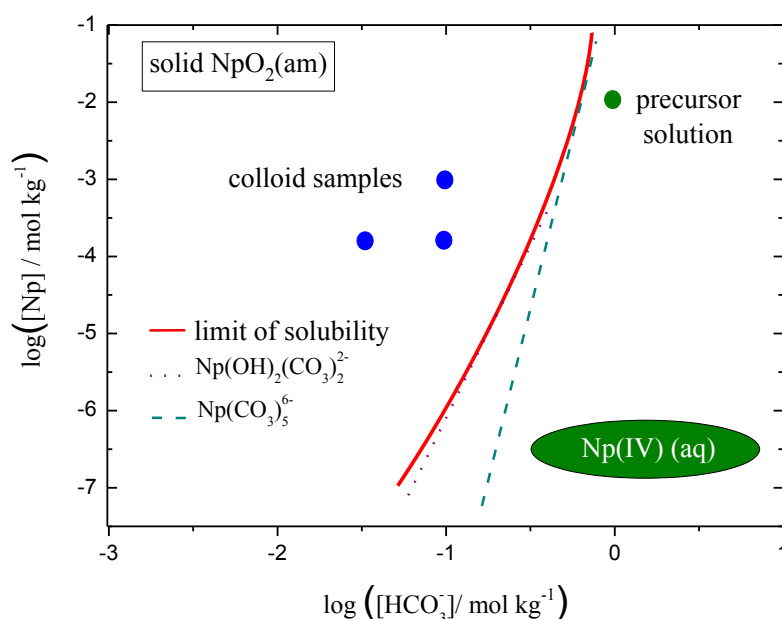


**Figure 5. Solubility of neptunium(IV) in dependence on carbonate/bicarbonate concentration**

Figure is in accordance to the thermodynamic model of  $\text{NpO}_2(\text{am})$  solubility by Rai et al. [26]. The green dot indicates the conditions of the precursor solution before dilution and the blue dots depict conditions of colloidal samples after dilution.

**Table 1. Colloid characterization by nephelometry, ultracentrifugation (5 h,  $100\,000 \times g$ ) and ultrafiltration (5-kDa).**

Sample	Concentration [ $10^{-3}$ M]						pH	Scattered light intensity [kcps] <sup>1</sup>			
	After preparation			After 24 h settling	After UF/UC			After preparation	After acidification	After 24 h settling	After UF/UC
	Np	Si	$\text{HCO}_3^-$	Np	Np	Si					
1	1.4	-	0.1	0.3	$0.3^{\text{UF}}$	n.m.	> 8.5	52	-	12	-
2	1.4	3.0	0.1	1.4	$0.3^{\text{UF}}$	n.m.	> 8.5	200	-	200	-
3	1.4	3.0	1	1.4	$1.3^{\text{UF}}$	n.m.	> 8.5	12	-	12	-
4	0.3	1.5	0.1	n.m.	$<0.1^{2,\text{UF}}$	$1.3^{2,\text{UF}}$	8.0 - 8.5	50	3900	3900	$156^{2,\text{UF}}$
5	0.3	1.5	0.1	n.m.	$<0.2^{2,\text{UC}}$	$1.4^{2,\text{UC}}$	7.0 - 8.0	50	2800	2800	$129^{2,\text{UC}}$

<sup>1</sup> The reference value is the count rate of pure water under the conditions applied ( $\sim 10$  kcps).

<sup>2</sup> These values refer to the acidified sample (see text). n.m. = not monitored, UF = Ultrafiltration, UC = Ultracentrifugation.

Here, the dissociation of the Np(IV) carbonate complexes due to mixing with water (dilution) resulted in the generation of hydrolyzed Np(IV) species forming nanoparticles, which was indicated by parallel detection of increased SLI. Parallel, *in situ* monitoring of the dilution process by UV-vis spectroscopy revealed significant changes in the characteristic spectrum of the original aqueous Np carbonate stock-solution. The characteristic absorption bands of the Np(IV) carbonate complex precursor completely disappeared for the diluted sample (Figure 6-(a) sample 1). A decrease in its characteristic absorption maxima at 584, 704, and 800 nm among other characteristic peaks (shown in Figure 6 and Figure 44) indicated the absence of Np(IV) carbonate species in the diluted sample. The spectrum revealed an absorption maximum at 742 nm (Figure 6-(a) sample 1) indicating the formation of colloidal Np(IV) species[60], which becomes also apparent with a parallel increase in SLI. This slight increase in the SLI was only observed directly after dilution; the nanoparticles settled from the solution and the SLI decreased to the value of pure water within 24 h while the corresponding UV-vis absorbance disappeared (Figure 6-(b) sample 1). Hence, no stable colloidal system was formed. Ultrafiltration, too, removed these Np(IV) particles, which correlates with the disappearance of the corresponding UV-vis absorbance at 742 nm. About 80 wt% of the Np was in a removable form as indicated by liquid scintillation counting (LSC) concentration measurements. The chemical nature of the remaining Np which was not removed after 5-kDa ultrafiltration is unknown.

Samples 2 and 3 refer to the region above the MWSA and they contained  $3 \cdot 10^{-3}$  M silicic acid. The increased SLI and the immediate absorbance at 742 nm of Sample 2 (Figure 6-(a) Sample 2) indicate the formation of colloidal particles. However, these particles did not settle within 24 h, and they could be removed by ultrafiltration through a 5-kDa membrane (also in this case there is an irremovable component of approximately up to 20 wt%, of which the nature is unknown). These results indicate that a relatively stable colloidal solution was formed in Sample 2. On the other hand, in Sample 3 no colloids were formed ;– the SLI was not increased and no Np could be removed by ultrafiltration. This is attributable to the high carbonate concentration of Sample 3 that allows for soluble Np(IV) carbonate complexes, as verified by the characteristic peaks in UV-vis absorbance mentioned above, to remain in solution.

In the samples with Si concentrations below the MWSA (Samples 4 and 5), colloids did not readily form before reducing the pH to less than 8.5. After reducing the pH, however, the SLI rose steeply and the colloids generated did not settle within 24 h. Significant fractions of these colloids were removable by ultrafiltration (Sample 4) or ultracentrifugation (Sample 5). In Sample 4 and Sample 5 at least 80 and 40 wt% of Np could be removed respectively. The similar reduction of the silica concentrations by ultrafiltration and ultracentrifugation indicates that the colloids contain silica, i.e. that these Np(IV) colloids are consistent with previously reported actinide(IV) silica colloids of uranium(IV) and thorium(IV).[49, 50]

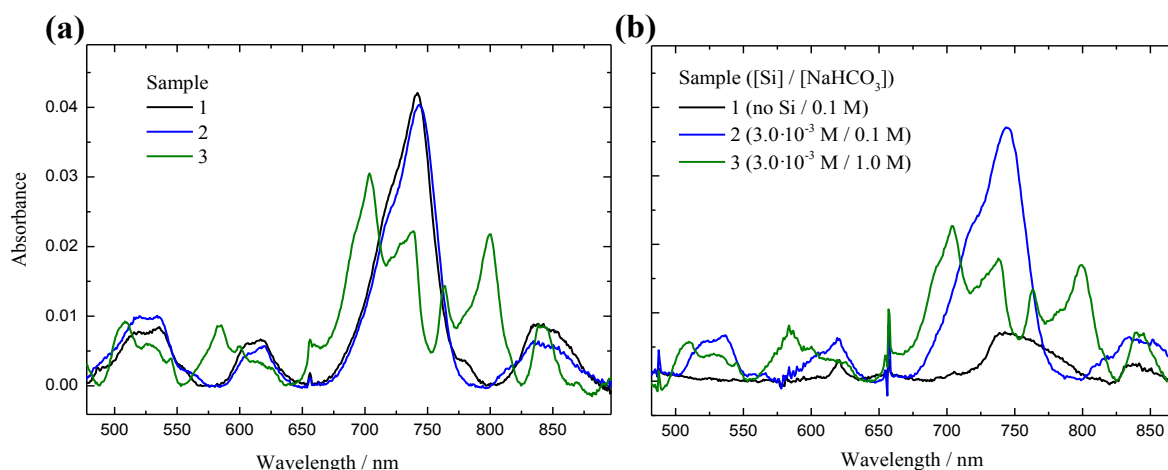


**Figure 6. UV-vis absorbance spectra of  $1.4 \cdot 10^{-3}$  M Np(IV) solutions as a factor of time and carbonate and silicate concentrations**

(a) spectra directly recorded after preparation and (b) spectra recorded after equilibration time of 24 h. Np(IV) samples defined by initial composition: (1) diluted in absence of silicate (0.1 M NaHCO<sub>3</sub>), (2) diluted in presence of silicate ([Si] =  $3.0 \cdot 10^{-3}$  M, 0.1 M NaHCO<sub>3</sub>) and (3) carbonate-rich solution in presence of silicate ([Si] =  $3.0 \cdot 10^{-3}$  M, 1.0 M NaHCO<sub>3</sub>).

Although Sample 2 contained about 5 times more Np(IV) than Samples 4 or 5, the SLI showed much lower values. This is due to the higher concentration of silicic acid in Sample 2. A higher supply of silicic acid during nanoparticle formation results in smaller particle sizes, which reduces the SLI.[49, 50]

Assuming that the density of the silica-containing Np(IV) colloids are similar to those of other actinide silicates, namely coffinite, i.e. of  $5.1 \text{ g cm}^{-3}$ , it can be concluded that the diameters of the particles of the “stable” colloids (Samples 2, 4, and 5 of Table 1) do not exceed 250 nm, otherwise they would have settled due to gravitation. Conversely, the ultracentrifugation experiment on Sample 5 of Table 1 shows that 40 wt% of the colloidal particles must have been larger than about 5 nm because they were removed by a 5 h centrifugation step at  $100\,000 \times g$  (cf. Table 2 in Dreissig et al.).[49] Hence, about 40 wt% of the Np must have occurred as particles of 5 to 250 nm in the solution. The Np fraction that was not removed by the ultracentrifugation step might contain Np monomers (carbonate complexes), Np oligomers and/or lower Np polymers.

The ultrafiltration experiments on the stable colloids of Samples 2 and 4 (cf. Table 1) using 5-kDa membranes indicated that about 80 wt% of the Np in these samples were in a colloid-borne form showing particle sizes between about 2 nm (see ultrafilter pore sizes given in Table 1 of Dreissig et al. [49]) and 250 nm which prevented particles from settling. Thus, the estimates based on both ultracentrifugation and ultrafiltration are in accordance with the particle size results of PCS.

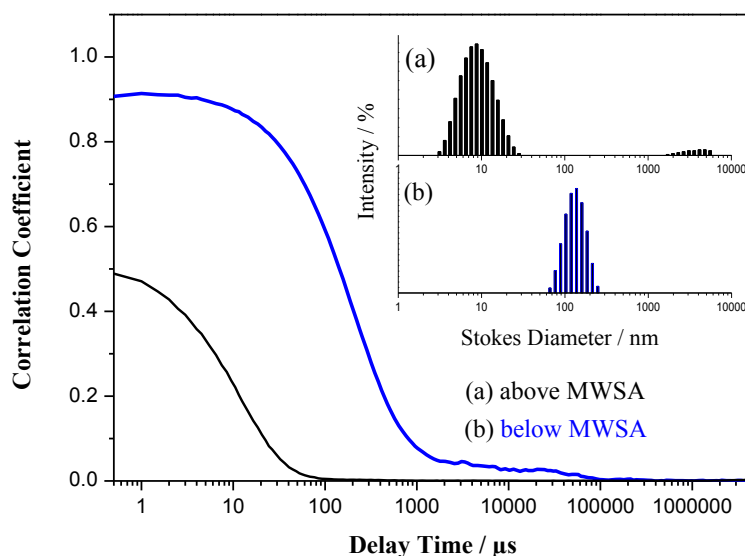


**Figure 7. PCS autocorrelation functions and CONTIN deconvolutions (light-intensity weighted PSD) of Np(IV)-silica colloids**

In the region (a) above the MWSA of silicic acid ( $[\text{Np}] = 1 \cdot 10^{-3} \text{ M}$ ,  $[\text{Si}] = 3 \cdot 10^{-3} \text{ M}$ ,  $0.1 \text{ M NaHCO}_3$ , pH 8–9) and (b) below the MWSA of silicic acid ( $[\text{Np}] = 3.8 \cdot 10^{-4} \text{ M}$ ,  $[\text{Si}] = 1.76 \cdot 10^{-3} \text{ M}$ ,  $0.1 \text{ M NaHCO}_3$ , pH 7–8).

Time-resolved analyses of the SLI by PCS can provide information on the size of the particles.[61-63] Figure 7 displays the autocorrelation functions and their deconvolutions according to the CONTIN routine [64] for two typical samples containing Np(IV)-silica colloids. The samples are similar to Samples 2, 4, and 5, and represent the region (a) above the MWSA (like Sample 2) and (b) below the MWSA (like Samples 4 and 5). The deconvolution accomplished by the respective Malvern software shows either a monomodal light-intensity weighted particle diameter distribution with a median of about 10 nm and a spurious peak or a bimodal particle size distribution (PSD) in the presence of few additional particles (several microns in size) after 24 h (Figure 7-(a)). Both would be in accordance with the study on U(IV)-silica colloids [49]). In addition, a monomodal particle diameter distribution with a median of about 140 nm was found (Figure 7-(b)). Above the MWSA, Np(IV) silica colloids of smaller size are immediately formed, while below the MWSA colloids of larger size are formed after initialization by gradually decreasing the pH.

In conclusion, the test experiments confirmed that an excess of carbonate ( $[\text{carbonate}] = 1.0 \text{ M}$ ) stabilizes Np(IV) as truly soluble Np(IV) carbonate complexes in solution under ambient conditions. Irrespective of the presence of silicate (Sample 3) the prevailing species were identified by UV-vis as Np(IV) carbonate complexes in the ternary system. Dilution of the Np(IV) in absence of silicate leads to destabilization of water-borne Np and precipitation. In contrast, in the

ternary system the presence of silicate stabilizes Np in the water-borne form due to the formation of Np(IV) silica colloids. In both diluted systems the contribution of Np(IV) carbonate complexes was negligible. Next to this there is evidence by light scattering and UV-vis that the hydrolyzed Np(IV) species and the Np(IV) silica colloids reveal characteristic spectral features in the UV-vis spectra that are different from Np(IV) carbonate complexes, but similar to Np(IV) colloids found in presence of humic acids.[60]

The precipitation behavior of the binary Np-carbonate system and the ternary Np-carbonate-silicate system were separately investigated in more detail in the following chapters.



---

### 3 The Np(IV)-carbonate system

The precipitation behavior of Np(IV) as a function of carbonate concentration was further investigated for a comprehensive understanding of hydrolysis, precipitation, and stabilization of Np(IV) under several conditions of interest in this study. The binary system of Np(IV)-carbonate serves as a reference system for the ternary system Np(IV)-silica-carbonate presented in the following chapter 4 of this work. Therefore, the investigation of the structural and physico-chemical characteristics concerning the stability in valency, the structure of the first and second coordination spheres of Np, the electronic structure of Np in the precipitate, and its morphology, were of particular interest. In coherence with this, the *in situ* monitoring of the precipitate formation and of the growth processes in the binary system was of concern to determine the impact of silica during particle formation in the ternary system and its possible implication in an environmental scenario.

For these purposes, the following binary system was investigated as a reference system in further detail in chapter 3: a Np(IV) carbonate stock solution ( $[\text{Np}] = 9.8 \cdot 10^{-3} \text{ M}$  in  $\text{NaHCO}_3$  1.0 M,  $\text{pH} = 9.0$ ) was diluted tenfold with ultrapure water resulting in a colorless solution of  $[\text{Np}] = 1.0 \cdot 10^{-3} \text{ M}$  in 0.1 M  $\text{NaHCO}_3$  with  $\text{pH} = 8.6$ . This solution is similar in composition to Sample 1 of Table 1 of the model experiment that highlights the Np(IV) behavior in carbonate in the absence of silica.

The time-dependent UV-vis spectra of the diluted sample are shown in Figure 8. A tenfold dilution of the Np(IV) carbonate precursor solution with ultrapure water resulted in an immediate spectral change with the emergence of a new absorption maximum at 742 nm, indicating the formation of colloidal Np(IV) species.[60, 65] The diluted Np solution appeared clear for the first few hours after which the formation of slight brownish precipitate occurred (Inset (a) in Figure 8). The re-dispersion of this precipitate in ultrapure water ( $\text{pH} = 7.0$ ) yielded a transparent solution (Inset (b) in Figure 8) although the UV-vis spectrum still showed the characteristic absorption maximum at 742 nm, but with a significant increase in background (solution 3). The observed increase in background can be attributed to the light scattering from small particles, [66] suggesting the formation of Np colloidal particles in solution 3, as confirmed by PCS for Sample 1 in Table 1 with similar composition and behavior. This precipitation-redispersion process was reversible.

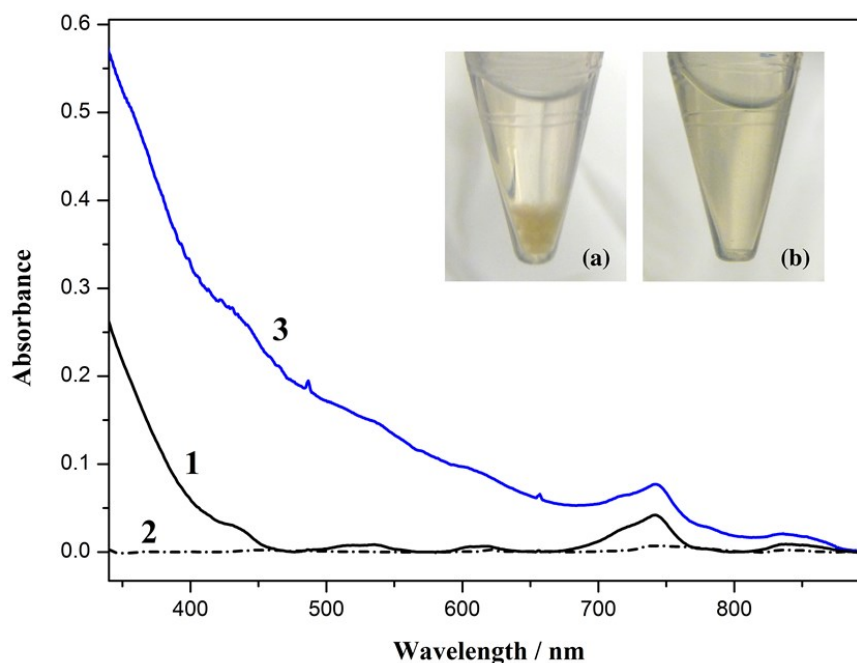


**Figure 8. UV-vis absorption spectra of Np(IV) in diluted carbonate environment and sample appearance in dependence on time**

- (1) Tenfold dilution of Np(IV) stock solution: Initial hydrolyzed Np(IV) – Sample 1,  $[\text{Np}] = 1.0 \cdot 10^{-3} \text{ M}$  in  $\text{NaHCO}_3$  0.1M at  $\text{pH} = 8.6$ ; Spectrum was recorded immediately after dilution
- (2) Supernatant of sample 1 after 24 h and precipitate settling (inset a)
- (3) re-dispersion of the precipitate (inset b) obtained from solution (2) in ultrapure water

### 3.1 Local structure of Np(IV) in carbonate solution

XAS, including both X-ray absorption near-edge structure (XANES) and extended X-ray absorption fine structure (EXAFS), was applied to characterise Np species both in solution and in the solid-state as a factor of varying carbonate concentration. The dilution of the initial Np(IV) solution and the subsequent formation of Np particles resulted in no significant shift in the Np  $L_{\text{III}}$ -edge XANES edge position (Figure 9 and Table 2), suggesting that the tetravalent valence state was preserved and not oxidized to Np(V), even after precipitate formation. The preparation of corresponding samples is given in Table 12 in the experimental section.

Figure 10 shows the  $k^3$  weighted Np  $L_{\text{III}}$ -edge EXAFS spectra (left) and the corresponding Fourier transforms (FTs, right) of the Np stock solution (green), the wet precipitated sample (black) and a  $\text{NpO}_2$  reference powder. The corresponding EXAFS structural parameters obtained from curve fitting are given in Table 3.

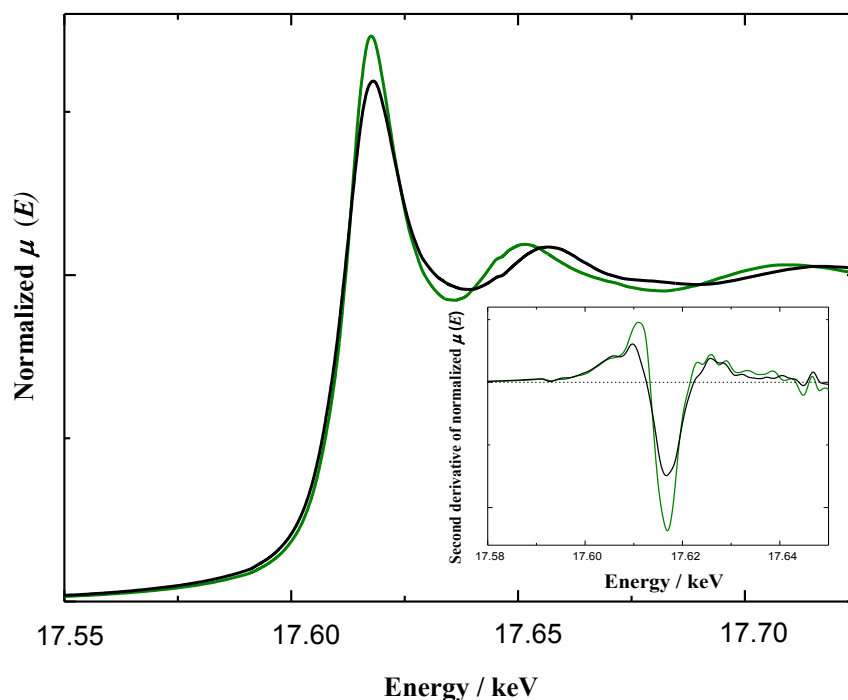


**Figure 9. Normalized Np L<sub>III</sub>-edge XANES spectra for Np(IV) samples**

Aqueous Np(IV) in 1 M NaHCO<sub>3</sub> (green) and wet precipitate obtained by tenfold dilution of the Np(IV) stock solution (black), and their corresponding second derivatives (inset).

**Table 2. XANES edge positions at the Np L<sub>III</sub>-edge for the spectra given in Figure 9 and a Np(V) reference (Figure 49). The edge position is defined at the first inflection point.**

Sample	Edge position / keV
Np(IV) (aq) in 1 M NaHCO <sub>3</sub>	17.6134
Wet precipitate	17.6126
Np(V) (aq) in 1 M HNO <sub>3</sub>	17.6119

In general, the EXAFS oscillation became intricate particularly in the higher  $k$  range when [Np(IV)(CO<sub>3</sub>)<sub>5</sub>]<sup>6-</sup> was transformed into a precipitate by dilution (Figure 10, left). The main oscillation feature of this precipitate resembles that of the one observed for NpO<sub>2</sub>, although the variation of their oscillation amplitude was different (Figure 10). The EXAFS structural parameters obtained for the initial Np(IV) solution in 1 M NaHCO<sub>3</sub> are consistent with a pentacarbonate Np(IV) structure, [Np(IV)(CO<sub>3</sub>)<sub>5</sub>]<sup>6-</sup> (Table 3), the coordination geometry of which is comparable to those reported for [U(IV)(CO<sub>3</sub>)<sub>5</sub>]<sup>6-</sup>[67] and [Pu(IV)(CO<sub>3</sub>)<sub>5</sub>]<sup>6-</sup>[68]. The CO<sub>3</sub><sup>2-</sup> ligands in the stock-solution are coordinated in bidentate-chelating mode [26, 69, 70] and exhibit a Np-O distance of 2.44 Å.

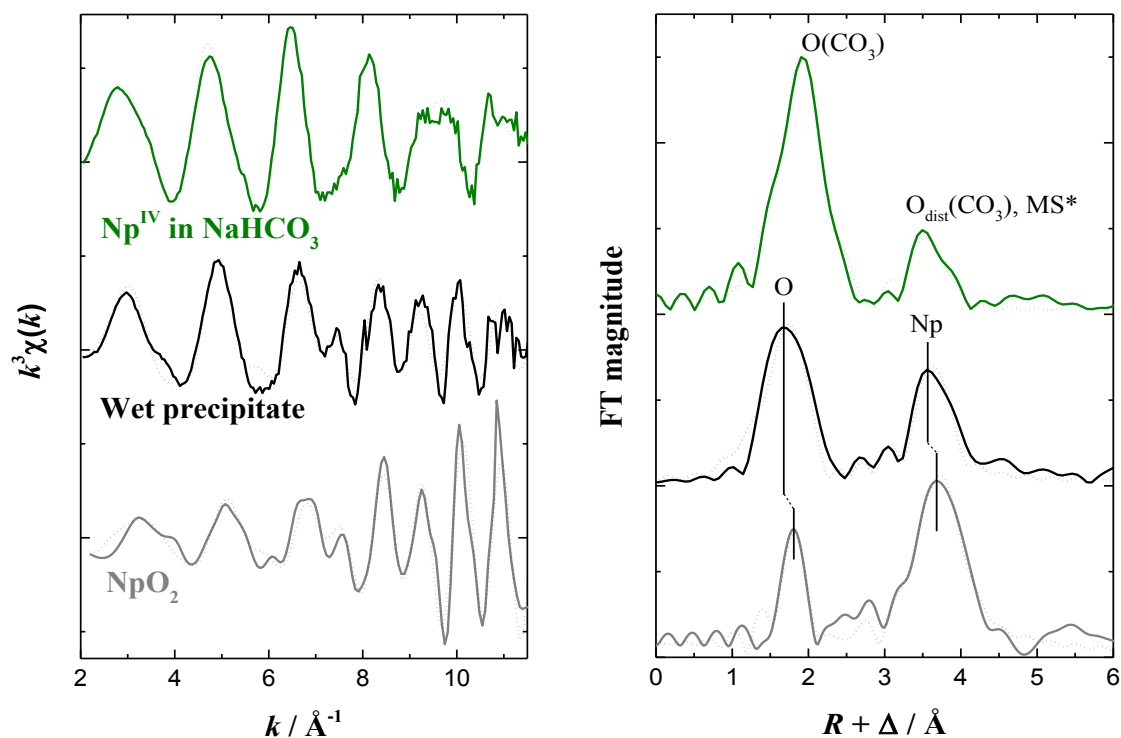


**Figure 10. EXAFS of Np(IV) precursor solution, wet Np(IV) precipitate and NpO<sub>2</sub> powder** (left)  $k^3$ -weighted Np L<sub>III</sub>-edge EXAFS spectra for Np(IV) in 1 M NaHCO<sub>3</sub> at pH = 8.6 (green), a wet precipitate obtained by the dilution of the Np(IV) NaHCO<sub>3</sub> solution with ultrapure water (black) and reference NpO<sub>2</sub> powder (grey), and (right) their corresponding Fourier transforms (FTs). Solid lines, experimental data; dotted lines, theoretical fit; phase shifts ( $\Delta$ ) are not corrected on FTs, MS\*; multiple scattering paths. The magnitude of the data for NpO<sub>2</sub> is reduced by one fourth relative to the  $y$  axes for clear comparison of the spectra.

The linear arrangement of Np, the carbon atom of CO<sub>3</sub><sup>2-</sup>, and its distal oxygen (O<sub>dist</sub>) atom, resulted in a multiple-scattering peak labeled as MS in Figure 10-right. Dilution of the Np(IV) carbonate resulted in a shortening of the Np-O distance in the first shell. Furthermore, a loss of the previously visible O<sub>dist</sub> FT peak and intensification of the FT peak at  $R+\Delta=3.83$  Å were observed. The characteristic strong FT peak at 3.83 Å arising from metal-metal arrangement increases due to intensified Np-Np backscattering. It indicates the growth of Np-Np coordination in exclusively polymeric species and hence the immediate formation of well-ordered NpO<sub>2</sub>-related species. The approximation of the Np-O-bonding in the first shell is reasonably described by splitting into shorter (2.26 Å) and longer (2.39 Å) distanced oxygen bonds. One single Np atom is coordinated with five to six oxygen atoms (respectively two short distanced and up to four longer distanced) and four Np atoms. EXAFS structural analysis reveals that the nearest Np-O and Np-Np interatomic distances obtained for the Np(IV) precipitate are well comparable to those for NpO<sub>2</sub>, whilst the coordination numbers (CNs) for the precipitate are calculated to be much lower with larger Debye-Waller factors ( $\sigma^2$ ) in comparison with those for NpO<sub>2</sub> (Table 3).

**Table 3. EXAFS structural parameters obtained from theoretical curve fitting.**

Sample	Scattering path	$R / \text{\AA}^a$	$CN^b$	$\sigma^2 / \text{\AA}^2$	$\Delta E_{k=0} / \text{eV}$	$F$
Np(IV) (aq) in 1 M NaHCO <sub>3</sub>	Np-O(CO <sub>3</sub> )	2.44	10.2	0.0110	1.4	0.22
	Np-C(CO <sub>3</sub> )	2.86	5.1	0.0069		
	Np-O <sub>dist</sub> (CO <sub>3</sub> )	4.18	4.8	0.0091		
	MS <sup>c</sup> (CO <sub>3</sub> )	4.18	4.8	0.0091		
Wet precipitate of diluted sample (+hydrolyzed Np(IV))	Np-O1	2.26	2.4	0.0071	-7.9	0.25
	Np-O2	2.39	3.6	0.0071		
	Np-Np	3.83	3.6	0.0052		
NpO <sub>2</sub> reference material	Np-O	2.31	8.3	0.0043	0.4	0.76
	Np-Np	3.84	11.8	0.0013		
	Np-O <sub>dist</sub>	4.47	25.3	0.0022		

<sup>a</sup> Interatomic distance ( $R$ ), errors  $\leq \pm 0.02 \text{\AA}$ , <sup>b</sup> Coordination number  $CN$ , errors  $\leq \pm 15\%$ , <sup>c</sup> MS; multiple scattering paths assuming the linear Np-C-O<sub>dist</sub> arrangement.

Similar trends were also observed for UO<sub>2</sub> NCs[71] and a colloidal form of An(IV) oxide/hydroxide species,[72-74] indicating that the formed Np(IV) precipitate could be identified as (i) either small particles of crystalline NpO<sub>2</sub> or (ii) structurally disordered Np(IV) oxide/hydroxide. In case of (i), slightly different or mixed coordination spheres can occur due to a higher ratio of Np atoms located at the surface, relative to the number of Np atoms in the core matrix. The case (ii) would be also acceptable, given that the precipitation of aqueous An(IV) species under circumneutral conditions could also involve the formation of amorphous oxides/hydroxides.[75, 76] These amorphous phases often show a similar EXAFS pattern to those observed for the pure dioxides, but their CNs for the neighbouring coordination shells (*i.e.* nearest An-O and An-An) are calculated to be much smaller than those for the dioxide with larger  $\sigma^2$  values stemming from their amorphism.[72-74]

The CNs and  $\sigma^2$  values obtained for the Np(IV) wet precipitate follow this trend (Table 3).

The Np(IV) precipitate formed in solution could be identified as a mixture of amorphous Np(IV) oxides/hydroxides and nanocrystalline NpO<sub>2</sub>. Only the latter could be further characterised by TEM investigation (cf. section 3.2.). The redispersion of the original precipitate into water removes soluble species/phases from the precipitate, also helping to purify NpO<sub>2</sub> NCs from the amorphous phases. Image acquisition of the redispersed precipitate (Figure 12) was not

affected by the presence of amorphous phases. Another explanation for the lower CNs would be the additional presence of oligomeric Np(IV) species. Note that the wet precipitate sample was measured directly after the precipitation, that was triggered by the dilution of the mother solution without any treatment, such as a washing procedure, drying or purification by filtration. Therefore, the slight contribution of oligomeric Np(IV) species should be considered. Their contribution could also result in lower CNs for the neighbouring coordination shells (nearest An-O and An-An). The possible contribution of small oligomeric Np(IV) species in this study will be demonstrated by HR-TEM in the later section (cf. section 3.4.2.).

Takao and co-workers determined uncharged Np(IV) clusters in a polyhedron configuration: six neighbouring Np atoms connected by two differently distanced O-bridges defining oligomeric Np-O molecules. The reported splitting into short and long distanced O-bonding and increased Np-Np backscattering coincide with the presented findings.[41, 77] Therefore, the consideration of nano- and subnanometer sized clusters is required in the present work. Small polymeric species, e.g. dimeric and trimeric Np(IV) species as indicated by HR-TEM (cf. section 3.2.) are still not identified. The decrease in CNs of the An-An coordination shell in PuO<sub>2</sub> colloids with the fluorite structure was also observed in aging experiments. The decrease of CNs from 3.9 to 1.7 of Pu-Pu of the PuO<sub>2</sub> colloids with ultra-small size was attributed to the formation of small oligomeric plutonium oxide species containing 5 to 6 Pu atoms per polynuclear species.[78]

In summary the calculation of lower CNs for the neighbouring coordination shells (nearest An-O and An-An) of the NpO<sub>2</sub>-like core structure could be influenced by contributions of surface located hydroxyl groups and by the presence of co-precipitated Np(IV) oligomers.

EXAFS results confirmed the dramatic change from the initial Np(IV) carbonate complex to ordered NpO<sub>2</sub>-like structure, which is in accordance with the results from UV-vis absorption spectroscopy (Figure 6; Figure 8; Figure 44).

### 3.2. Morphology of Np(IV) precipitate at near-neutral pH

The Np(IV) precipitate was further characterised by high-resolution TEM (HR-TEM). Figure 11 shows a brightfield TEM micrograph of the precipitate obtained from the Solution 3 in Figure 8, implicating the settled Np(IV) precipitate formed after dilution and redispersion in water. The precipitate appears as fragmented particles in the micrometer-size range (length of particle  $\sim 1.2 \mu\text{m}$ ).

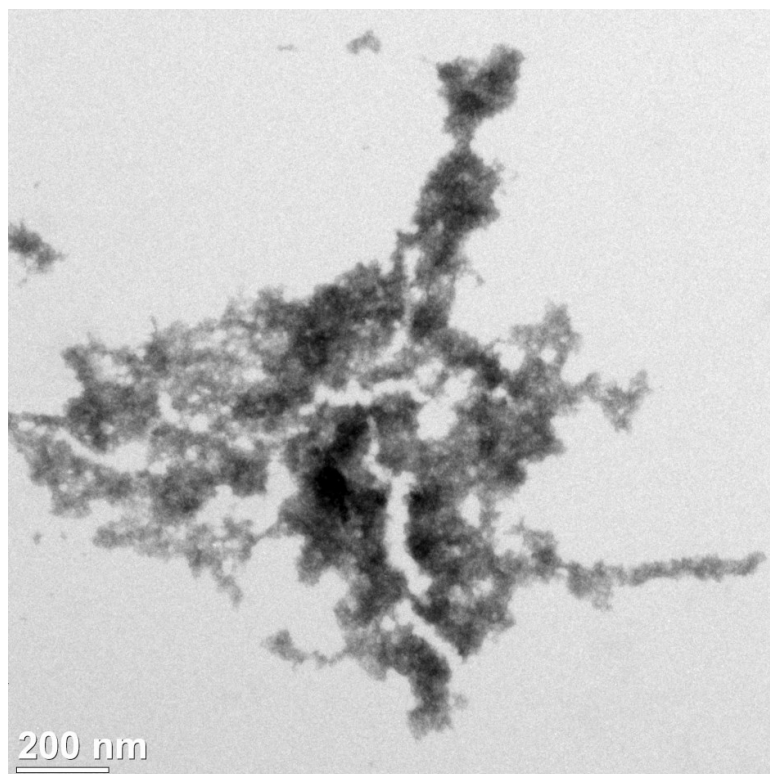


**Figure 11. Bright field TEM micrograph of Np(IV) precipitate**

The high resolution TEM micrograph shown in Figure 12-(A) clearly demonstrates the agglomeration of uniformly sized particles with 2-5 nm in diameter. The small particles also form agglomerates in the nanometer-size with diameters  $\sim 15$  to 20 nm (in the left-top in Figure 12-(a) and in Figure 12-(b)). The relevant EDX spectrum (Figure 12-(c)) reveals the dominant presence of Np and O in the nanoparticles. When zooming in on some specific particles, clear lattice images could be acquired (Figure 12-(b) and 12-(d)). The corresponding selected area electron diffraction (SAED) patterns are consistent with the fluorite-type  $\text{NpO}_2$  structure ( $Fm\bar{3}m$ )[79] without the presence of secondary phases (Figure 12-(e)).

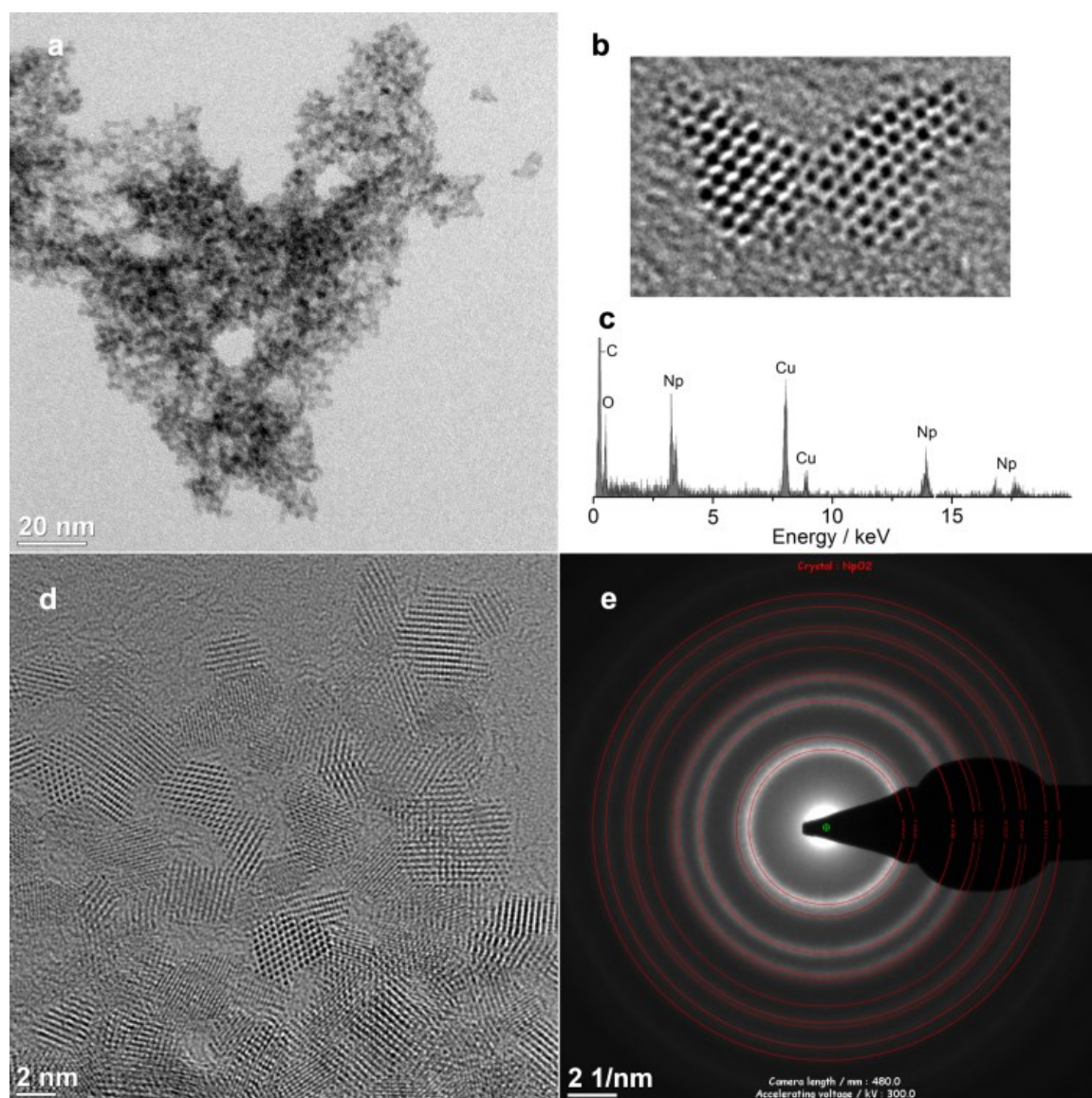


**Figure 12. TEM data of re-dispersed Np(IV) precipitate – NpO<sub>2</sub> NCs**

(A) Bright field TEM micrograph of agglomerated NpO<sub>2</sub> nanoparticles and (B) HR-TEM image of NpO<sub>2</sub> NC agglomerated as a cluster and (C) energy dispersive X-ray spectrum of NpO<sub>2</sub> NCs . Bottom: (D) HR-TEM micrograph of agglomerated NpO<sub>2</sub> NCs and (E) experimental SAED ring pattern superimposed with a modelled SAED pattern based on face-centered cubic NpO<sub>2</sub> (ICSD card 647176)

Note that the gentle drying process to prepare TEM samples at 298 K would not cause the formation of NpO<sub>2</sub> crystals, as the synthesis of crystalline NpO<sub>2</sub> generally involves calcination with high temperature.[80] Hence, it is highly likely that the observed NpO<sub>2</sub> NCs were already present in the solution phase. Other TEM micrographs and corresponding SAED in Figure 13 for the precipitate obtained directly from the solution 1 in Figure 8 (*i.e.* “non re-dispersed”



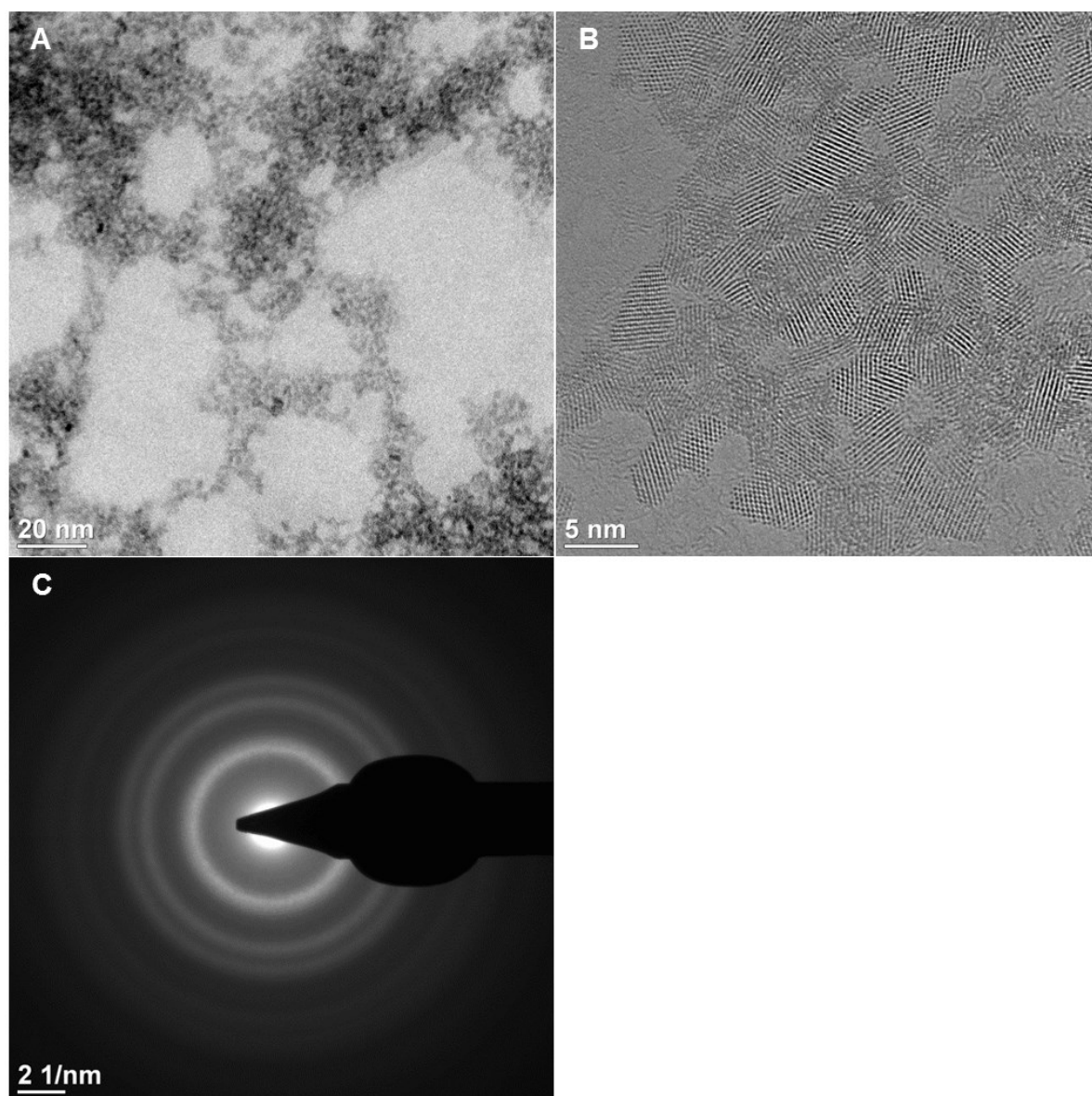


**Figure 13. TEM data of Np(IV) precipitate isolated from dispersion– NpO<sub>2</sub> NCs**

(A) Bright field TEM micrograph of agglomerated NpO<sub>2</sub> nanoparticles

(B) HR-TEM image of agglomerated NpO<sub>2</sub> NCs

(C) experimental SAED ring pattern

Note: NCs were isolated from dispersion before any sedimentation process occurred.

precipitate) still showed clear lattice fringes compatible with the NpO<sub>2</sub> structure, confirming the formation of NpO<sub>2</sub> NCs even in the original precipitate before the washing process.

These results suggest that the dissociation of the initial soluble Np(IV) complex (*i.e.* [Np(IV)(CO<sub>3</sub>)<sub>5</sub>]<sup>6-</sup>) induces the intrinsic formation of nanocrystalline NpO<sub>2</sub> in the solution phase.

### 3.3 Electronic structure of Np(IV) precipitate obtained at near-neutral pH

The electronic structure of the Np precipitate state was further investigated by XPS. The survey spectrum of the binding energies (BEs) of the Np(IV) precipitate is shown in Figure 14. The sample was deposited after washing with ultrapure water and drying at RT on a highly ordered pyrolytic graphite (HOPG) sample holder. The spectrum indicates various peaks originating from Np and oxygen electrons and the background material including O KLL and C KLL Auger peaks. The dominant C 1s peak at 285 eV (referenced for BE calibration) and the C KLL Auger electrons ( $\sim 1013$  and  $\sim 994$  eV) were originated from the matrix of the sample. The Auger peaks for oxygen were also observed around 770 eV next to the O 1s electron state around 530 eV. Np was indicated by a typical split of the Np 4*f* core level resulting in a doublet around 404 eV and 415 eV.

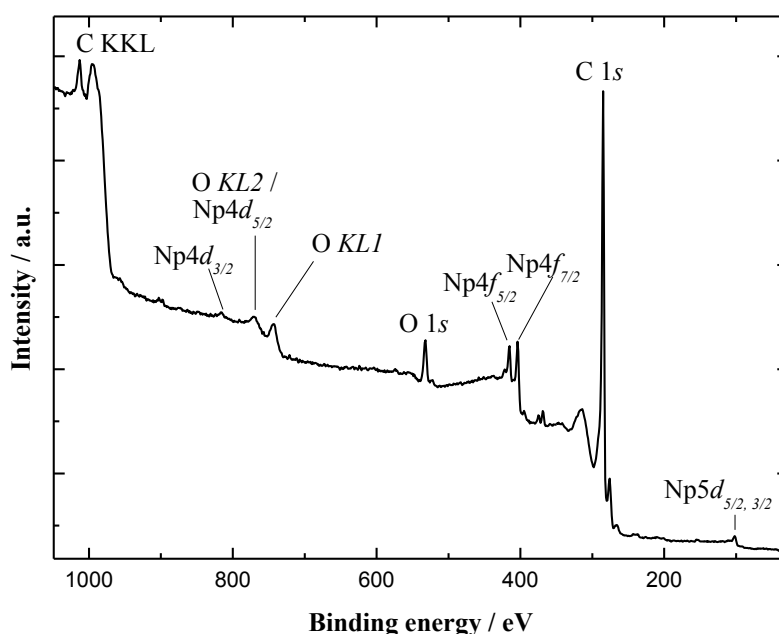
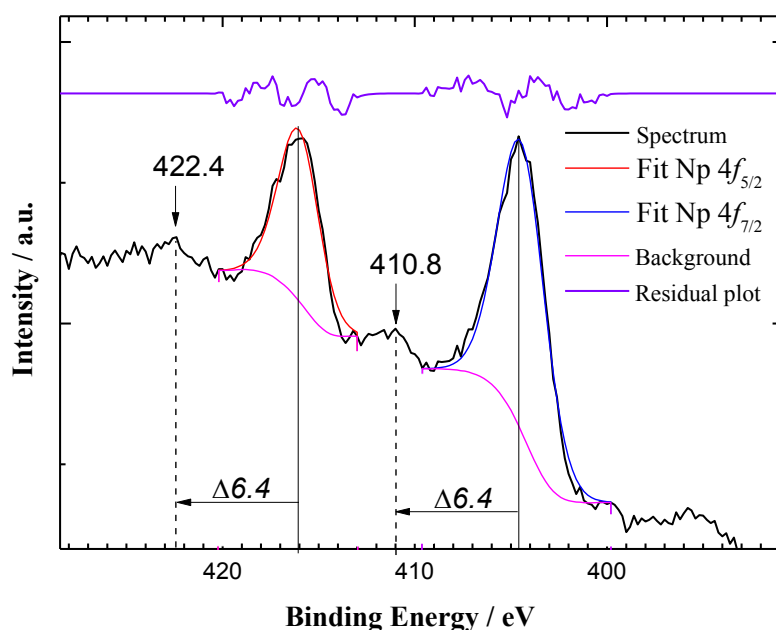


Figure 14. Survey XPS of NpO<sub>2</sub> NCs

The electron BEs of Np and oxygen core electrons were further investigated in more detail for the Np 4*f* and O 1s core levels. Corresponding XPS spectra and electron BEs of the Np 4*f* core electrons are displayed in Figure 15 and Table 4, and for the O 1s core electrons in Figure 16.

The Np 4*f* XPS (Figure 15, see also Figure 51 in Appendix) consists of the spin-orbit split doublet (Np 4*f*<sub>7/2</sub>/Np 4*f*<sub>5/2</sub>).



**Figure 15. Np 4f core level XPS of Np(IV) precipitate.**

The levels Np  $4f_{7/2}$  and Np  $4f_{5/2}$  were determined at  $404.4 \pm 0.2$  eV BE and  $416.0 \pm 0.2$  eV BE with a spin-orbit split of  $\Delta E_{sl}$  (Np  $4f$ ) = 11.6 eV. Satellite peaks were determined at higher BE with  $\Delta E_{sat} = 6.4$  eV than the main peaks (see also Figure 51 in Appendix). These characteristic satellites at  $\sim 7$  eV higher BE, related to the spin-orbit split doublet peaks, are exclusively observed for actinides dioxides with cubic structure,  $\text{ThO}_2$ ,  $\text{UO}_2$ ,  $\text{PuO}_2$  and  $\text{AmO}_2$ . [81-85] The  $\Delta E_{sl}$  (Np  $4f$ ) =  $\sim 11.7$  eV and the appearance of satellites with  $\Delta E_{sat} = 6.8$  can be regarded as a robust intrinsic signature of the fluorite structure [83, 84] and, hence an indication of the well-ordered  $\text{NpO}_2$ -like structure of the Np(IV) solid precipitated at near-neutral pH. Comparing the determined Np  $4f$  level with referenced BEs of various Np-oxides reveals a significant shift to higher BE (Table 5). One possible interpretation of the peak shift in BEs of Np core level are redox processes (oxidation/reduction), potentially indicating the formation of Np(V) species/ $\text{Np}_2\text{O}_5$  or a mixed valency in a mixture of  $\text{NpO}_2/\text{Np}_2\text{O}_3$  (Table 5). Nevertheless, oxidation processes in this study should be inevitably related with the quantitative disappearance of the high BE satellites [83, 86] next to a shift of O  $1s$  BE to lower energy values ( $\sim 528/9$  eV) due to the loss of the cubic structure in  $\text{Np}_2\text{O}_5$ . [83] This shift to  $\sim 529$  eV was not observed in O  $1s$  XPS spectrum (Figure 16). In conclusion, the formation of  $\text{Np}_2\text{O}_5$  can be ruled out [83] in particular when considering the corresponding XAS results (cf. section 3.1.).

**Table 4. Electron BE of core level in Np-precipitate at near-neutral pH at 1253.6 eV.**

Core level	Electron BE [eV]	FWHM [eV]	$\Delta E$ [eV]
Np 4 <i>f</i> <sub>5/2</sub>	416.0 ± 0.2	2.3	$\Delta E_{st} = 11.6$
Np 4 <i>f</i> <sub>7/2</sub>	404.4 ± 0.2	2.2	
Satellite Np 4 <i>f</i> <sub>5/2</sub>	422.4 ± 0.2	-	$\Delta E_{sat} = 6.4^*$
Satellite Np 4 <i>f</i> <sub>7/2</sub>	410.8 ± 0.2	-	$\Delta E_{sat} = 6.4^*$
O 1s	533-531	-	-

\* = related to corresponding Np 4*f* core level

The shift of the 4*f* core level to higher BEs can be induced by the work function of photoelectrons in nano-sized material: measured energies of the emitted photons in general can be shifted due to the value of the work-function in non-conductive/isolating material.[87, 88] Additionally, the work function significantly increases with decreasing size of the investigated material.[89] Therefore, the physical properties of NpO<sub>2</sub> NCs (prevailing nano-crystalline solid state that is presumably a non-conducting material) and slight charging effects of the background material (originating from mother solution or the Np-material itself) might induce this significant shift to higher BEs.

**Table 5. Electron BEs of Np 4*f*<sub>7/2</sub> core level for a series of Np-oxides with different valencies.**

Np-oxide	Np <sub>2</sub> O <sub>3</sub> <sup>[83]</sup>	NpO <sub>2</sub> <sup>[83]</sup>	NpO <sub>2</sub> /Np <sub>2</sub> O <sub>3</sub> <sup>[83]</sup>	Np <sub>2</sub> O <sub>5</sub> <sup>[86]</sup>	This study
Valency	(III)	(IV)	(IV/III)	(V)	(IV)
Electron BE of Np 4 <i>f</i> <sub>7/2</sub> [eV]	401.6	402.9 ± 0.2	403.8	403.1 ± 0.3	404.4 ± 0.2

The Np(IV) precipitate sample, which is identified as NpO<sub>2</sub>-like structure due to the presence of satellite peaks, shows a dominant O 1s peak broadening from 533.2-530.8 eV (Figure 16). Similar spectra were observed in dissolution experiments of Th(IV) oxyhydroxide and for uranium compounds interacting with mineral interfaces.[90, 91] These spectra reveal different types of oxygen bonds, namely from oxide (O<sup>2-</sup>) at 530 ± 0.5 eV, hydroxide (OH<sup>-</sup>) at 532 ± 0.5 eV, and chemically sorbed or bound H<sub>2</sub>O at 533 ± 0.5 eV. The O 1s BEs of O<sup>2-</sup>, OH<sup>-</sup>, and H<sub>2</sub>O are similar to those of Th(IV) oxyhydroxide colloids.[50] The Np(IV) precipitate was identified as precipitated agglomerate of NpO<sub>2</sub> NCs by HR-TEM (cf. section 3.2.).

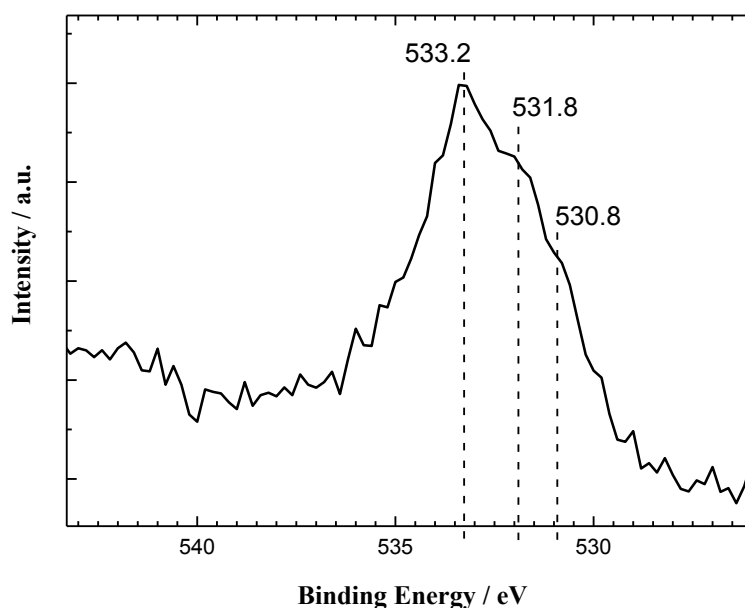


**Figure 16. XPS O 1s core level of NpO<sub>2</sub> NCs.**

Therefore, the BEs of oxide oxygen O<sup>2-</sup> core electrons at 530.8 eV correspond to the oxygen bonds in the fluorite structure of the NpO<sub>2</sub> nanoparticles. Due to the high surface of nanoparticles a significant number of oxygen atoms are located on the surface or at the water-solid interface compared to atoms incorporated in the core-matrix. Consequently, the BEs of 533.2 and 531.8 eV are attributed to chemically sorbed H<sub>2</sub>O and hydroxyl groups on the nanoparticle surface in the precipitate. The O 1s core levels of defined fcc AnO<sub>2</sub> NCs synthesized by thermal decomposition strategy showed similar broad peaks originating from various types of oxygen bonding.[92, 93] Note that the ratio of the surface water content in nanoparticles is easily influenced by sample preparation and atmosphere interactions. The Np(IV) precipitate was prepared under nitrogen atmosphere. During the installation of the sample into the XPS chamber, the thin layer of NpO<sub>2</sub> NCs could be inevitably exposed to atmosphere for several hours. Thus, the possible contamination, such as water adsorption at the NCs surface, was considered knowing that if it occurred it would ultimately change the sample composition. This possible chemical change could influence the interpretation of the XPS-results, especially the O 1s core BEs. In order to prevent exposition of the precipitate to the atmosphere, XPS investigation should be performed with an appropriate analytic chamber in Ar atmosphere and/or cooled nitrogen.[50]

### 3.4 Insights into the formation of NpO<sub>2</sub> nanocrystals

#### 3.4.1 *In situ* monitoring of the Np(IV) hydrolysis and agglomeration of NpO<sub>2</sub> nanocrystals

The hydrolysis of Np(IV) and the subsequent precipitation of NpO<sub>2</sub> NCs were monitored *in situ* by PCS in order to determine the particle size distribution in solution in dependence on time and correlate this with their resulting UV-vis absorption spectra. The particle size distributions in the supernatant of hydrolyzed Np(IV) in dependence on time are displayed in Figure 17. The particle morphology in the course of aging in solution is shown in Figure 18.

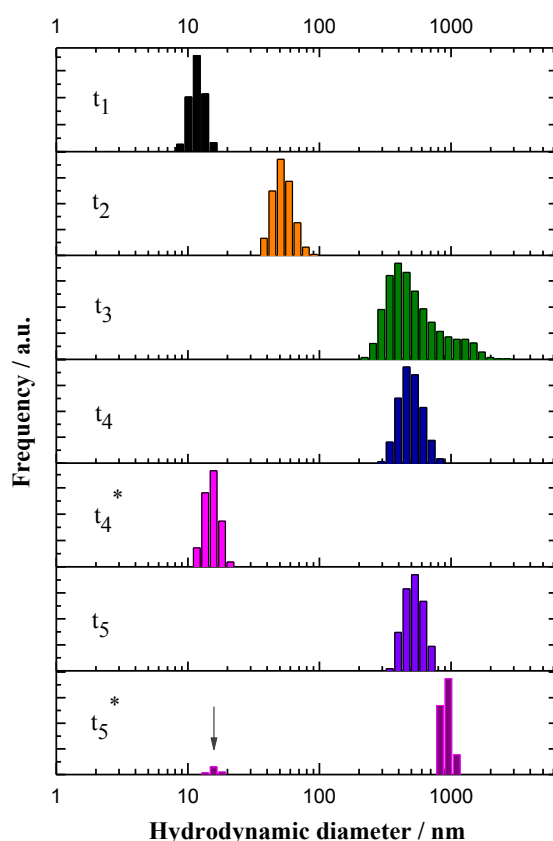


**Figure 17. PSD of NpO<sub>2</sub> NCs agglomerates in dependence on time**

Frequency of PSD determined from untreated supernatant.  $t_1 = 1/60$  h,  $t_2 = 2$  h,  $t_3 = 3$  h,  $t_4 = 24$  h,  $t_5 = 144$  h;  $t_4^*$  and  $t_5^*$ : corresponding PSD in homogenous samples determined in supernatant after re-dispersion of sedimented agglomerates.

Immediately after dilution, the formation of small nanoparticles was measured with an average diameter of 12 nm was determined ( $t_1$  in Figure 17). The measured PSD in the range of 10-15 nm indicates that the single NpO<sub>2</sub> nanocrystals, which range up to 5 nm per crystal unit in size were not appear in a mono-dispersed state in solution. This observation indicates the intrinsic tendency of NpO<sub>2</sub> NCs to agglomerate. The average particle size of this agglomerates of ~12 nm (PSD: 10-

20 nm) was in agreement with the findings by HR-TEM results (Figure 12-(A) and 12-(B)). Here small agglomerates with diameters of sizes around 10-15 nm were observed. These were composed of two to a maximum of four/five NCs. It should be considered that TEM images are not necessarily representative of the whole particles present in the waterborne state, as deposition and drying process can change chemical environment around the particles that may cause aggregation.

After an equilibration time of two hours small agglomerates were not determined but particle fractions with bigger hydrodynamic diameter of  $\sim 55$  nm were detected. This indicates the growth of particles or an enhanced agglomeration of the smaller sized 'sub'-agglomerates (characterized by diameter  $< 20$  nm as observed by HR-TEM). HR-TEM revealed that the  $\text{NpO}_2$  NCs were not grown in their actual crystal size ( $\sim 5$  nm), which led to the assumption that only the agglomerates in solution grew in size (Figure 18-(B)). Additionally, the UV-vis absorption spectrum of the bigger agglomerates in solution showed an increase in the absorbance at 742 nm (Figure 19-(a), insets Figure 19 and Table 6) as well as the baseline (especially at 500 nm). The increase in baseline can be attributed to the light scattering of small particles [66], or in the present case, it could be a result of the growing agglomerates with bigger diameter. After three hours, the PSD of the agglomerates split at around  $\sim 200$ -500 and  $\sim 1000$  nm (Figure 17-(t<sub>3</sub>)). Additionally, the precipitate formation becomes visible (Figure 52 in appendix) with the disappearance of the characteristic absorbance at 742 nm and a significant decrease in baseline (Figure 19-(a) and Table 6). As a consequence of the settlement of bigger sized agglomerates with diameter  $> 1$   $\mu\text{m}$  (Figure 17), the scattered light intensity was no longer detected. After 24 h the Np(IV) seemed to be quantitatively precipitated, although a contribution from the weak scattering light of the remaining particles or agglomerates in solution with an average diameter of  $\sim 500$  nm was still observed (Figure 17-(t<sub>4</sub>)). Based on their diluted concentration in solution the remaining agglomerates (t<sub>4</sub>) after 24 h were not indicated by the colloidal Np(IV) absorbance at  $\lambda_{742 \text{ nm}}$ , but they showed a weak contribution in baseline absorbance (especially at  $\lambda_{500 \text{ nm}}$  (Figure 19-(a)) caused by their scattered light contribution, which is much more pronounced than the absorbance of Np(IV) at 742 nm which could depend linearly on Np(IV) absorbance/concentration following the Lambert-Beer-Law. The occurrence of the absorbance around 742 nm is speculative: it could result from absorption of Np(IV) atoms in the particles or from surface plasmon resonance due to the electronic structure of the particles dependent on their size and shape. It is possible that the majority of the  $\text{NpO}_2$  NCs settled to the ground due to their incorporation into big micron-sized agglomerates as indicated by TEM (Figure 11). Redispersed of the settled agglomerates resulted in the distribution of small agglomerates (Figure 17-(t<sub>4</sub><sup>\*</sup>)) with a PSD of  $< 20$  nm (average diameter  $\sim 15$  nm) together with the simultaneous appearance of UV-vis absorbance at 742 nm and an increasing baseline (Figure 19-(b)).

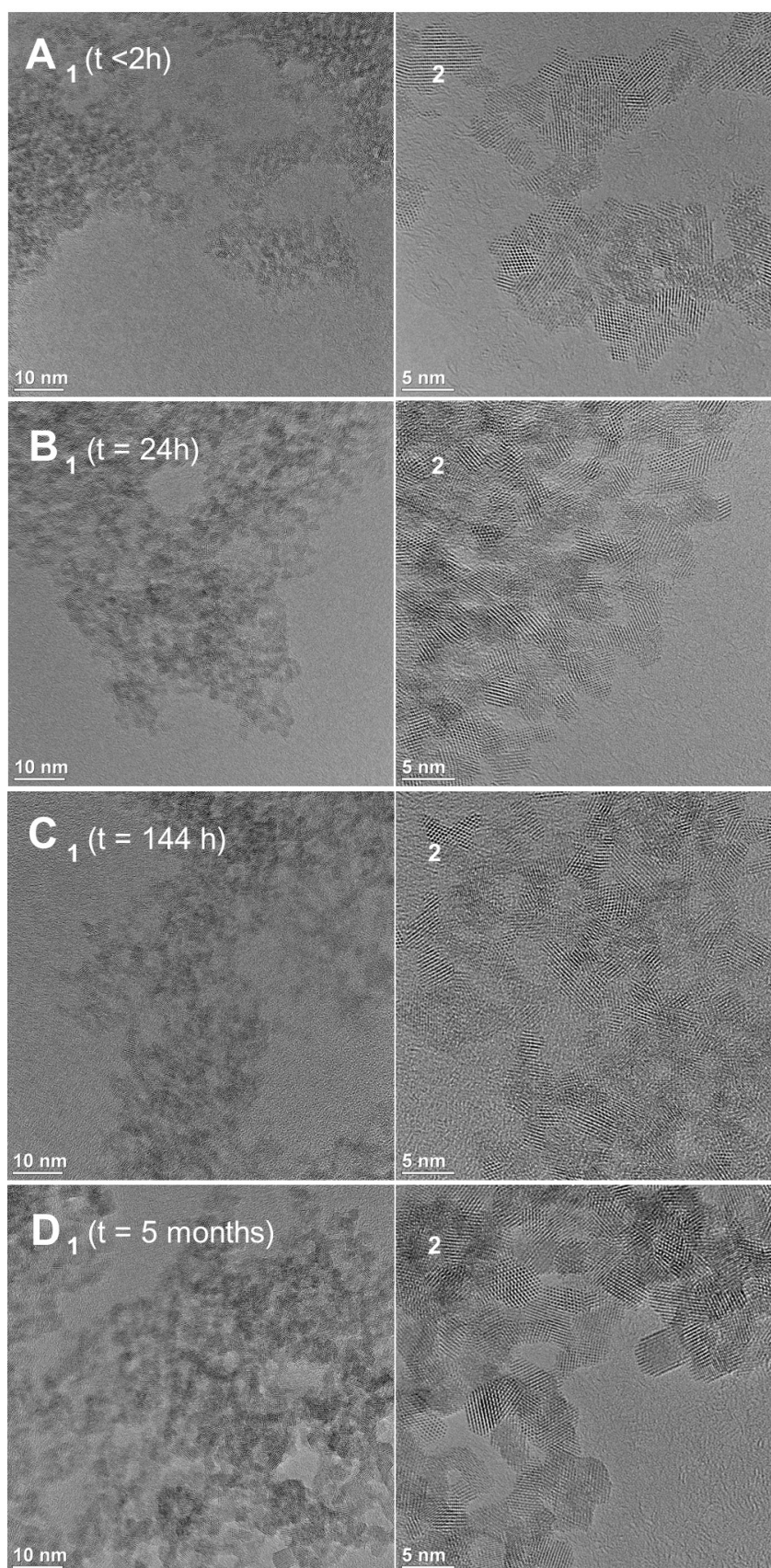


**Figure 18.** HR-TEM micrographs of  $\text{NpO}_2$  NCs in dependence on aging time. Equilibration time (A)  $<2$  h ( $t_1$ - $t_2$ ), (B) 24 h ( $t_4$ ), (C) 144h ( $t_5$ ) and (D) 5 months in magnification 300 kx (1) and 620 kx (2)



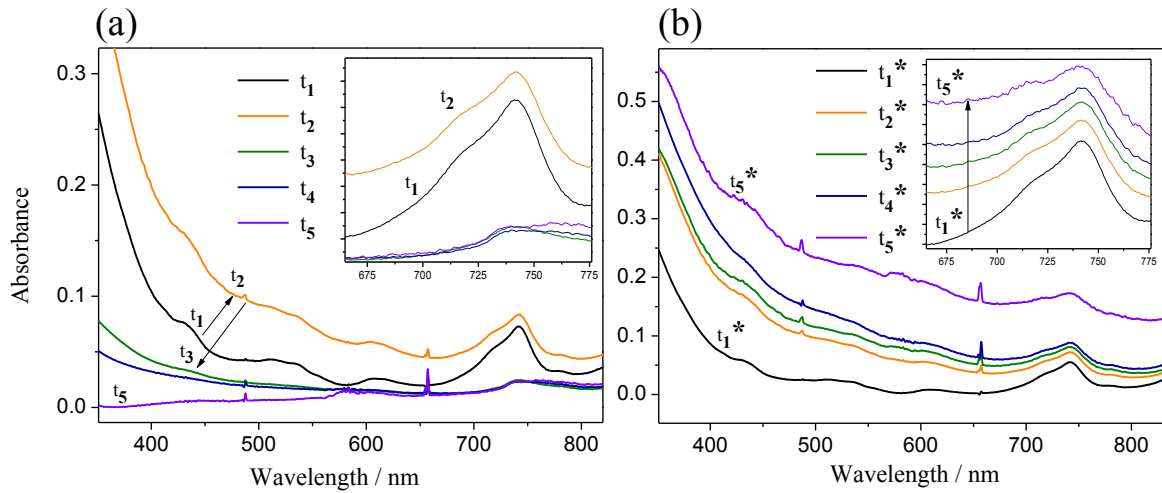


**Figure 19. UV-visible absorption spectra of hydrolyzed Np(IV) and NpO<sub>2</sub> NCs in solution in dependence on time**

(a) Supernatant of untreated samples:  $t_1 = 1/60$  h,  $t_2 = 2$  h,  $t_3 = 3$  h,  $t_4 = 24$  h,  $t_5 = 144$  h and  
 (b)  $t_{(1-5)^*}$ : samples obtained by re-dispersion of sedimented agglomerates.

Aging the precipitate for a week led to the formation of a settled precipitate with a loss of the UV-vis absorbance, although with a scattered light intensity resulting from a small amount of agglomerates of NpO<sub>2</sub> NCs in solution with a PSD of  $\sim 500$  nm ( $t_5$ ). Redispersion of the precipitate obtained after one week ( $t_5^*$ ) resulted in larger sized agglomerates of  $1 \mu\text{m}$  in solution and not the smaller agglomerates of  $\sim 15$  nm observed after 24, therefore indicating an enhanced agglomeration/crosslinking process of NpO<sub>2</sub> NC cores.

Additionally, the time-dependent UV-vis measurements revealed a continuous increase in background (Figure 19-(b) and Inset; Table 6-(b)) due to increased scattering light intensity, which could indicate the formation of NCs agglomerates with a larger size. As confirmed by PCS results in Figure 17, the agglomerates tend to grow bigger with time.

To resolve the actual absorbance of Np(IV) in the particles/agglomerates from the scattering contribution in the UV-vis spectra (e.g., increasing baseline), a baseline correction was required. A raw approximation was accomplished by calculating  $\Delta I$ , representing the difference of the absorbance values at  $\lambda = 742$  nm to those at 645 nm which represent the absorption of Np(IV) and contributions of the scattered light from agglomerated particles, respectively (Table 6). Note that further research is essential to proof the characteristics of absorbance and the scattering contributions that in summation contribute to the total observed UV-vis spectrum of NpO<sub>2</sub> NCs in solution. Nevertheless, with this raw approximation, a decrease in the ratio was determined by each aging step, possibly indicating the decrease in the Np(IV) absorbance in the particles/agglomerates, and a degradation of the signal-noise ratio with time.

Table 6. Coherences in PSD, UV-vis absorbance of Np(IV) solutions and sediment occurrence

		(a) Supernatant of untreated samples ( $t_x$ )			(b) Supernatant of homogenized dispersion ( $t_x^*$ )				
		UV-vis characteristics		Particles size distribution	UV-vis characteristics		Particles size distribution		
Reaction coordinate	Time [h]	Absorbance at $\lambda_{742}$ nm [a.u.]	Absorbance at $\lambda_{500}$ nm [a.u.]	$\Delta(\lambda_{742}$ nm - $\lambda_{645}$ nm) [a.u.]	Diameter/Frequency (sediment appearance)	Absorbance at $\lambda_{742}$ nm [a.u.]	Absorbance at $\lambda_{500}$ nm [a.u.]	$\Delta(\lambda_{742}$ nm - $\lambda_{645}$ nm) [a.u.]	Diameter/Frequency
$t_1$	1/60	0.0729	0.0420	0.0229	~15 nm/100% (no sediment)	0.0554	0.0240	0.0054	n.m.
	2	0.0836 (+)	0.0924 (+)	0.0453 (+)	~55 nm/100% (no sediment)	0.0726 (+)	0.0964 (+)	0.0362 (+)	n.m.
$t_3$	3	0.0247 (-)	0.0217 (-)	0.0132 (-)	~500 nm/80% ~1 $\mu$ m/20% (notable sediment)	0.0819 (+)	0.1160 (+)	0.0489 (+)	n.m.
	24	0.0227 (-)	0.0183 (-)	0.0122 (-)	~450 nm/100% (extensive sediment)	0.0889 (+)	0.1452 (+)	0.0600 (+)	~15 nm (100%)
$t_5$	144	0.0227	0.0067 (-)	0.0112 (-)	~500 nm/100% (extensive sediment)	0.1734 (+)	0.2338 (+)	0.1543 (+)	~15 nm (5%) ~1 $\mu$ m (95%)

(+)/(-) tags: tendency of value compared to previous reaction coordinate: (+) intensification or (-) decrease in value; n.m. = not monitored

These observations are in accordance with changes in UV-vis absorption spectra of aged Pu(IV) colloids.[43] Their origin is still unknown and speculative. Nevertheless, this might be related to the change of the  $\text{NpO}_2$  agglomerate size. Therefore, one possible explanation might be the transformation of Np hydroxide species of the surface into  $\text{NpO}_2$  cores due to enhanced agglomeration.

Figure 20 displays the SAED pattern of Np(IV) precipitate in dependence on aging time. Precipitate (A) was isolated directly from the dispersion of a freshly diluted sample before any obvious sedimentation process occurred, and characterized by the diffraction patterns consistent with  $\text{NpO}_2$ . The precipitates after aging for 3 h to 24 h gave SAED patterns with more distinct diffraction rings (B) than the initial precipitate (A) indicating the presence of higher ordered structures in the solid state than in the previous precipitate state. This could be explained by the removal of amorphous phases like hydroxide and coexisting oligomeric species by washing with ultrapure water.

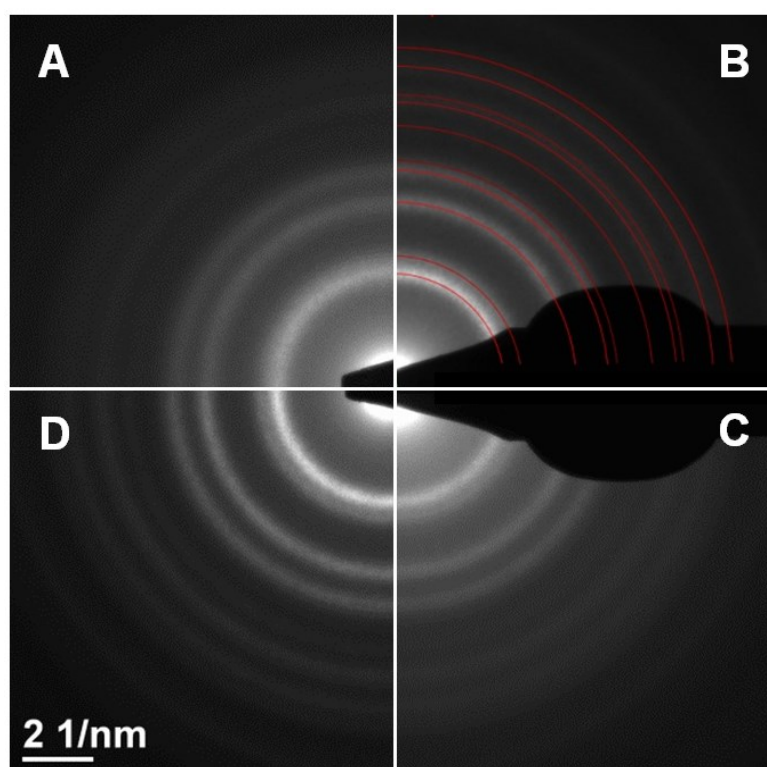


**Figure 20. SAED patterns of Np(IV) precipitates in dependence on aging time**

- (A) ( $t_1$ - $t_2$ ): hydrolyzed Np(IV) nanoparticles after < 2 h; isolated directly from colloidal dispersion  
(B) ( $t_3$ ):  $\text{NpO}_2$  NCs isolated after 3 h, superimposed with a modelled SAED pattern based on face-centered cubic  $\text{NpO}_2$  (ICSD card 647176); precipitate washed in  $\text{H}_2\text{O}$   
(C) ( $t_5$ ):  $\text{NpO}_2$  NCs after 144 h aging; isolated from re-dispersed suspension  
(D) ( $t_6$ ):  $\text{NpO}_2$  NCs isolated after 5 months aging; precipitate purged in  $\text{H}_2\text{O}$

Aged precipitate obtained from the initial diluted sample after 144 h (C) shows less distinct diffraction patterns than the purged sample. The precipitate after 5 months aging (D) was characterized by more pronounced diffraction patterns corresponding to the  $\text{NpO}_2$  cubic structure after washing.

The diffraction pattern of the NCs rapidly formed in the initial diluted sample is presumably masked by the contributions of amorphous phases and oligomeric species.

Monitoring the precipitation behavior of Np(IV) revealed a dynamic Np(IV) hydrolysis process and the subsequent intrinsic formation of  $\text{NpO}_2$  NCs. The NCs are rapidly formed and stabilized at a specific size of around  $\sim 5$  nm. Additional treatments, such as redispersion of precipitate into water, did not influence the specific size of the nanocrystals, but did affect the size of their subsequent agglomerates. Changes in UV-vis spectra, such as the increase in baseline due to increased scattering light intensity originating from the growth of agglomerates, the decrease of the Np(IV) absorbance at 742 nm and the degradation of the signal-noise ratio could be some hints to understanding the equilibration state of agglomerated  $\text{NpO}_2$  NCs.

### 3.4.2 Oligomeric Np(IV) species in the sub-nanometer scale as intermediate structures of NpO<sub>2</sub> cluster formation

In the previous chapters the results obtained by EXAFS or electron diffraction investigations indicated the possible presence of oligomeric Np(IV) species. The synthesis of highly ordered NCs by diluting aqueous monomeric Np(IV) precursors require a certain reaction mechanism including hydrolysis (illustrated in Figure 21) and the consideration of intermediate species which might be formed via nucleation. This simplified reaction scheme suggests that such intermediately formed Np(IV) species could be isolated in dependence on the reaction progress.

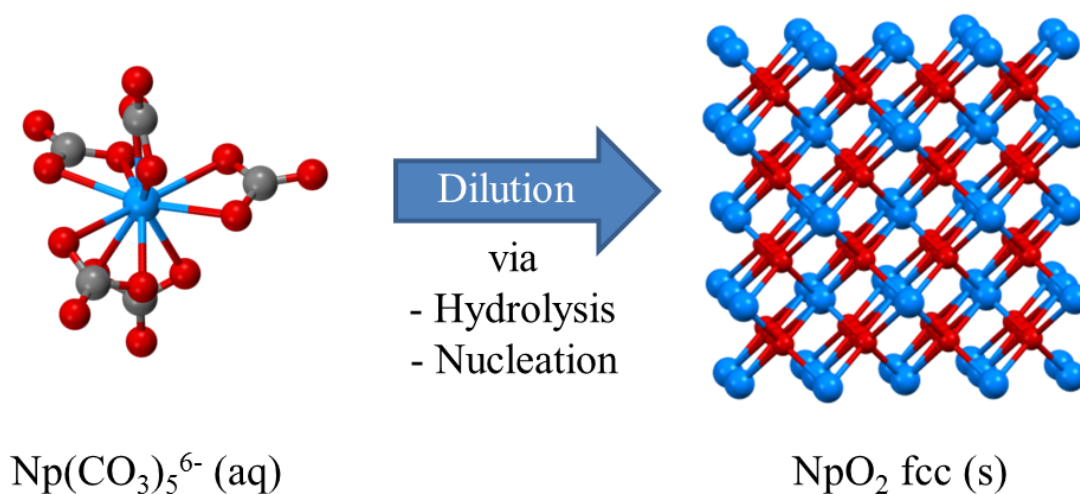


**Figure 21. Intrinsic formation of the nanocrystalline NpO<sub>2</sub> starting from aqueous monomeric precursor species via hydrolysis**

In order to isolate such intermediate species a sample of freshly hydrolyzed Np(IV) dispersion was segregated before any precipitation occurred and was investigated by HR-TEM. The TEM micrograph of the isolated fraction is shown in Figure 22, which reveals the presence of already formed NpO<sub>2</sub> NCs with ~3 nm in diameter.

Additionally, several randomly structured oligomeric Np(IV) species sized between 1-2 nm and in the sub-nanometer range were observed. These small species in the sub-nanometer scale could be phenomenologically characterized as dimeric or trimeric Np(IV) species (highlighted by white arrows; by approximation of their size and appearance by HR-TEM contrast) without knowing details of their molecular structure. The micrograph in Figure 22 could show the self-assembling of different sub-nanometer-sized Np(IV) species via randomly structured oligomeric clusters to highly coordinated NpO<sub>2</sub> nanocrystals in the fcc-lattice.

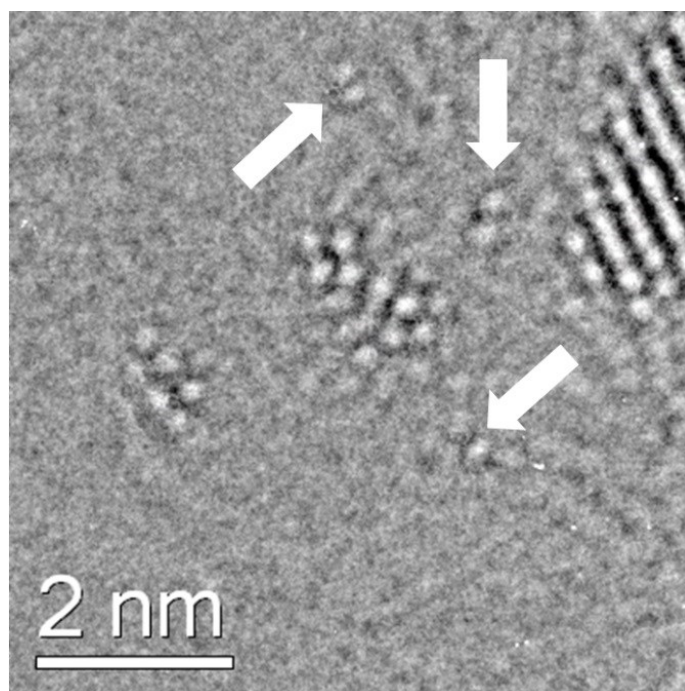


**Figure 22. HR-TEM micrograph of NpO<sub>2</sub> NC and sub-nanometer-sized Np(IV)-species**

Such small oligomeric Np(IV) species have rarely been identified in aqueous solution. First hints for the existence and contribution of small Np(IV) clusters were found by applying UV-vis absorption spectroscopy and EXAFS.[41, 77]

In addition to stabilizing complexing agents hexanuclear Np(IV) cluster structures forming octahedron molecules could be isolated and identified by EXAFS.[41] The first approximation of a Np(IV) cluster structure was fitted as an arrangement of hexanuclear complexes.[41] Herein, Takao and co-workers determined Np(IV) clusters in the polyhedron configuration with six Np atoms connected by two different O-bridges. The reported splitting into short and long distanced O-bonding and increased Np-Np backscattering are in coincidence to EXAFS findings in recent work (cf. section 3.1).[41, 77] Therefore, the consideration of nano- and subnanometer sized clusters is mandatory. Molecular structures of e.g. dimeric and trimeric Np(IV) species as indicated by HR-TEM have not been identified in literature yet.

Under certain conditions small sub-nanometer sized oligomeric species were reported for other An(IV) analogues. Ekberg *et al.* estimated by EXAFS that plutonium oxide clusters in solution consisted of 4-5 atoms in a single species.[78] In case of Th(IV), oligomeric and especially dinuclear species could be synthesized and identified both in the solid state. These dinuclear species were either bridged via hydroxyl- [94-96] or oxo-groups[97, 98]. Structural investigations on aqueous systems revealed that dimeric dihydroxo-bridged Th chlorides were present in solution.[96] Hexanuclear complexes of Th(IV) and U(IV) were observed both in the solid state

and in solution in the presence of carboxylic ligands.[99] Hexanuclear compounds remain stable even in solution due to the bridging carboxylic groups stabilizing the hexanuclear structure. The presence of carboxylic ligands prevents the formation of larger polynuclear species at least up to pH = 3.2. Recently, a hexanuclear Pu(IV) cluster structure with  $[\text{Pu}_6(\text{OH})_4\text{O}_4]^{12+}$  core was identified after defined hydrolysis and condensation reactions.[100]

Avoiding the stabilizing effect of functionalized bridging compounds, the polynuclear species  $[\text{Th}_6(\text{OH})_6\text{O}_6]^{16+}$  was indicated in solution as a precursor of  $\text{ThO}_2$  crystallites by studying a clear thorium sol under ambient conditions and a heat-treated thorium sol, an opaque solution, by low- and high-angle X-ray scattering. The opaque solution contained  $\text{ThO}_2$  crystallites of ~4 nm size, that joined with other crystallites formed after heating, whereas the clear solution contained the polynuclear species  $[\text{Th}_6(\text{OH})_6\text{O}_6]^{16+}$  which was not a fragment of the fluorite structure.[101, 102] In an ambient environment under near-neutral pH such structures of polynuclear species are still unknown, especially in case of Np(IV) and are reported for the first time in this work (Figure 22).

The rapid organization of nanocrystals with the fcc-based oxide structure and the absence of hydroxyl groups in their crystalline core indicates that the reaction mechanism is mainly dominated by the oxolation reaction as also predicted for Pu(IV). In long-term aging experiments of Pu(IV) hydroxide precipitates, the conversion of amorphous particles into  $\text{PuO}_2$  with crystalline cubic cores (2 nm in diameter) was also observed.[103]

A plausible mechanism of  $\text{PuO}_2$  colloid formation involves the condensation of poorly crystalline or amorphous Pu(IV) hydroxides and oxyhydroxides, which further evolves into the fcc-based  $\text{PuO}_2$ . [42, 104] The results from UV-vis, EXAFS and laser induced breakdown detection (LIBD) experiments herein give hints for a reasonable formation mechanism: two monomeric  $\text{Pu}(\text{OH})_2(\text{H}_2\text{O})_2^{2+}$  units *via* hydrolysis and condensation define an edge sharing, charge-neutral binuclear species (illustrated in Figure 10. in [104]). This binuclear species reacts further stepwise *via* trinuclear species with monomeric  $\text{Pu}(\text{OH})_2(\text{H}_2\text{O})_2^{2+}$  units resulting in polynuclear species. Subsequent growth presumably leads to  $\text{PuO}_2(\text{cr})$  colloids.[105] The consideration of bi- and trinuclear species crosslinking each other *via* oxolation to crystalline  $\text{AnO}_2$ -structures could fit to the phenomenological observations in the present Np(IV)-system.

The intrinsic and rapid formation of  $\text{NpO}_2$  NCs observed by HR-TEM in the present study suggest there exists similarities with An(IV) chemistry in terms of hydrolysis. Ikeda-Ohno and co-workers also confirmed the evolution of  $\text{CeO}_2$  NCs through simple hydrolysis of aqueous Ce(IV) species, a chemical analogue of An(IV)[106]. The initial precursor Ce(IV) species were identified as primarily various oxo-bridging dinuclear complexes (next to a trinuclear complex), not mononuclear ones.[106, 107] Even to date there are no other studies reporting the structure of similar oligomeric Np(IV) species in solution.[39]



### 3.4 Implication of the intrinsic formation of NpO<sub>2</sub> NCs under ambient conditions

Soluble An(IV) species formed in alkaline conditions, such as  $[\text{Np(IV)(CO}_3)_5]^{6-}$  in the present case, have been considered stable. However, the present results demonstrate, that the hydrolysis of An(IV) is strong enough to dissociate these stable species by simple dilution and the subsequent marginal change in pH, ultimately yielding crystalline AnO<sub>2</sub> nanoparticles. The present results also simulate the plausible transport scenario of An(IV) from waste repositories (near field with alkaline conditions) to the surrounding environment (far field with neutral conditions) involving diffusion processes (dilution). The observed drastic change in chemical form from soluble species to stable nanocrystalline oxides would have a significant impact on understanding the behaviour of An in natural aquatic environments. This is of particular importance in terms of long-term prediction of radionuclide transport in geological environments, as AnO<sub>2</sub> NCs are expected to be stable for a long periods of time and the co-existing amorphous phases could even transform into AnO<sub>2</sub> NCs over time.[108]

This study also highlights the importance of further investigation into the formation of An(IV) NCs under alkaline conditions as well as their properties as colloidal particles, both of which are still unexplored. With a general knowledge of chemistry, one would expect the same hydrolysis product regardless of whether the initial solution is neutralized from acidic or from basic. The precedent works on An(IV) hydrolysis have focused primarily on the former neutralization route from the acidic condition, which would reflect the fact that the leakage of An contaminants (e.g. Pu) at shallow ground waste disposal sites was often found under acidic – circumneutral conditions (e.g. pH > 1.9 at the Maxey Flats disposal site, Kentucky, USA;[109] pH = 3.9-6.8 at the Savannah River Site, South Carolina, USA;[110] and pH = 5 at the Little Forest Legacy Site, New South Wales, Australia[111]). However, as demonstrated by EXAFS, the present alkaline-originated Np(IV) precipitate is obviously different from that of the precipitate obtained from an acidic solution.[112] That implies that the alkaline-originated precipitate would be more amorphous than the acid-originated one, or that the contribution of oligomeric Np(IV) would be different. Although further study is required to fully characterize these Np(IV) precipitates, this difference in chemical form would finally cause a significant impact on their chemical behaviour in actual environmental and engineered systems.

The NpO<sub>2</sub> NCs stabilized in specific size between 2-5 nm could also form agglomerates of different sizes. For instance, the agglomeration of 3-5 NCs could form the smaller particles with a diameter of up to ~15 nm, while the majority of NpO<sub>2</sub> NCs precipitated as micron-sized agglomerates. The formation of agglomerates in micron-size might be interpreted as immobilisation of NpO<sub>2</sub> NCs. In general, particles or agglomerates of heavy metal oxides in this



size range are immobilised by retention caused by adsorption effects or cut-off and filtration effects in the host rock material.[47] Therefore, the formation of bigger size agglomerates might retard the migration behaviour of Np(IV) under certain ambient conditions. However, there is a lack of knowledge of behaviour of AnO<sub>2</sub> NCs agglomerates under more complex but realistic environmental conditions, such as temporal variations by time in groundwater compositions, temperature, redox potential etc.. It is also unknown if the AnO<sub>2</sub> NCs would remain as immobilized agglomerates in micron-size. Aging experiments over several months did not show significant change either in the degree of crystallinity or in the averaged particle size of the NCs. These NpO<sub>2</sub> NCs could persist for a long period of time due to their thermodynamically stable and privileged fcc structure. They could be released from the waste disposal sites through mechanical, chemical or thermodynamical changes, which could occur, in the worst case, in the actual environment and show enhanced migration.

The occurrence and impact of oligomeric Np(IV) species is still unknown and should be considered in future investigations.

In addition to the environmental implication discussed above, the current work also demonstrates a new synthetic concept for producing metal dioxide (MO<sub>2</sub>) NCs *via* simple dilution of alkaline M(IV) solutions. The existing routes to MO<sub>2</sub> NCs, such as TiO<sub>2</sub>[113], ZrO<sub>2</sub>[114] or CeO<sub>2</sub>[106] are generally based on the hydrolysis of aquo M(IV) species. However, the alkaline-originated synthesis demonstrated in this study is potentially applicable to the production of MO<sub>2</sub> NCs for these transition metals.[115]

Nanoparticles of An(IV) with poorly and highly crystalline structures have been synthesized in the expectation to be significantly defined by the application of favoured synthesis strategies to obtain a desired degree of crystallinity[92, 103, 116-118], all these syntheses required additional processes e.g. heating, sintering or calcination, organic solvents, sol-gel processing and gamma-radiation. Heat-influx seems to be essential to intensifying the degree of the crystallinity.[21, 119] First syntheses of defined UO<sub>2</sub> and NpO<sub>2</sub> NCs were achieved by non-aqueous thermal decomposition.[92, 93, 116] Hereby the accessibility was limited due to actinide precursor ions of higher valency (An(V) and An(VI)) and application in an exclusively organic solvent with heat-influx. In aqueous solution, first nanopowders of UO<sub>2+x</sub> were generated by electrochemical reduction of U(VI) species.[120] Preventing the competing chemistry of highly charged precursors and influx of additional synthesis procedures the current work confirms the self-assembled formation of NpO<sub>2</sub> NCs due to the simple dilution of tetravalent aqueous precursor under ambient aqueous conditions. The resulted shape of each self-organized NpO<sub>2</sub> NC unit is described as inhomogeneous and, therefore, similar to findings of Hudry and co-workers who

---

provided defined NpO<sub>2</sub> NCs by thermal decomposition strategy (irregular shaped NpO<sub>2</sub> NCs with a similar average crystal size of 2 - 4.5 nm in diameter) achieved from the initial Np(V) precursor.[116] In conclusion, the Np(IV)/NpO<sub>2</sub> system seems to possess an intrinsic nature to stabilize within a specific domain size independent of the type of solution (aqueous or non-aqueous) or additional treatment such as heat-influx.

The principles and mechanisms of the formation and growth of MO<sub>2</sub> crystals, especially of AnO<sub>2</sub>, and the enforcement or manipulation of the resulting degree of their crystallinity are not fully clarified yet and are still of particular interest. The first evidence for the intrinsic formation of crystalline AnO<sub>2</sub> structures was observed by aging of amorphous An(IV) precipitates in long-term solubility studies. The transformation from ill-defined hydrous oxide solids to well-defined oxide structures was obtained.[119, 121] In these studies, crystalline NpO<sub>2</sub> precipitates, sized within the micrometer-scale, were obtained by aging amorphous Np(IV) hydrous oxide over more than four weeks or by heating Np(V) solution over several weeks.[119, 121] The as-prepared precipitates exhibited strong X-ray diffraction peaks after several weeks that correspond to crystalline NpO<sub>2</sub>. In these studies, competitive processes associated with the presence of both Np(IV) and Np(V) complicate the interpretation of the reaction mechanisms. In order to avoid such competitive processes, (e.g. the different redox and solubility chemistry of the parallel occurring actinides of higher valence (Np(V)), the present work confirms the precipitation of NpO<sub>2</sub>(cr) from pure aqueous Np(IV) precursor. Instead of the initial formation of poorly-defined Np(IV) hydroxides via hydrolysis, the dynamic evolution of highly structured NpO<sub>2</sub> was observed. The rapid organization of oxo-bridged nanoparticles composed in fcc indicates a reaction mechanism probably affected by oxolation reaction as predicted for Pu(IV).[42, 104] Based on the chemical characteristics of Np(IV) observed in the present study, it could be concluded that the aqueous chemistry of Np(IV) at slightly alkaline pH resembles that of Pu(IV) and Ce(IV), rather than of Th(IV). Nevertheless, under acidic conditions the redox stable Th(IV)(aq) system reveal similar An(IV) precipitation behavior after intensively increasing the pH by an excess of 1M KOH (enforced hydrolysis) and a subsequent drying process. TEM identified agglomerates of ThO<sub>2</sub> characterized by fluorite structure and irregular in shape and size (0.8-15 μm) which are composed of various crystalline domains (~5 nm in size).[122]

The current finding of self-organization of NpO<sub>2</sub> in the fcc-structure under ambient conditions and stabilization in a specific nano-size range could be utilized for new energy-efficient nuclear power systems based on minor-actinide mixed oxides (MA-MOX) fuels. MA-MOX fuels are of particular interest to reduce or eliminate Np from HLW (before enclosed in repository systems) by transmutation in fast reactors. The efficiency and costs of the Np reduction partially depends

on the chemical and physical composition of MA-MOX pellets. State of the art in MA-MOX production is raw processing of NpO<sub>2</sub> precursor powders consisting of spheroids and complicated crystals with 5-10 μm in size.[123] The poor flowability of these micron-sized spheroids in the MA-MOX pellet production influences the homogeneity of the resulting pellets and subsequently their physical properties during the burn-up process in reactor.[123-125] Herein, the application of nano-sized materials, which are easily generated in thermodynamically stabilized form from aqueous solution, to the precursor material for MA-MOX production would influence not only the efficiency in pellet production but also the overall efficiency in the nuclear cycle processing of minor actinides. This could also contribute to the safer control of the physical characteristics of fuel pellets during burn-up[126] and the reduction of the Np (or minor actinide) inventory in HLW repositories, an advantage for the safety assessment of extremely long time spans of over one million years.

---

## 4 The Np(IV)-silicate system in bicarbonate solution

This section discusses the precipitation of Np(IV) in presence of silicate, an important representative of ubiquitous occurring groundwater components, in the diluted carbonate environment as expected in the far-field of a nuclear repository. Parameters like the Si/Np ratios in solution are considered and the systems are checked for evidence of potentially long-term stabilized Np(IV) silica colloid. Experiments of various Si/Np ratios - below and above the MWSA - are performed to figure out the coherences of particle sizes, morphology, and dispersion stability of resulting particles. First hints for the driving forces and reaction mechanisms of Np(IV) silica particle formation by testing competitive polymerization behavior of both, Np and silica in diluted and saturated systems, are also presented.

### 4.1 Precipitation of Np(IV) silica particles versus silicate polymerization

As shown in the previous chapters, the dilution of Np(IV) at near-neutral pH led to the self-organization of NpO<sub>2</sub> NCs or the formation of small colloidal Np(IV) silica particles when silicic acid was admixed. This precipitation behavior raises the question concerning the driving force of Np(IV) silica particle formation. On the one hand, it seems obvious that the dilution of Np(IV) by exceeding its solubility limit at near-neutral pH as a factor of the carbonate concentration can be regarded as the driving force, but on the other hand, the question remains if the polymerization of silicate also influences the Np(IV) silica particle formation. At pH 7-9 the monomeric silicic acid is unstable and polymerization is increased in dependence on ionic strength and temperature due to the catalyzing effect of hydroxyl ions.[127] Therefore, an experiment was performed to resolve the intensity of hydrolysis and/or polymerization by determining the SLI of particles formed after moderate dilution with silicate solutions of concentrations above and below the threshold of silicate polymerization in the presence of neptunium (Figure 23-(a)) and absence (b). It has to be noted that silicate starts to polymerize at concentrations above  $\sim 2.5 \cdot 10^{-3}$  M in solutions (see chapter 2).[55] Neptunium diluted in a silica-poor environment below the MWSA (red trace in Figure 23-(a)) exhibited a strongly increased SLI, indicating the formation of larger sized particles which were not colloidal stabilized and settled noticeably with the decrease of SLI over time. This is in analogy to NpO<sub>2</sub> NC agglomeration behavior but retarded in time. In contrast, the neptunium containing silica above the MWSA (blue trace in (Figure 23-(a)) permanently showed a slightly enhanced SLI and the dispersion was stabilized without noticeable sedimentation processes due to the formation of colloidal stabilized particles of smaller size (see also similar trend observed in Figure 7).

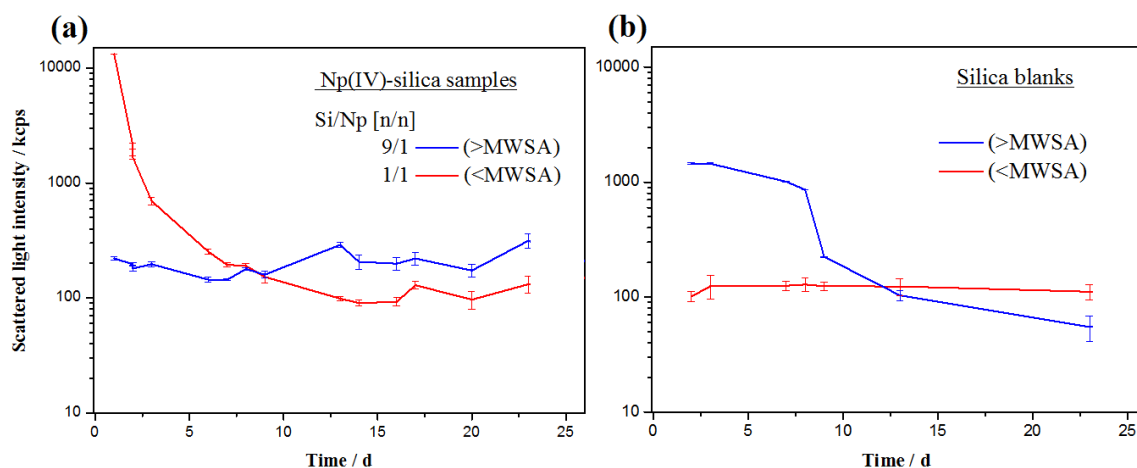


**Figure 23. Time dependence of the SLI in different silicate samples**

(a) samples containing neptunium and silicate concentrations above (blue trace) and below (red trace) the MWSA of silica.  $[Np] = 5 \cdot 10^{-4}$  M in each sample;  $[Si] = 0.5 \cdot 10^{-3}$  M (red),  $[Si] = 4.5 \cdot 10^{-3}$  M (blue); initial 0.1 M  $NaHCO_3$ .

(b) silicate blank samples in absence of neptunium above (blue trace) and below (red trace) the MWSA of silica.  $[Si] = 0.5 \cdot 10^{-3}$  M (red),  $[Si] = 4.5 \cdot 10^{-3}$  M (blue); initial 0.1 M  $NaHCO_3$ .

Again, this observation underlines the trend that a silicate enriched environment induces the formation of small and colloidal stabilized An(IV) silica particles.[49, 50] Therefore, silicate enriched solutions prevent the intrinsic formation of  $NpO_2$  NCs and their subsequent agglomeration as observed in chapter 2. These observations suggest that silicic acid might rule the Np(IV) silica particle formation. Nevertheless, in the absence of neptunium above the MWSA (blue trace in Figure 23-(b)) an increased SLI was monitored in the first seven days indicating the formation of silicate polymers. In presence of neptunium the polymerization of pure silicate polymers was not observed (confirmed by the observation of lower SLI of the blue trace in Figure 23-(a), and determination of the chemical composition in the following chapter) suggesting that the presence of neptunium prevents silica polymerization above the MWSA. This observation again highlights the strong tendency of An(IV) hydrolysis, which may govern the An(IV) silica particle formation as a factor of the molar Si/Np ratio in solution. The SLI of the silica polymers dispersion decreased to a lower value of truly dissolved silicate solutions over time, which may be caused by dissolution of the silicate polymers or by sedimentation of destabilized silicate polymers of larger size. Note that no obvious sediment formation was observable at any time. In conclusion, neptunium and silicate significantly influence each other in their hydrolysis and polymerization behavior, silicate or silicic acid prevents the intrinsic self-assembly of  $NpO_2$  NCs in the fcc-structure, whereas Np(IV) prevents the polymerization of silicic acid or silicate, in analogy to other metal ions[127, 128].

## 4.2 Influence of the initial silica concentration in solution on resulting Np(IV) silica colloid characteristics

### 4.2.1 Chemical composition of Np(IV) silica particles

The silica uptake of the Np(IV) particles is dependent on the supply of silicic acid during particle formation. Table 7 demonstrates this for samples of both the region above and the region below the MWSA. The table represents the concentration ratios of Np and Si found in solution - with initial concentrations shown in the first two columns and after two days of equilibration - before and after ultrafiltration (5 kDa). It shows that the Si/Np ratio of the colloid particles does not simply depend on the initial Si concentration of the solution or simply on the initial Si/Np ratio of the solution. The composition of Np(IV) silica particles in dependence on the reaction coordinate might be influenced by the equilibration state. Note that the molar Si/Np ratio of the colloids given in Table 7 is an average over the particle radius. Studies on Th(IV) silica colloids showed that there may be significant variation of the Si/An(IV) ratio from the surface to the center of the particles. The correlation between the silicic acid concentration in the solution and the molar Si/Np ratio of the particles is obviously determined by the structural inclusion of silica into the particle inside (see section 4.3 - internal structure by EXAFS) as well as by silica polymerization processes both in the water and on the particle/water interface. Note also that the colloids of many of the samples contain more silica than Np(IV), which makes these particles increasingly similar to silica particles with elevated silicic acid concentration.

**Table 7. Molar Si/Np ratio of the Np(IV) silica colloids in dependence on the initial Si and Np solution concentrations [Si] and [Np]**

[Si] [ $10^{-3}$ M]	[Np] [ $10^{-3}$ M]	Si/Np in solution [n/n]	Si/Np in colloids [n/n]
8.6	1.04	8.6	3.6
7.3	1.05	7.3	3.5
5.4	1.05	5.4	2.6
(>MWSA) 3.2	1.05	3.2	1.7
(<MWSA) 1.3	1.04	1.3	0.8
0.7	1.02	0.7	0.4
1.5	0.25	6	1.3

Using UV-vis absorption spectroscopy it was observed that the colloidal Np(IV) peak (which appears very reproducibly at 740 to 742 nm for Np(IV) oxyhydroxide colloids) was shifted toward 746 nm if the nanoparticles contained sufficient amounts of silica. The shift started at initial concentrations of  $>5.4 \cdot 10^{-3}$  M silicic acid in the solutions (Figure 24) and suggests a change of the electronic structure of Np in the particles in dependence on the silica environment. Here, Np(IV) silicate structures could be observed in the silica enriched environment different than in silica-poor solutions.

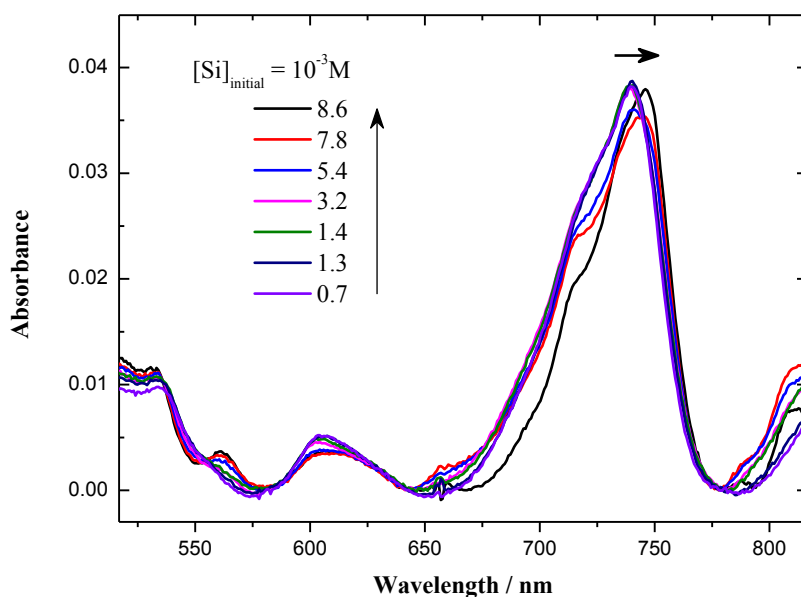


**Figure 24. Visible absorption spectra of Np(IV) in dependence on initial silica concentration**  $[\text{Np}] = 1 \cdot 10^{-3}$  M, initial silicate:  $[\text{Si}] = 0.7 \cdot 10^{-3}$  to  $8.6 \cdot 10^{-3}$  M; initial 0.1 M  $\text{NaHCO}_3$ ; pH = 8-9.

#### 4.2.2 Particle growth behavior and long-term stability

In order to figure out how the Si/Np ratios influence the resulting particles size, the time dependence of the SLI and hydrodynamic radius of colloids was determined in different system of  $[\text{Np}] = 5.0 \cdot 10^{-4}$  M and  $[\text{Np}] = 1.0 \cdot 10^{-3}$  M.

The reproducibility of simple SLI determinations can reliably serve as indication of particle growth, and the correlation between SLI and hydrodynamic diameter of particles in solution was verified for the Np(IV) silica system. In Figure 25 the correlation of the SLI with the average

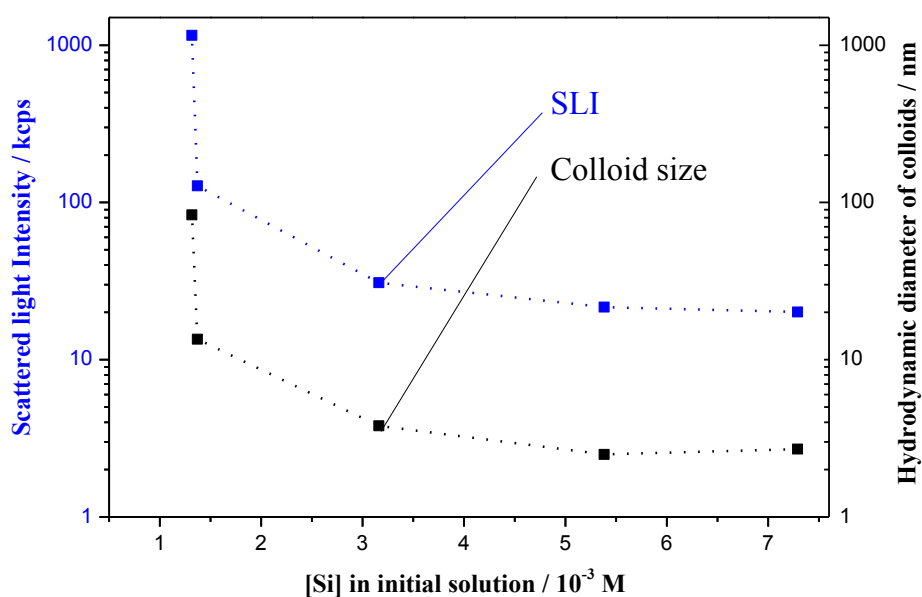


**Figure 25. Dependence of SLI and particle size (PCS) of the Np(IV) silica particles on the initial concentration of silicic acid**

[Np] =  $1.0 \cdot 10^{-3}$  M in each sample; initial [Si] given in graph; initial 0.1 M  $\text{NaHCO}_3$ ; SLI recorded after an equilibration time of <24 h.

hydrodynamic diameter of colloids in solutions with [Np] =  $10^{-3}$  M in dependence on the initial silica concentration is shown. Note, that the SLI and the corresponding hydrodynamic diameters were determined after a short equilibration time of <24 h. Silica-poor systems with a Si/Np ratio below 2 were characterized by SLI of ~150-1300 kcps and hydrodynamic diameters of ~10-95 nm, while silica-enriched systems with a Si/Np ratio above 2 showed a SLI of ~20-30 kcps by approximated hydrodynamic diameters of ~2-3 nm.

Silica-enriched systems above the MWSA exhibited lower SLI than silica-poor systems caused by the less intensive scattering contribution of small-sized colloids. Therefore, Figure 25 demonstrates that the SLI can be a quite useful semiquantitative measure of the size of the particles in the Np(IV) silica systems.

The time dependence of the SLI of colloidal systems that were generated from different silicic acid concentrations with [Np] =  $10^{-3}$  M is shown in Figure 26. Three cases can be discerned in this figure. A silicic acid concentration of  $1.3 \cdot 10^{-3}$  M is not able to stabilize the nanoparticles resulting from [Np] =  $10^{-3}$  M; fast sedimentation is observed in this case, which is in close analogy to the sedimentation behavior of  $\text{NpO}_2$  NCs, but retarded in time in comparison to rapid  $\text{NpO}_2$  NCs agglomeration in less than 24 h. A silica concentration of  $3.2 \cdot 10^{-3}$  M, also results in slow sedimentation of the particles. Stabilization was found at [Si] =  $8.6 \cdot 10^{-3}$  M.



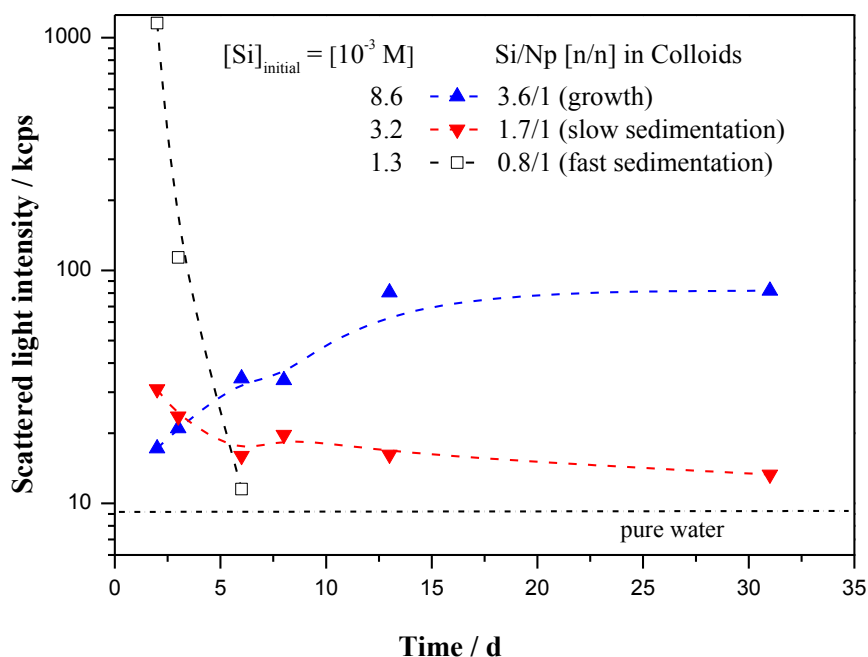


**Figure 26. Time dependence of the SLI for three systems of Np(IV) silica colloids in dependence on silica content**

([Np] =  $1 \cdot 10^{-3}$  M, initial silicate: [Si] =  $1.3 \cdot 10^{-3}$  M (white boxes) pH 8.8, [Si] =  $3.2 \cdot 10^{-3}$  M (red triangles down) pH 8.7, [Si] =  $8.6 \cdot 10^{-3}$  M (blue triangles up) pH 8.6; initial 0.1 M NaHCO<sub>3</sub>).

However, as can be seen in Figure 26, the colloids did not immediately reach their final particle size, but showed a growth phase of several days. This is another analogy between the behavior of Np(IV) silica colloids and that of other An(IV) silica colloids.[49, 50] Figure 26 shows that stabilization for at least 30 days is observed if enough silica in the [Np] =  $1.0 \cdot 10^{-3}$  M system is supplied. In another sample, also representative of the region above the MWSA, colloid stability over a period of at least 370 days was found ([Np] =  $1 \cdot 10^{-3}$  M with initial silicate: [Si] =  $9.0 \cdot 10^{-3}$  M; Si/Np = 9/1).

Above the MWSA, the excess of silicate was essential to stabilize  $1 \cdot 10^{-3}$  M Np(IV) as a new type of An(IV) colloids, the An(IV) silica colloids. Here, the stabilization of Np(IV) in the waterborne state exceeded the limits of solubility of Np(IV) species - ranging from  $10^{-8}$  to  $10^{-5}$  M - by factors of 100 to 10.000.[20, 21, 129]

In precipitation experiments at near-neutral pH, various samples with settled precipitate revealed that dissolved Np(IV) was found in the supernatant with concentrations of  $\sim 0.5 \cdot 10^{-4}$  M. Herein, the Np(IV) speciation was unknown and could not be sufficiently characterized with the applied UV-vis detection setup because of enhanced dilution of the analyte.

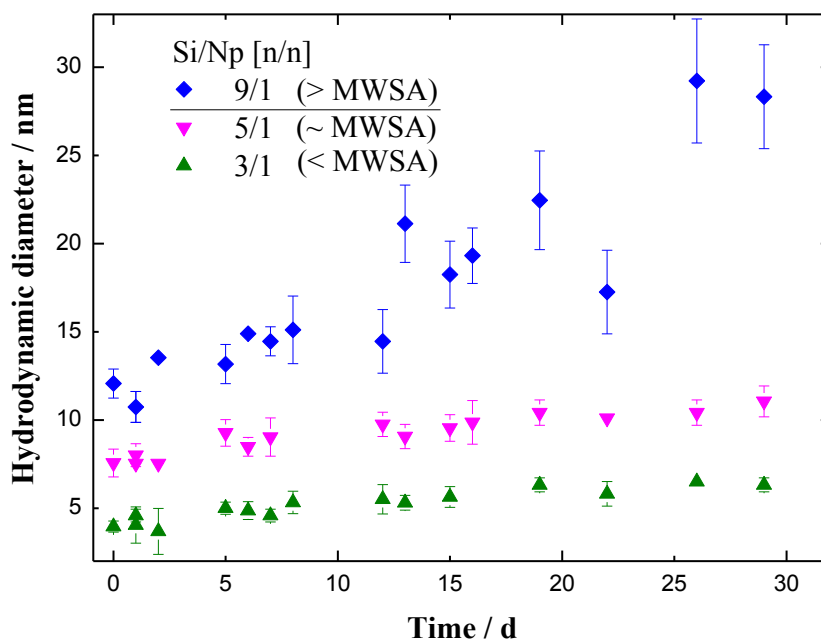


**Figure 27. Hydrodynamic diameter of Np(IV) silica colloids in dependence on time and the initial silicate concentration (PCS)**

[Np] =  $5 \cdot 10^{-4}$  M in each sample; [Si] =  $1.5 \cdot 10^{-3}$  M (green), pH 9.1, [Si] =  $2.5 \cdot 10^{-3}$  M (magenta) pH 9.0, [Si] =  $4.5 \cdot 10^{-3}$  M (blue) pH 8.9; initial 0.1 M NaHCO<sub>3</sub>. Hydrodynamic diameter determined from untreated supernatant. Error bars are given at the 95% confidence level.

The dissolved Np(IV) with concentrations  $\sim 0.5 \cdot 10^{-4}$  M could be provoked by the appearance of small oligomeric Np(IV) species.

The assumption that an increased Si/Np ratio is essential to stabilize An(IV) silica colloids at actinide concentrations of  $\sim 10^{-3}$  M [49, 50] was not proved in a diluted system of  $0.5 \cdot 10^{-3}$  M Np(IV), which is a contradiction to the non-stable system at [Np]  $1 \cdot 10^{-3}$  M. Figure 27 demonstrates the influence of the Si/Np ratio on the prevailing particles size in a  $0.5 \cdot 10^{-3}$  M Np(IV) silica system as a function of time. Again, in the sample with silica excess above the MWSA, specified as Si/Np = 9, the formation and stabilization of Np(IV) silica colloids occurred, with diameters of 10 nm in size, which grew up to  $\sim 25$ -30 nm during equilibration of 30 days. The systems below the MWSA containing less initial silica revealed the formation of smaller Np(IV) silica particles which did not significantly tend to grow in size. A Si/Np ratio of 3 and 5 resulted in the formation of particles of  $\sim 5$  nm and  $\sim 9$  nm in size. These results suggest that the formation of small Np(IV) silica colloids also depends on the Np concentration.

More detailed PSD (light-intensity weighted) of these samples in dependence on the Si/Np ratio and time are displayed in Figure 28 where an additional sample specified with Si/Np = 1/1

( $[\text{Np}] = 5 \cdot 10^{-4} \text{ M}$  and  $[\text{Si}] = 0.5 \cdot 10^{-3} \text{ M}$ ) is involved. Here, all particle fractions measured in dispersion were included, the prevailing fractions of small particles and the minor fractions of micrometer-sized particles as well. Due to the strong dependence of the SLI on the particle size, the SLI is proportional to the sixth power of the particle diameter. Generally, a minor fraction of large particles would dominate the SLI by parallel appearance of a fraction of small-sized particles in the same sample. Thus, under certain PSD conditions the scattering contribution of particles of smaller size are masked by extremely intensive scattering of large particles[62], but in the case of a dominating particle concentration of small-sized colloids beside an only minor and negligible fraction of larger particles, the smaller fraction can be reliably determined by light intensity weighted PSD as observed in Figure 28. All samples contained a fraction of larger sized particles in an early stage of equilibration, but in samples from a 3/1 ratio and so forth, this minor fraction decreased in frequency over time. Interestingly, in sample 9/1 the disappearance of the minor fraction of  $\sim 600 \text{ nm}$  sized particles was observed after 8 days of equilibration.

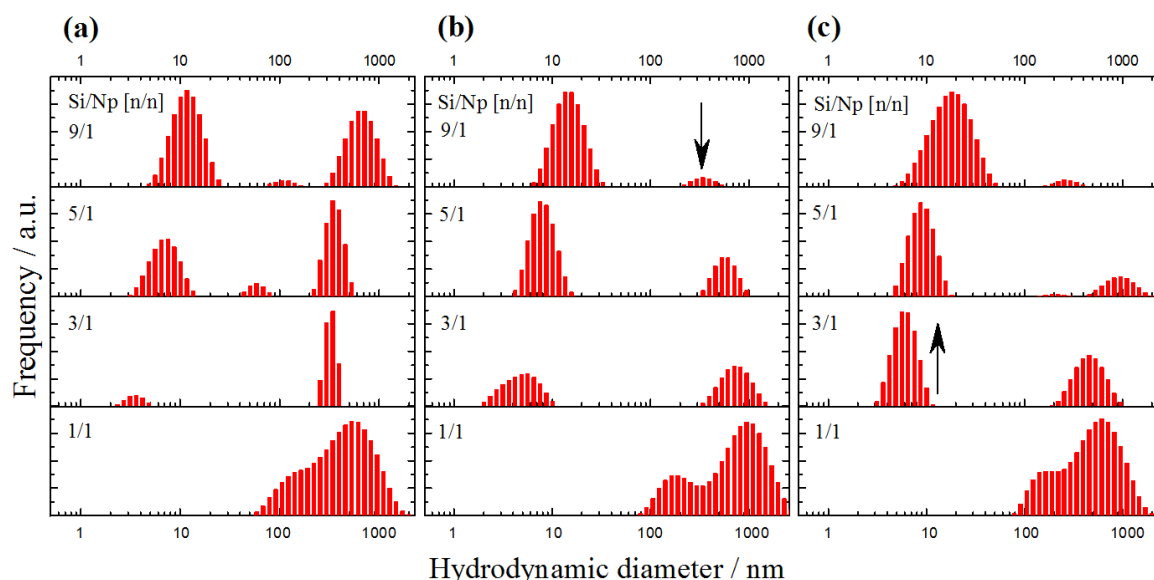


**Figure 28. Size distribution of Np(IV) silica colloids in dependence on initial silicate concentration and time**

(a) after  $<24 \text{ h}$ , (b) after  $8 \text{ d}$  and (c) after  $15 \text{ d}$ ;  $[\text{Np}] = 5 \cdot 10^{-4} \text{ M}$  in each sample; initial  $[\text{Si}]$ :  $[\text{Si}] = 0.5 \cdot 10^{-3} \text{ M}$  ( $\text{Si/Np} = 1/1$ ),  $[\text{Si}] = 1.5 \cdot 10^{-3} \text{ M}$  ( $\text{Si/Np} = 3/1$ ),  $[\text{Si}] = 2.5 \cdot 10^{-3} \text{ M}$  ( $\text{Si/Np} = 5/1$ ),  $[\text{Si}] = 4.5 \cdot 10^{-3} \text{ M}$  ( $\text{Si/Np} = 9/1$ ); initial  $0.1 \text{ M NaHCO}_3$ .

Note also that the mathematical instability during deconvolution can play a role in multimodal particle size distributions. Thus, it cannot be ruled out that the disappearance of a very small fraction of larger particles by sedimentation also influences the calculation result for the small particles (for mathematical reasons - when performing the inverse Laplace transform). For instance, one could, imagine that the disappearance of a trace of larger particles by sedimentation

causes a shift of the result for the small particles toward slightly higher values, simulating growth of the particles. Also, regard that a resolution of more than two or three size fractions in very polydisperse samples is not possible by DLS.[130] Trimodal particle size distributions should only be considered as qualitative hints for polydisperse particle systems and not used to determine the actual particle sizes within a significant confidence level.[131] They are sufficient only for raw approximation and indication of variation in particle sizes of polydisperse systems, however, spurious peaks might be caused by artefacts, ill-posed problems and inverse Laplace transforms.[62, 63, 130, 131]

However, the trimodal PSD in Figure 28-(a) of the Si/Np systems 9 and 3 are shown for comparison to emphasize the dynamic process in alteration in particle sizes over time.

In the samples of Si/Np = 3, 5 and 9 a significant increase in frequency of the smaller sized fractions between 5-30 nm was determined. In samples containing silicate at concentrations higher than that of Np by a factor of three, the Np concentration was always constant at  $5 \cdot 10^{-4}$  M in solution, while in sample Si/Np = 1/1 the Np concentration significantly decreased to  $10^{-5}$  M, resulting in the appearance of a settled precipitate. The Np remaining in the supernatant was characterized by a PSD with the main peak at ~200-1000 nm. Here, the major fraction was found at sizes of ~1  $\mu$ m which was analogous to the threshold of NpO<sub>2</sub> NC agglomeration and precipitate settlement (~1  $\mu$ m size) determined for the Np(IV)-carbonate system. Again, a destabilizing effect on Np(IV) silica colloids was observed if not a sufficient amount of silica was accessible in the Np(IV) solution.

Nevertheless, the formation and growth of Np(IV) silica particles is a dynamic process.

In long-term experiments monitoring the SLI of U(IV) silica colloids for a period of more than 850 days, fluctuations in SLI were observed and not fully understood. After the decrease of the SLI in two years, the average particle size was determined and found to be ~180 nm and the SLI was found to show no more variations. The state of this sample was interpreted as a metastable equilibration state.[49] Further long-term monitoring of the SLI and the PSD would be necessary to elucidate if Np(IV) colloids also show this behavior.

### 4.2.3 Colloidal stability of Np(IV) particles in dependence on silica incorporation into the solid phase

The influence of the silica content on the resulting surface charge of the intrinsic formed Np(IV) silica particles was investigated by the determination of the zeta potential ( $\zeta$ ) in dependence on pH and molar ratio of Si to Np in the initial solution. For this purpose, the Np concentration was kept constant ( $[\text{Np}] = 5 \cdot 10^{-4} \text{ M}$ ), whereas the concentration of silica was increased up to nine times that of neptunium ( $[\text{Si}] = 3 \cdot 9 \cdot 10^{-4} \text{ M}$ ). This was performed to simulate different conditions beneath, close to and over the threshold of silica polymerization and to utilize the stabilizing effect of silica uptake into the solid state particle structure. The zeta potentials of Np(IV) silica colloids were determined by LDV and compared to the surface charge of silica-free  $\text{NpO}_2$  NCs precipitated under similar conditions in absence of silica and of  $\text{SiO}_2$  reference material. Note that the term “particle surface charge” used in the present thesis actually describes the effective hydrodynamic surface characterized by the zeta potential. In Figure 29, the dependence of the  $\zeta$ -potential of Np(IV) silica colloids, re-suspended Np(IV) silica flocs, and  $\text{NpO}_2$  NCs on pH and the initial molar Si/Np ratio are depicted.

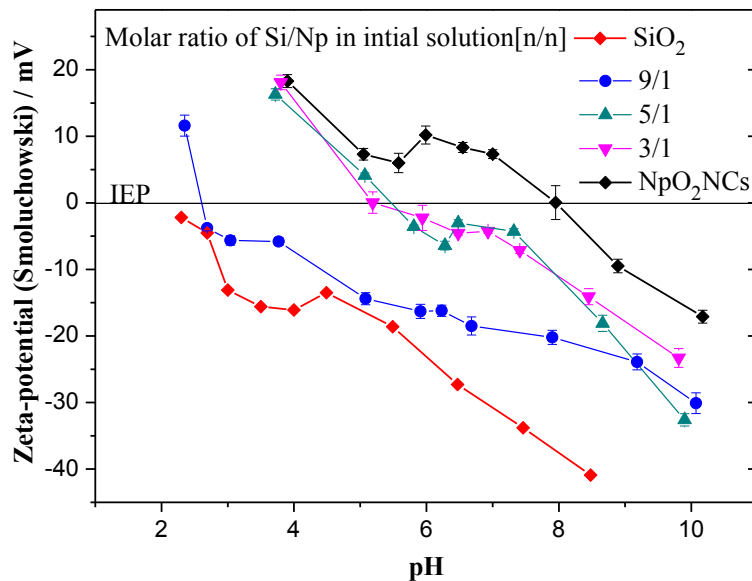


**Figure 29. Zeta-potential of Np(IV) nanoparticles in dependence on pH and silicate content** ( $[\text{Np}] = 5 \cdot 10^{-4} \text{ M}$ ;  $[\text{Si}] = 0 - 45 \cdot 10^{-4} \text{ M}$ ; initial  $0.1 \text{ M NaHCO}_3$ ). Error bars are given at the 95% confidence level; data of  $\text{SiO}_2$  from [49].

In general, Np(IV) silica particles precipitated from silicate solutions around the MWSA ( $[\text{Si}/\text{Np}] = 3/1$  and  $5/1$ ) appeared positively charged at acidic conditions  $\text{pH} = 4\text{-}5$  with  $\zeta = (+) 3$  to  $25 \text{ mV}$  and negatively charged at alkaline conditions  $\text{pH} = 7\text{-}10$  with

$\zeta = (-) 3$  to  $(-) 25$  mV with an average isoelectric point (IEP) of  $\sim 5$ . At IEP, which is defined by the pH range where the electrophoretic mobility is zero, the particles are characterized without effective electrical net charge.[132, 133] For instance, under ambient conditions the NpO<sub>2</sub> NCs can be characterized as an uncharged system in absence of silica: the NpO<sub>2</sub> NCs particle surface was characterized without an effective net charge ( $\zeta = 0$  mV) in bicarbonate background at  $\text{pH}_{\text{IEP}} = 8.0$ . The lack of an effective surface charge prevents the effective repulsive forces between the NCs. This allows closer approach of the particles, due to an increased degree of Van-der-Waals attraction and promotes agglomeration. Repulsive forces stabilize colloidal systems, and the absence of repulsive forces, caused by surface charge of the NpO<sub>2</sub> particles, initiates the tendency of particle-particle interaction during Brownian motion resulting in precipitation within a few hours after re-dispersion. This precipitation-dispersion process of NpO<sub>2</sub> NCs was repeatable (cf. section 3.4.) and the rapid agglomeration of NCs in ambient conditions is explained by absence of repulsive electric double-layer forces caused by their high IEP at  $\text{pH} = 8.0$ . A similar  $\text{pH}_{\text{IEP}} = 8.1$  was determined for Th(IV) oxyhydroxide particles in previous studies.[50]

**Table 8. Isoelectric points of actinide oxide particles, An(IV) silica colloids and silica particles.**

Material	Description	Background	$\text{pH}_{\text{IEP}}$	Reference
NpO <sub>2</sub> NCs	Agglomerates of NCs	0.05 M NaHCO <sub>3</sub>	8.0	This work
Th(IV) particles	Th(IV) oxyhydroxide	0.05 M NaHCO <sub>3</sub>	8.1	[50]
Pu(IV) colloids	Pu(IV) oxyhydroxide	-	8.6	[43]
Np(IV) silica colloids	Molar ratio [Si/Np] = 9/1	0.05 M NaHCO <sub>3</sub>	2.6	This work
Th(IV) silica colloids	Molar ratio [Si/Th] = 10/1	0.05 M NaHCO <sub>3</sub>	4.6	[50]
U(IV) silica colloids	Molar ratio [Si/Th] = 3/1	0.1 M NaHCO <sub>3</sub>	$\sim 4.4$	[49]
SiO <sub>2</sub>	-	-	2.0	[134]
SiO <sub>2</sub>	Ludox, nanosized particles (~12 nm in diameter), Aldrich	0.05 M NaHCO <sub>3</sub>	$\sim 2.4$	[50]
SiO <sub>2</sub>	Merck	0.01M NaCl	<3	[135]
SiO <sub>2</sub>	Davisil, Aldrich	0.001 M KCl	3.5	[136]

In contrast, the silica enriched Np silica nanoparticles generated above the MWSA ( $[\text{Si}/\text{Np}] = 9/1$ ) carried exclusively negative surface charge in nearly the whole pH range from pH = 3-10 with  $\zeta = (-) 5$  to  $(-) 30$  mV.

Due to the influence of silicate, the zeta potentials of all silica samples were shifted to more negative values below pH 7. A silica uptake in excess, related to Np into particle structure, shifted the IEP of the particles from  $\text{pH}_{\text{IEP}} 8.0$  to  $\text{pH}_{\text{IEP}} 2.6$ . This resulted in a negative charge of silica rich particles at ambient conditions and supported the electrostatic stabilization.

These Np silica systems can be described as colloidal stabilized dispersions, in which the double layer barrier prevents colloids to flocculate. The silica enriched Np particles, precipitated in nearly tenfold silica excess, were positively charged at  $\text{pH} < 2.7$ . The silica enriched Np particles surface charge correlates with the pH-dependent surface charge of the  $\text{SiO}_2$  reference system. The determined IEPs of various An(IV) particles in dependence on silica content are listed in Table 8 and compared to the IEP of reference material.

The surface charge of the untreated An(IV) oxide or oxyhydroxide particles at slight alkaline pH is weak and the corresponding IEP are  $\text{pH} \sim 8$ , i.e. to neutral pH. In contrast, all An(IV) particles formed in presence of silica show a shift in IEP to lower values of around 3 to 4, close to the IEP of pure silica. It must be considered that the sample background might influence the magnitude of the IEP.[137-141] The ionic strength and the type of ions can significantly shift the IEP value as observed in different investigations of the IEP of  $\text{SiO}_2$  (Table 8). A slight variation of determined IEP might be caused by slight variations in sample composition. However, it is obvious that An(IV) silica colloids possess similar surface charge characteristics and IEPs in comparison to the surface characteristics of environmentally relevant colloids with a silica-rich composition. Such colloidal systems are bentonite and smectite colloids originating from the erosion of silica dominated mineral structures.[43, 142] For instance, such smectite colloids are negatively charged over a widespread pH range (pH 1.2 to pH 9.0).[43]

A theory to explain their colloidal stability, the Derjaguin-Landau-Verwey-Overbeek-Theory (DLVO-theory) describes the force between charged surfaces that interact through a liquid medium. The DLVO-theory takes both the van-der-Waals attraction and the electrostatic repulsion into consideration. At high ionic strength the colloids tend to aggregate when the colloidal charge exceeds the charge of the double layer. Accordingly, at low ionic strengths the colloids remain in dispersion, since the double layer barrier prevents colloids from flocculation.[133, 143-145] The investigation of the colloidal stability of bentonite colloids and smectite colloids in solution under similar environmental conditions as a function of pH and ionic strength revealed that natural colloids were stable at lower ionic strengths of 0.01 and 0.001 M but unstable at a higher ionic strength of 0.1 M.[43, 142] Interestingly, the colloidal stability of

Np(IV) silica colloids generated under conditions exceeding the previously mentioned stability level at lower ionic strength (0.05 M) might be in contradiction to the DLVO-behavior of e.g. bentonite colloids. The stability of these Np(IV) silica colloids can also be explained by taking the so-called, non-DLVO-behavior into consideration.

In general, Np(IV) silica colloids might prove to be relatively stable, because both (i) a considerable repelling electrostatic force (i.e., a DLVO force) accompanied by a shift of the IEP to lower pH values and (ii) significant non-DLVO forces due to the increased influence of silica stabilize them.[146]

In absence of silica in An(IV) systems at  $\text{pH} > 5$ , e.g. Pu(IV) colloids are unstable at all ionic strength values tested.[43] This instability could be due to strong colloid-colloid attractive van-der-Waals interactions that outweigh the repulsive electric double layer interactions in dependence on the bicarbonate solution. Therefore, under the pH range of most groundwater aquifers (typically between 5 and 9), e.g. Pu(IV) colloids exists as aggregates of several primary particles rather than single particles [43, 147], and the observed behavior of  $\text{NpO}_2$  NCs in this study is consistent.

A structural explanation for the colloidal stabilization of silica enriched Np(IV) particles could be the enrichment of silanol-groups at the particle surface, which is supported by results of the average elemental composition (Table 7; Figure 36). This induces a pronounced negative surface charge at near neutral pH, which guarantees the presence of repulsive forces between the colloidal particles. This prevents agglomeration caused by particle-particle interactions and attraction.

### 4.3 Internal structure of Np(IV) silica nanoparticles

Generally, in environmental related samples of complex composed matrices, competitive redox processes of various actinide redox couples[148, 149] were observed, for instance the Np(V)/Np(IV) redox couple in presence of humic acids.[149] In this section, the dilution of the initial Np(IV) solution in presence of silicic acid and the subsequent formation of Np silica particles was investigated by XANES spectroscopy. No significant shift of the Np  $L_{III}$ -edge XANES edge position (Figure 30 and Table 9) was observed. The formation of pentavalent Np can be ruled out by comparison of the XAS data with reference material of aqueous Np(V) (Figure 49 in Appendix, Table 9). The presence of pentavalent Np would generate a significant shift of the XANES edge to lower energy[150], coincident with the characteristic oscillation feature at higher energy (highlighted by arrow in Figure 49) originating from the transdioxo-cation (i.e. actinyl ion  $\text{AnO}_2^+$ ) structure in solution.[104, 151-153] The tetravalent state was preserved even after the precipitate formation.



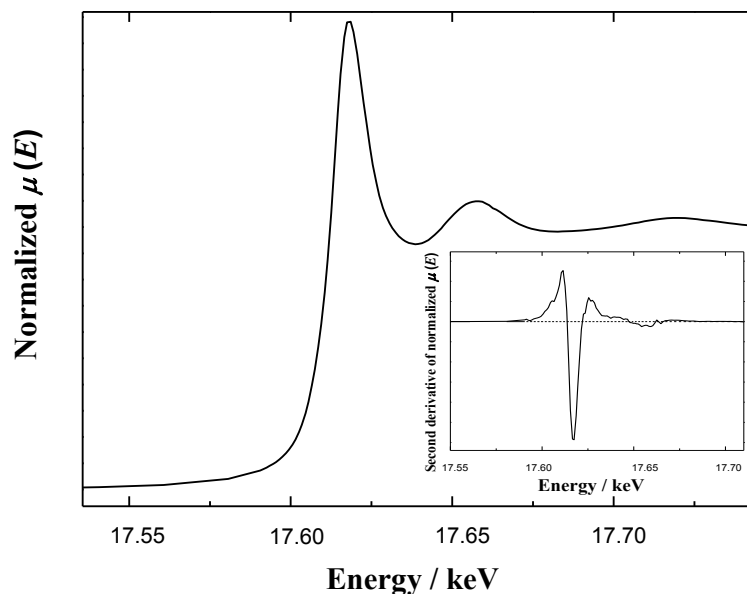


**Figure 30. Normalized Np L<sub>III</sub>-edge XANES spectrum for Np(IV) silica nanoparticles.**  $[(\text{Np},\text{Si})\text{O}_n(\text{OH})_{4-n}\cdot x\text{H}_2\text{O}]^{4-2n-(4-n)}$  precipitated in 0.1 M  $\text{NaHCO}_3$  and corresponding second derivative (inset).

**Table 9. XANES edge position at Np L<sub>III</sub>-edge.**

Sample	Edge position / keV
Np(IV) silica particles	17.6137
Np(IV) in 1 M $\text{NaHCO}_3$	17.6134
Np(V) in 1 M $\text{HNO}_3$	17.6119

Np(V) edge from spectrum given in Figure 30. The edge position is defined at the first inflection point. Np(V) XANES edge shown in Appendix Figure 49.

Note that the absorption edge intensity can also slightly vary with the degree of condensation of the sample phase.[104, 150, 154] Actinide appearance in the colloidal state might provoke minor broadening of the white line.

These intensity differences can lead to errors in individual concentration determinations of Np(IV) and Np(V) in mixtures through linear combination of XANES spectra from reference compounds, if the degree of condensation of the unknown differ highly from reference compounds.[150] Figure 31 shows the  $k^3$  weighted Np L-edge EXAFS spectrum (left) and the corresponding Fourier transforms (FT, right) of the Np(IV) silica colloids. The corresponding EXAFS fit parameters are given in Table 10. The spectrum of the colloidal Np(IV) silica particles exhibits a strong dampening of the EXAFS oscillation, related to a peak broadening in the Fourier transform and a large Debye-Waller factor  $\sigma^2$  (Figure 31, Table 10). These spectral features indicate a large structural disorder in the colloid structure.

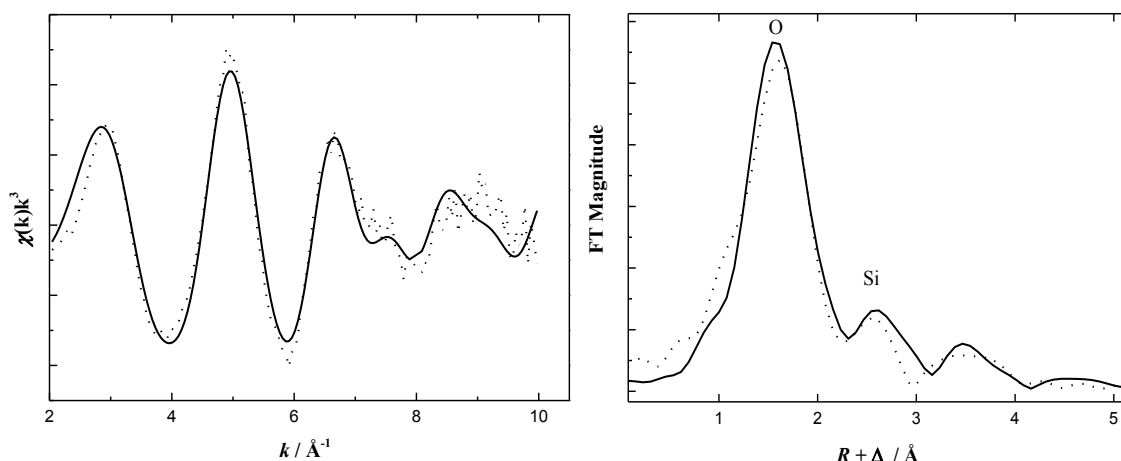


**Figure 31. EXAFS of Np(IV) silica colloids.**

(left side)  $k^3$ -weighted Np L<sub>III</sub>-edge EXAFS spectrum for Np(IV) silica nanoparticles  $[(\text{Np},\text{Si})\text{O}_n(\text{OH})_{4-n}\cdot x\text{H}_2\text{O}]^{4-2n-(4-n)}$  precipitated in 0.1 M NaHCO<sub>3</sub> and (right side) corresponding Fourier transform (FT). Solid lines, experimental data; dotted lines, theoretical fit; phase shift ( $\Delta$ ) is not corrected on FT.

**Table 10. Structural parameters of Np(IV) silica particles  $[(\text{Np},\text{Si})\text{O}_n(\text{OH})_{4-n}\cdot x\text{H}_2\text{O}]^{4-2n-(4-n)}$  obtained from theoretical curve fitting.**

Scattering path	$R / \text{\AA}^a$	$CN^b$	$\sigma^2 / \text{\AA}^2$	$\Delta E_{k=0} / \text{eV}$	$F$
Np–O	2.28 (1)	7.1 (2)	0.017 (4)		
Np–Si	3.11 (1)	1.3 (1)	0.0091 (2)	-9.3	0.07
Np–Np	3.75 (1)	1.1 (1)	0.0098 (1)		

<sup>a</sup> Interatomic distance ( $R$ ), errors  $\leq \pm 0.02 \text{\AA}$ , <sup>b</sup> Coordination number  $CN$ , errors  $\leq \pm 15\%$ .

Standard deviations are given in parentheses.

The oxygen coordination sphere was calculated to an Np–O distance of  $R + \Delta = 2.28 \text{\AA}$ . If pentavalent Np should contribute to the internal structure, the Np–O distance should be shorter than  $R + \Delta = 2.28 \text{\AA}$ . It is well-known that pentavalent actinides generally form actinyl cation ( $\text{AnO}_2^+$ ) structures described with transdioxo structure ( $\text{O}_{\text{ax}}$ ).

In general, this transdioxo structure generates an intense single scattering peak around short distance  $R + \Delta = 1.5 \text{\AA}$  in EXAFS-FT spectra.[70, 151-153, 155, 156] It was not necessary to consider such short Np–O bonds during fitting procedure, thus, a significant contribution of Np(V) due to possible redox processes is not indicated and the presence of pentavalent Np can be ruled out in the formation of Np(IV) silica nanoparticles.

A small peak occurs in the Fourier transform which indicates silicon atoms in the environment of neptunium with a Np–Si distance of  $3.11 \text{\AA}$ . This short Np–Si distance is characteristic of silica in bidentate coordination, while monodentate coordination would result in a significantly longer Np–Si distance

A small but less specific peak at a larger distance may indicate Np-Np interactions. It follows that, as for uranium(IV)-silica colloids and thorium(IV)-silica colloids,[49, 50] also in the case of neptunium(IV)-silica colloids, the actinide-oxygen-actinide bonds are increasingly replaced by actinide-oxygen-silicon bonds, i.e. silica was included into the structure of the solid if the solution contains silicic acid.

#### 4.4 Electronic structure of long-term stabilized Np(IV) silica colloids

The electronic structure of long term stabilized Np silica colloids was further investigated by XPS. The survey spectrum of the BEs is shown in Figure 32. The sample was deposited directly from dispersion in  $\text{NaHCO}_3$  by drying at RT on a HOPG sample holder. The spectrum revealed various clear peaks deriving from Na, Np, O, and Si electrons and from the sodium bicarbonate background including O KLL and CKLL Auger electrons. The dominant C 1s peak at 285 eV (referenced again for BE calibration) and the C KKL Auger peaks ( $\sim 1013$  and  $\sim 994$  eV) originate from the carbon of the sample holder and bicarbonate background and appear more intensive than in XPS of cleaned  $\text{NpO}_2$  NCs (cf. section 3.3.). Even Auger peaks for oxygen were observed around 770 eV next to the O 1s electron state around 530 eV. Np was indicated again by a typical split of the Np 4*f* core level resulting in a doublet around 405 eV and 416 eV.

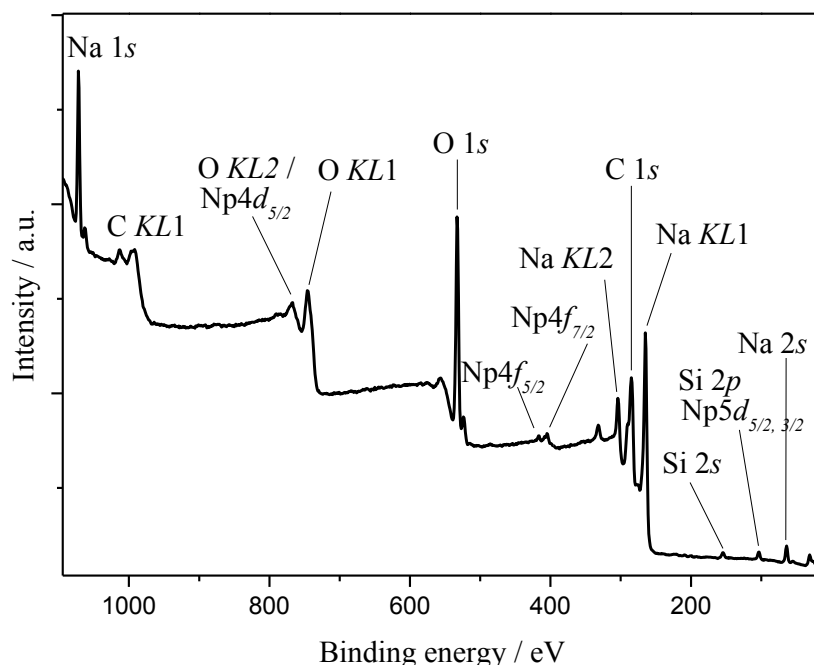
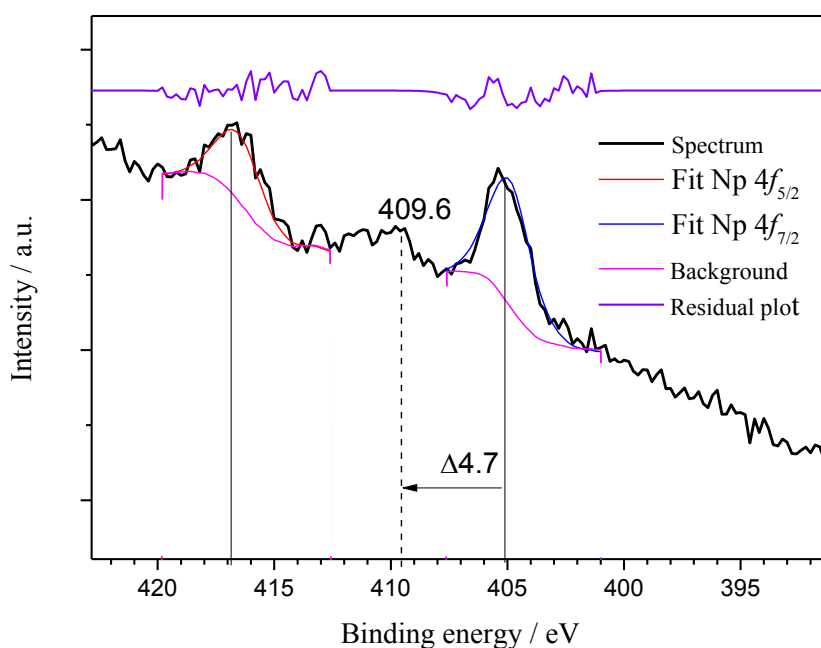


Figure 32. Survey XPS of potentially long term stabilized Np(IV) silica colloids.

The levels Np  $4f_{7/2}$  and Np  $4f_{5/2}$  (shown in Figure 33 and Figure 50-Appendix) were determined at  $404.9 \pm 0.2$  eV BE and  $416.5 \pm 0.2$  eV BE with the same spin-orbit split  $\Delta E_{sl}$  (Np  $4f$ ) = 11.6 eV of NpO<sub>2</sub> NCs. A satellite peak was determined at higher BE with  $\Delta E_{sat} = 4.9$  corresponding to Np  $4f_{7/2}$  BE (see also Figure 51 in Appendix). In comparison to the  $4f$  core level of NpO<sub>2</sub> NCs the BE in presence of silicate were slightly shifted ( $\sim 0.5$  eV) to lower BEs, presumably due to slight charging effects of the bicarbonate background in the dried state during measurement.



**Figure 33. Np  $4f$  core level XPS of long term stabilized Np(IV) silica colloids**

**Table 11. Electron BE of long-term stabilized Np(IV) silica colloids at 1253.6 eV**

Core level	Electron BE [eV]	FWHM [eV]	$\Delta E$ [eV]
Np $4f_{5/2}$	$416.5 \pm 0.2$	2.3	$\Delta E_{sl} = 11.6$
Np $4f_{7/2}$	$404.9 \pm 0.2$	2.2	
Satellite Np $4f_{7/2}$	$409.6 \pm 0.2$	-	$\Delta E_{sat} = 4.7^*$
O $1s$	533.4	-	-

\* = related to corresponding Np  $4f_{7/2}$  core level

The characteristic satellite peaks with  $\Delta E_{sat}$  (Np 4*f*)  $\sim 6.9$  eV indicative of the fluorite structure were not observed. Nevertheless, one satellite corresponding to Np 4*f*<sub>7/2</sub> level was indicated at  $409.6 \pm 0.2$  BE with  $\Delta E_{sat} = 4.7$  eV. Its origin is unknown and can be speculated to be an indication of a different internal structure in Np(IV) silica colloids compared to the fcc structure of NpO<sub>2</sub>.

The long term stabilized Np(IV) silica colloids revealed a significant O 1*s* peak at 533.4 eV (Figure 34). The O 1*s* energy in pure  $\alpha$ -SiO<sub>2</sub> and other similar silicates show a BE of 532.9 eV, which is  $\sim 3$  eV higher than the O 1*s* BE of oxygen in e.g. An(IV) oxides.[50, 157, 158]

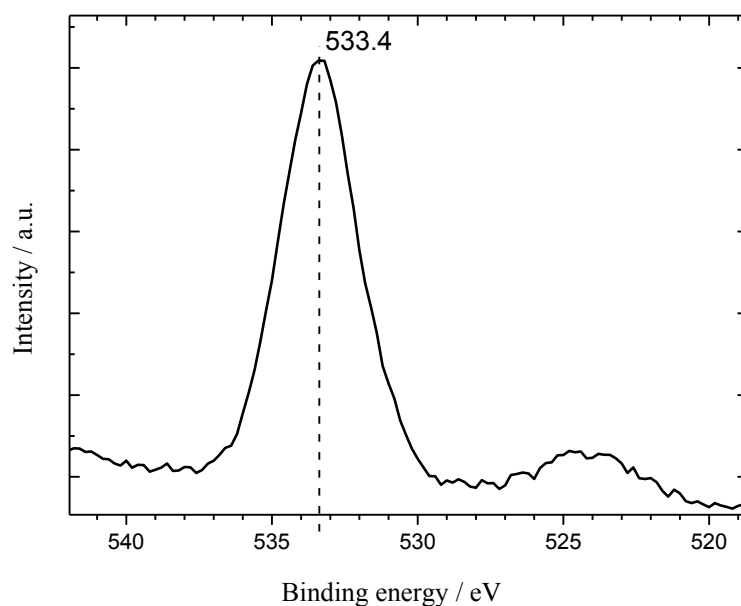


**Figure 34. XPS O 1*s* core level of aged Np(IV) silica colloids.**

## 4.5 Morphology of Np(IV) silica colloids

### 4.5.1 Effect of initial silica concentration on the morphology of Np(IV) silica colloids

Particles precipitated from different Np(IV) silica systems were further characterized by TEM. In Figure 35 some silica-containing particles isolated from a stabilized dispersion of the Np(IV) silica system ( $\text{Si/Np} = 9/1$ ) are shown at different magnifications. Various particles with an average diameter of  $\sim 45$  nm (Figure 35-(A)) are shown consolidated with each other and displayed diffuse scattering characteristics without defined reflections (Figure 35-(B)). Single isolated nanoparticles with a diameter of  $\sim 40$  nm (Figure 35-(C)) and  $\sim 20$  nm (Figure 35-(D)) were also observed and further investigated on their elemental composition (Figure 36).

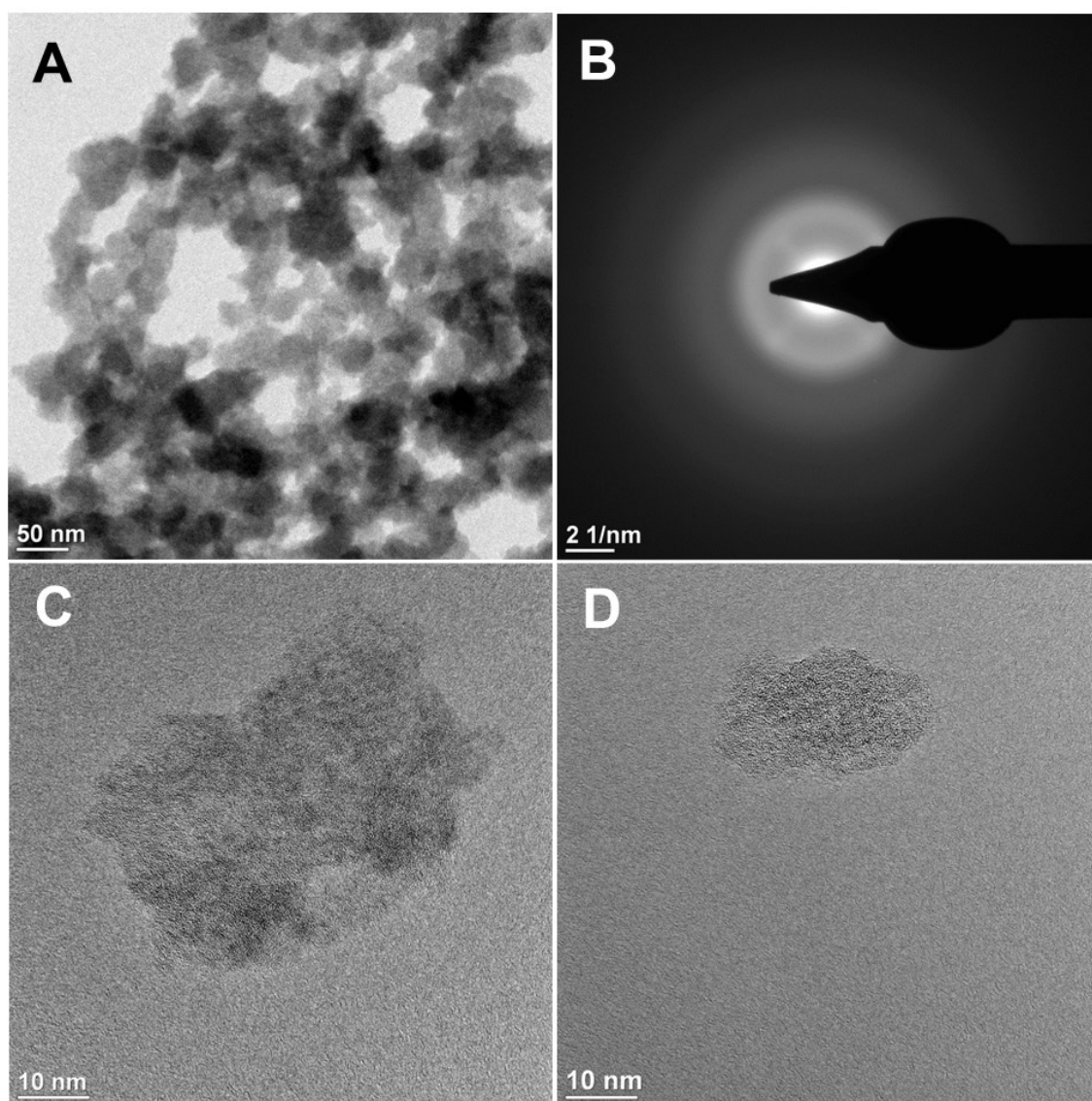


**Figure 35. TEM data of silica-enriched Np(IV) silica colloids**

(A) Bright field TEM micrograph of agglomerated Np(IV) silica colloids,  
(B) experimental SAED ring pattern,  
(C) and (D) HR-TEM image of isolated Np(IV) silica nanocolloids of different size;  
[Np] =  $1 \cdot 10^{-3}$  M, initial silicate: [Si] =  $8.6 \cdot 10^{-3}$  M ( $\text{Si/Np} = 9/1$ ); initial 0.1 M  $\text{NaHCO}_3$ .

The particle morphology can be described as irregular. No distinguishable lattice structures like in  $\text{NpO}_2$  NCs were observed. The irregularly structured particles appeared in an amorphous solid state. Incoherent imaging with HAADF-STEM, by which the intensity correlates with the atomic number, located compartments of different dense phases in the interior of an isolated nanoparticle (Figure 36-(A)). Two exemplary areas of different contrast were selected and further investigated on their elemental composition. Area 1, with a less intensive contrast, revealed  $\sim$ two-times the magnitude of silicon than Np, whereas area 2, with an intensified contrast, revealed  $\sim$ three-times the magnitude of silicon than Np, whilst the Np concentration was the same in both areas.

This implicates that the compartments with intensified contrast were provoked by silicate-enrichment at the same Np concentration although silicon, with a much lower atomic number compared to Np, would normally appear as less dense matter in STEM. The colloid structure between bulk and surface was not homogenous.

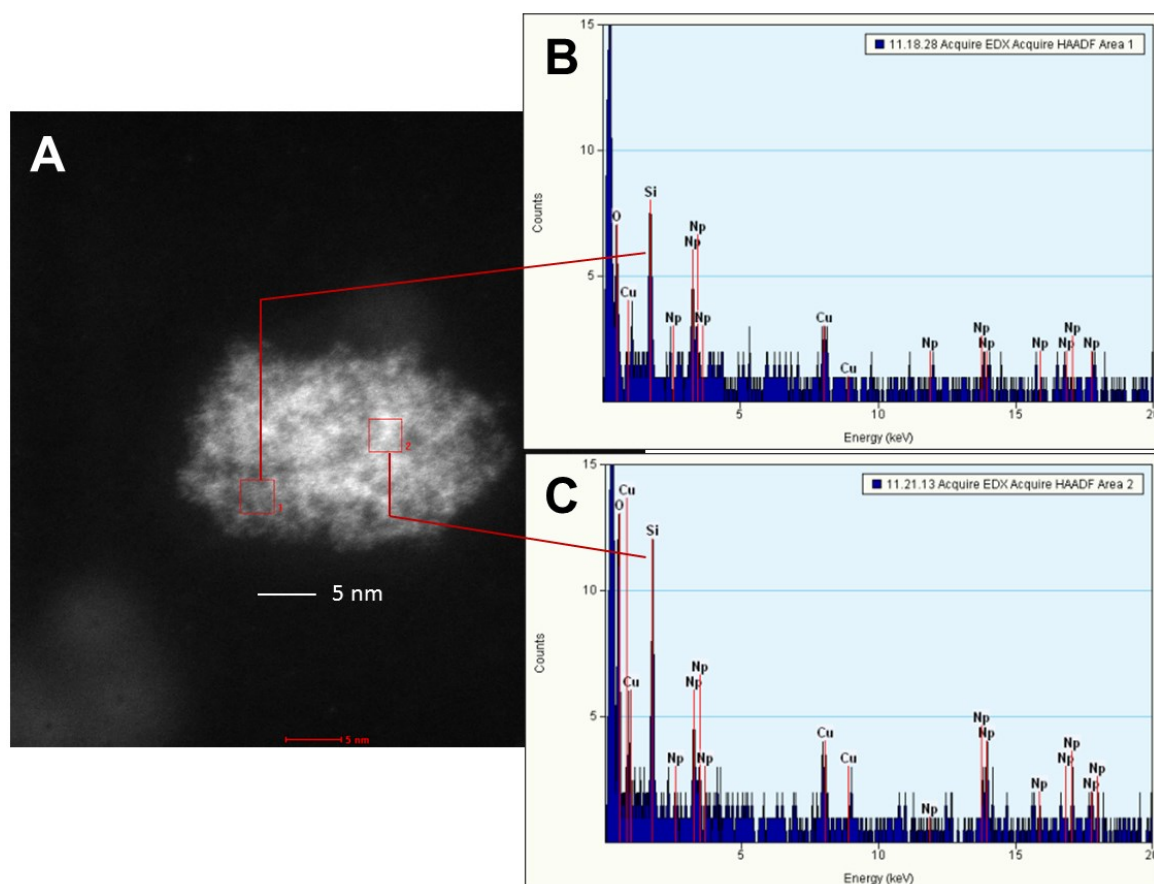


**Figure 36. HAADF-STEM micrograph and EDX of silica-enriched Np(IV) silica colloid**  
 (A) HAADF-STEM micrograph of Np(IV) silica nanoparticle corresponding to Figure 35-D,  
 (B) EDX spectrum of selected area 1 in A,  
 (C) EDX spectrum of selected area 2 in A;  
 $[\text{Np}] = 1 \cdot 10^{-3} \text{ M}$ , initial silicate:  $[\text{Si}] = 8.6 \cdot 10^{-3} \text{ M}$  ( $\text{Si}/\text{Np} = 9/1$ ); initial  $0.1 \text{ M NaHCO}_3$ .

Nonhomogenous distribution of Si in single An(IV) silica particles was also reported for Th(IV) silica colloids. In this case, the silicate was much more concentrated at the particle surface than in the particle interior.[50] It must be mentioned that layers or phases with similar elemental composition and a certain height and contrast would also provoke such differences in contrast if the organization of different multi-layers or differences in particle-height are given.

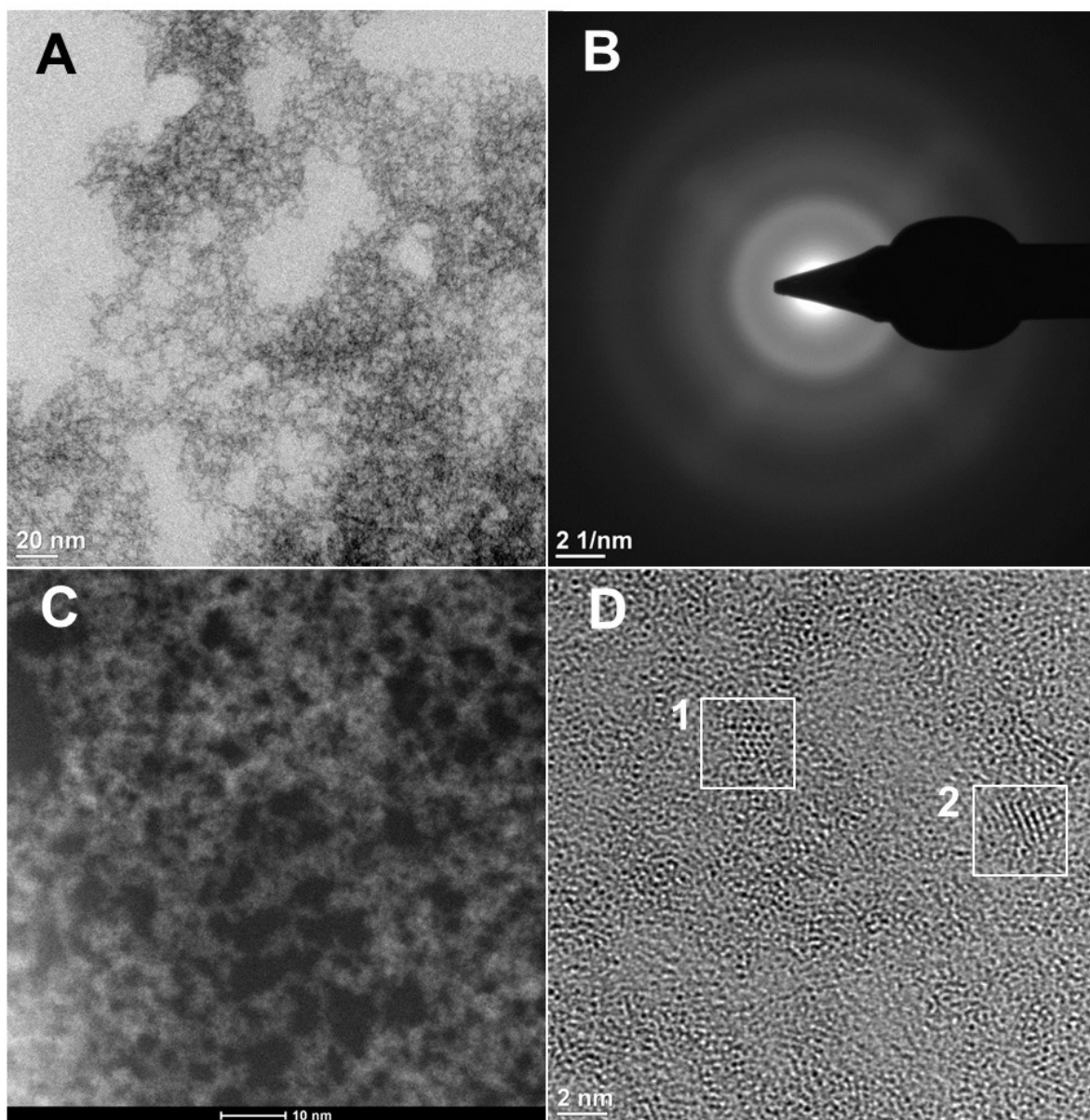


**Figure 37. TEM data of silica-poor Np(IV) silica particle**

(A) Bright field TEM micrograph of a compartment of micron-sized Np(IV) silica particle,  
(B) experimental SAED ring pattern,  
(C) HAADF-STEM micrograph of Np(IV) silica particle compartment,  
(D) HR-TEM image of Np(IV) silica particle compartment;  
[Np] =  $1 \cdot 10^{-3}$  M, initial silicate: [Si] =  $1.8 \cdot 10^{-3}$  M (Si/Np = 1.8/1); initial 0.1 M NaHCO<sub>3</sub>.



By combining the results of HR-TEM and incoherent imaging with elemental analysis from Figure 35 and Figure 36, silica-enriched Np(IV)-particles can be interpreted as irregularly structured particles of spherical shape with amorphous phases of partially different Si concentrations in composition.

In contrast, TEM of silica-poor systems revealed particles in the micron-range that consisted of irregularly cross-linked hydrolyzed Np(IV) silica compartments (Figure 37). These cross-linked compartments appeared as amorphous phases, too. No clearly defined reflections were determined (Figure 37-(B)). Neither HR-TEM nor high-angle annular dark-field scanning transmission electron microscopy (HAADF-STEM) showed single nanoparticles of small size. Exclusively porous micron-sized particles with pores <15 nm were observed. Some cross-links of the irregularly arranged compartments of hydrolyzed Np(IV) silica material revealed sparsely distributed ultra-small compartments that possess well-ordered lattice structure (Figure 37-(D), areas 1 and 2). These well-structured compartments may originate from partially localized Np(IV) oversaturation in solution during particle growth under the condition of silica deficiency. Therefore, the lack of silicate would provoke the formation of local  $\text{NpO}_2$ -like structures, whereas even the presence of low concentrations of silicate still results in the formation of disordered Np(IV) structures. Therefore, in silica-poor systems the formation of single isolated nanoparticles was prevented. In contrast, silica-enriched systems could be characterized by isolated small particles with an average particle size of 45 nm (Figure 38-(A)).

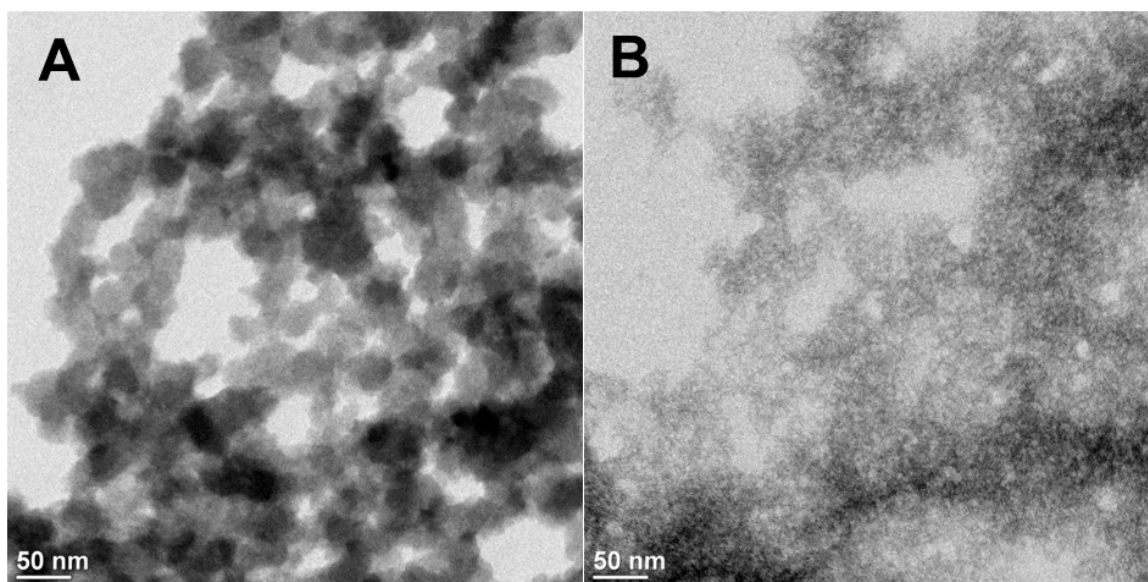


**Figure 38. Morphology of silica-enriched Np(IV) silica colloid structure versus structure silica-poor Np(IV) silica particle**

(A) Bright field TEM micrograph of silica-enriched Np(IV) silica colloids,  $[\text{Np}] = 1 \cdot 10^{-3} \text{ M}$ , initial silicate:  $[\text{Si}] = 8.6 \cdot 10^{-3} \text{ M}$  ( $\text{Si}/\text{Np} = 8.6/1$ ); initial  $0.1 \text{ M NaHCO}_3$ ;  
(B) Brightfield TEM micrograph of silica-poor Np(IV) silica particle compartment,

$[Np] = 1 \cdot 10^{-3}$  M, initial silicate:  $[Si] = 1.8 \cdot 10^{-3}$  M (Si/Np = 1.8/1); initial carbonate  $1 \cdot 10^{-2}$  M.

These particles appear as consolidated/compact amorphous solids with a densely closed surface and exhibit no internal fractures like silica-poor particles in the micron-range (Figure 38-(B)).

Differences in the resulting particle morphology were also observed in the arrangement of fractal  $SiO_2$  clusters in dependence on silica concentration. Herein, the differences could be monitored by UV-vis-NIR absorption spectroscopy due to different Rayleigh scattering characteristics.[159]

The morphology of silica-enriched Np(IV) silica particles with densely closed surface and spherical shape might facilitate the migration behavior of Np(IV) in a stabilized colloidal form under environmental conditions. In combination with the silica enriched surface which was indicated by the present TEM-EDX results in Figure 36 and the significant effective surface charge of silica-enriched particles shown in Figure 29, this type of An(IV) silica colloids might be stabilized as a colloidal dispersion under ambient conditions in the near- or far-field of a HLW repository. Larger sized particles lacking in silica and a less effective surface charge might be unable to form stable colloids, i.e., this type of particles would rather be retarded in solution due to filtration effects or would be immobilized by precipitation.

Spherically shaped nanoparticles with a densely closed surface and a high effective surface charge were also observed in more diluted samples under conditions close to environmental parameters (Figure 39) highlighting the importance of Np(IV) silica particles under ambient conditions.

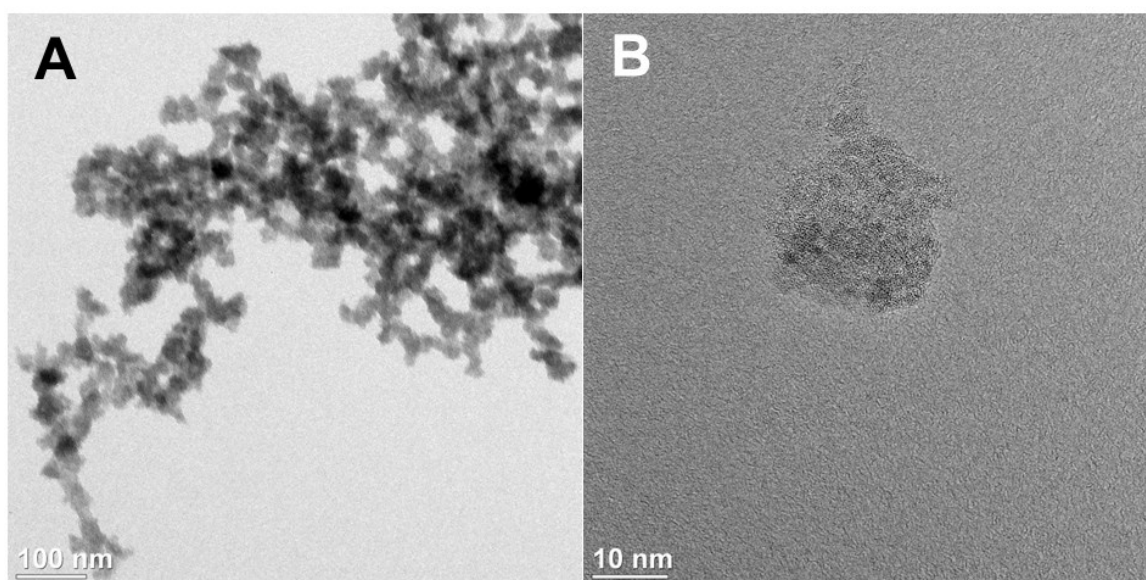


**Figure 39. TEM data of silica-enriched Np(IV) silica colloids**

(A) Brightfield TEM micrograph agglomerated Np(IV) silica colloids,

(B) HR-TEM image of Np(IV) silica particle;

$[Np] = 2.5 \cdot 10^{-4}$  M, initial silicate:  $[Si] = 2.5 \cdot 10^{-3}$  M (Si/Np = 6/1); initial 0.1 M  $NaHCO_3$ .

#### 4.5.2 Morphology of long-term stabilized Np(IV) silica colloids

In order, to evaluate changes in morphology of Np(IV) silica colloids over time, a 370 days aged sample ( $[\text{Np}] = 1 \cdot 10^{-3} \text{ M}$  with initial silicate  $[\text{Si}] = 9.0 \cdot 10^{-3} \text{ M}$ ;  $\text{Si/Np} = 9/1$ ) was investigated by TEM. Silica-enriched Np(IV) particles were directly isolated from the long-term stabilized colloidal dispersion without further purification steps. Note that no apparent precipitation process was observed in the mother dispersion during aging, emphasizing the stability of the colloids at near-neutral pH. The silica-enriched dispersion was colloidal stabilized until the desired measurement. At the time of particle isolation for TEM sample preparation the redox potential was  $E_h = (-) 76 \text{ mV}$  in solution at RT. A significant SLI was measured at 150 kcps and the PSD (light intensity weighted) was determined in a particle mixture with diameters of  $\sim 40\text{-}50 \text{ nm}$  and a minor fraction of  $\sim 900 \text{ nm}$ .

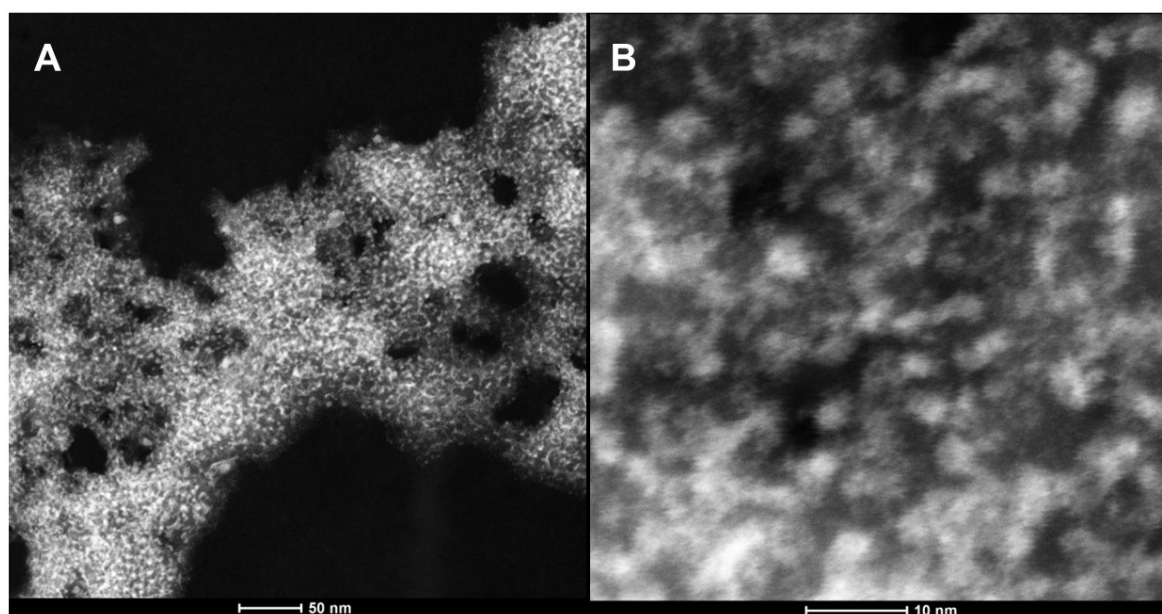


**Figure 40. HAADF-STEM micrographs of aged Np(IV) silica colloids in different magnifications: (A) 160kx and (B) 1300kx.**

$[\text{Np}] = 1 \cdot 10^{-3} \text{ M}$ , initial silicate:  $[\text{Si}] = 9.0 \cdot 10^{-3} \text{ M}$  ( $\text{Si/Np} = 9/1$ ); initial carbonate  $1 \cdot 10^{-2} \text{ M}$ .

In Figure 40 amorphous Np(IV) silica structures were observed by HAADF-STEM. These structures contained inclusions or attachments of material with higher density in/on the amorphous silica containing matter of low density. The spots/dots of higher electron density were distributed consistently over the agglomerated Np(IV) silica particle material. Corresponding HR-TEM and electron diffraction results (shown in Figure 41) demonstrate that in addition to the amorphous phase with corresponding diffuse diffraction properties, some clear rings of diffraction characteristics originating from the fcc structure were indicated.

Similar HAADF-STEM images of actinide bearing material with different density or phase mixtures were observed in other studies of fine atmospheric particulates from Detroit urban area emitted from coal-burning power plants. Herein, crystalline uraninite particles of less than 10 nm in size were encapsulated in a cage structure of fulleroid in atmospheric particulates.[160]

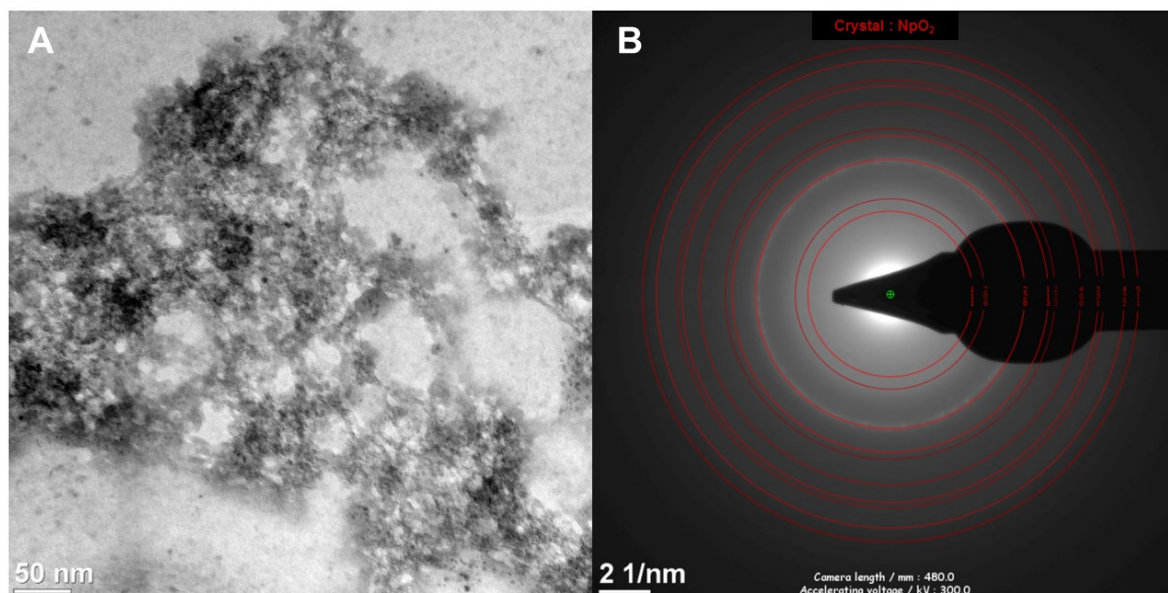


**Figure 41. TEM-Micrograph of potentially long-term stabilized Np(IV) silica colloids**

(A) HR-TEM micrograph of agglomerated Np(IV) silica colloids  
(B) SAED corresponding to (A).

More morphology details of the mixed phase particle material were observed by HR-TEM shown in Figure 42. It clearly revealed that the prevailing amorphous and irregular Np(IV) silica particle structure (exemplary shown in box 1 in (A), higher resolution in (D)) contained well-ordered and crystalline compartments (detail 2 – 5 in (A); detail 2 highlighted in (E)). The corresponding FFT of the mixed phases in (A) is displayed in box (B) and shows diffuse diffraction properties (like in Figure 41-(B)) caused by amorphous particle material next to clear reflections located on rings originating from highly ordered compartments with fcc structure. In box (C) the FFTs of some exemplary selected crystalline structures (corresponding details from (A)) revealed definite reflections of isolated crystalline compartments in dependence of crystal zone axis. It is speculative to whether the nanocrystalline phases were incorporated in the less dense amorphous phase or attached on the Np(IV) silica particle surface. The clearly resolved crystal lattice in Figure 42 detail 2 might be interpreted as thick crystal attached to the surface, while in detail 4 and 5 the crystalline phases could be interpreted as ultra-thin layer crystals or as weak contrast from incorporated crystalline phases in the interior of the prevailing less-dense amorphous structure of the Np(IV) silica colloid. Two-dimensional bright-field TEM analysis is inadequate for determining such complex morphologies in the third dimension (height) and occasionally

misleading for tomographic information. Modified electron tomography techniques are a better approach to determine the location of crystalline phases within the Np(IV) silica phase. For example energy-filtered (EF) TEM would determine the depth location, so the application of EFTEM is strongly recommended.[161] Ultra-small metal nanostructures ( $\sim 1$  nm) within a mesoporous silica were localized by applying this technique providing evidence that the nanostructures were anchored on the wall of mesopores.[162] By using a tilt series of EFTEM elemental maps, it would be possible to reconstruct a three-dimensional elemental distribution map.[163, 164]

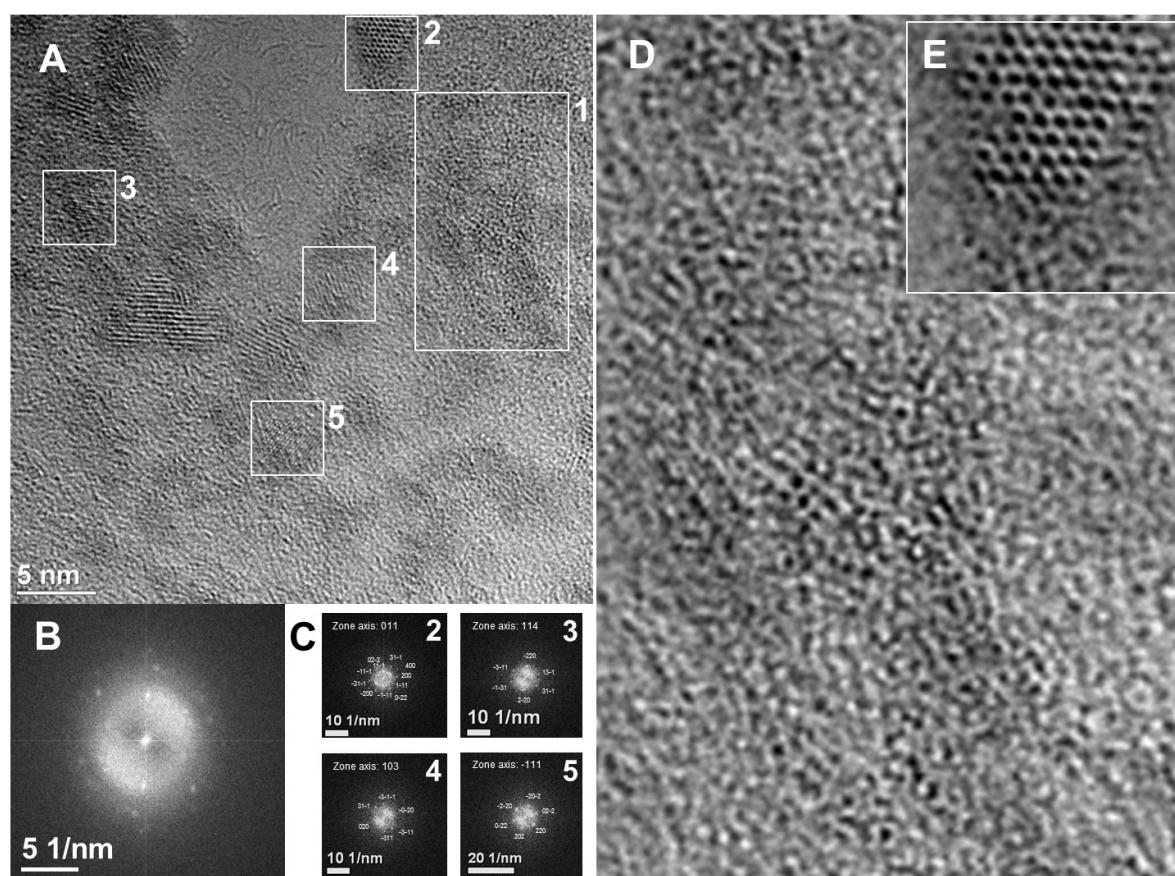


**Figure 42. HR-TEM of potentially long-term stabilized Np(IV) silica colloids**

(A) HR-TEM micrograph showing nanocrystalline structures in amorphous Np(IV) silica colloids, (B) FFT corresponding to micrograph (A), (C) FFTs corresponding to selected areas in micrograph A, (D) Detail of micrograph in A, area 1 (E) Detail of micrograph in A area 2 reveals well-organized fcc structure.

Concerning the structural aspects of the crystalline phase itself, the determined SAED rings and reflections were always in accordance to the fcc structure. The fcc structure does not only exclusively characterize the fluorite structure of  $AnO_2$  but also the fcc structure of actinide oxides of lower valency like trivalent An sesquioxides ( $An_2O_3$ ).

The diffraction rings in Figure 41-(B) could indicate cell parameters in the crystal phases slightly smaller than normally observed for  $\text{NpO}_2$ . This led to the additional consideration that the sesquioxide structure, which is characterized by slightly smaller cell parameters than those of the  $\text{AnO}_2$  counterpart, might also play a role. Note that further investigation with crystallographic methods is required herein to determine the actual cell parameters.

Sesquioxides are known for neptunium, plutonium and the heavier actinides. Regarding plutonium, the sesquioxide is characterized by a thermodynamically stable oxide structure. Hitherto,  $\text{Np}_2\text{O}_3$  was regarded as an unstable actinide oxide species which only appears as a metastable intermediate.[20] In contrast to  $\text{Pu}_2\text{O}_3$ ,  $\text{Np}_2\text{O}_3$  was evaluated to be stabilized only in trace concentration or ultra-thin layers under strongly reducing and well-defined conditions on the Np metal surface, but not in the bulk of Np oxide structures.[20, 165] As recently observed in water sorption/desorption processes on  $\text{NpO}_2$ , it was shown under definite conditions that water reduced the surface of  $\text{NpO}_2$  to  $\text{Np}_2\text{O}_3$ .[165] This phenomenon was observed by applying ultraviolet photoemission spectroscopy (UPS), which is much more sensitive in determining the electron structure in the valence band instead of the core level states of Np from which the sesquioxide structure is hardly verifiable. This new study confirmed that  $\text{Np}_2\text{O}_3$  can be present as a stable species (by determination of the  $5f$  state applying UPS) and points to the stability of the trivalent oxide, which might play a role under certain environmental scenarios also given in the recent study. Due to the similar fcc structure and the possibility of a bonding nature with slightly smaller cell parameters in the crystal phases, further investigation by UPS is recommended. The absence of the satellites at  $\sim(+)$  7 eV BE, typical indicators of  $\text{NpO}_2$  fcc structure, in the  $4f$  core level of aged Np(IV) silica colloids (XPS in Figure 33) could serve as an additional hint for the presence of  $\text{Np}_2\text{O}_3$ . The proof of the actual state of “fcc-masked” Np oxide structure in the crystalline phases on long-term stabilized Np(IV) silica colloids by UPS would determine if the presence of  $\text{Np}_2\text{O}_3$  phases should be considered or not. The exclusion of sesquioxide phases would confirm the absence of additional redox processes and further highlight the intrinsic property of Np(IV) to hydrolyze in the fcc structure even when incorporated with silica in the solid state over longer timespans of equilibration. To date, the bonding nature of long-term stabilized Np(IV) silica colloids is still not completely understood.

#### **4.6 The stabilization of Np(IV) silica colloids - Implication for potential migration behavior of An(IV)**

It has been proved that not only the “analogues” U(IV) and Th(IV), but also the highly radioactive Np(IV) itself is able to form silica-containing colloids. The assessment of Np behavior in the environment under reducing conditions should evaluate the role of such colloids, because the formation of silica-containing An colloids in the surroundings of a nuclear waste repository cannot be ruled out.[166] Np(IV) silica colloids might prove to be relatively stable because both, (i) a considerable repelling electrostatic force (i.e., a DLVO force) accompanied by a shift of the isoelectric point to lower pH values and (ii) significant non-DLVO forces due to the increased influence of silica in the colloids stabilize them.[50, 146] Special attention needs to be paid to a decrease of the ionic strength due to intrusions of electrolyte deficient water (e.g., glacial melt waters after a possible future ice age[167]), because decreasing ionic strength increases colloid stability. Furthermore, transport of Np(IV) silica colloids through the engineered barrier system (compacted bentonite) and through the fractures of crystalline host rock also cannot be ruled out. Macromolecules of about 5 nm (lignosulfate, 30 kDa) were observed to diffuse through the pores of bentonite independently of the bentonite density.[168] Humic substances and very small gold particles (2 nm), too, proved to be able to diffuse through compacted bentonite.[169, 170] However, slightly larger gold nanoparticles did not pass through compacted bentonite.[169, 171] The question whether or not Np(IV) silica colloids are able to pass through bentonite or fractured host rock needs clarification. If Np(IV) silica colloids can interact with other actinide colloids and stabilize them as pseudo-colloid carrier is unknown. Further research is needed to elucidate the potential role of Np(IV) silica colloids in environmental scenarios.



---

## 5 Summary

Considering the worldwide growing discharge of minor actinides and the current need for geological disposal facilities for radioactive waste, this work provides a contribution to the safety case concerning Np transport if it would be released from deep repository sites and moving from alkaline cement conditions (near-field) to more neutral environmental conditions (far-field). The reducing conditions in a nuclear waste repository render neptunium tetravalent, which is assumed to be immobile in aqueous environment due to the low solubility solution of Np(IV). For tetravalent actinide nuclides, the most significant transport should occur via colloidal particles. This work demonstrates the formation of intrinsic neptunium dioxide nanocrystals and amorphous Np(IV) silica colloids under environmentally relevant conditions.

The dissociation of the initial soluble Np(IV) complex (*i.e.*  $[\text{Np(IV)(CO}_3)_5]^{6-}$ ) induces the intrinsic formation of nanocrystalline  $\text{NpO}_2$  in the solution phase. The resulting irregularly shaped nanocrystals with an average size of 4 nm exhibit a face-centered cubic (fcc), fluorite-type structure (space group  $Fm\bar{3}m$ ). The NCs tend to agglomerate under ambient conditions due to the weakly charged hydrodynamic surface at neutral pH (zeta potential  $\zeta \sim 0$  mV). The formation of micron-sized agglomerates, composed of nanocrystals of 2-5 nm in size, and the subsequent precipitation cause immobilization of the major amount of Np(IV) in the Np-carbonate system. Agglomeration of  $\text{NpO}_2$  nanocrystals in dependence on time was indicated by PCS and UV-vis absorption spectroscopy with the changes of baseline characteristics and absorption maximum at 742 nm.

Hitherto, unknown polynuclear species as intermediate species of  $\text{NpO}_2$  nanocrystal formation were isolated from solution and observed by HR-TEM. These polynuclear Np species appear as dimers, trimers and hexanuclear compounds in analogy with those reported for other actinides.

Intrinsic formation of  $\text{NpO}_2$  (fcc) nanocrystals under ambient environmental conditions is prevented by admixing silicic acid: amorphous Np(IV) silica colloids are formed when silicate is present in carbonate solution.

Herein, the initial molar ratio of Si to Np in solution lead to the formation of Np(IV) silica particles of different composition and size where Si content determines the structure and stability of resulting colloids. Implications for different electronic structures of Np(IV) in dependence on Si content in the solid phase are given by the shift of the absorption maximum at 742 nm characteristic for Np(IV) colloids, silica excess of 5 times the magnitude of Si to Np reveal a redshift up to 6 nm in the colloidal UV-vis spectrum. Precipitation of Np(IV) particles in the



ternary system results in a different coordination sphere of Np(IV) compared to the binary system, and the incorporation of Si into internal structure of Np(IV) silica colloids in coffinite-like structure is confirmed by EXAFS. TEM confirms different kinds of particle morphologies in dependence on the silica content. Silica-poor systems reveal porous particles in the micron-range which consist of irregular cross-linked hydrolyzed Np(IV) silica compartments with pores <15 nm. In contrast, long-term stabilized and silica-enriched systems are characterized by isolated particles with an average particle size of 45 nm. Agglomerates of such isolated Np(IV) silica particles appear as consolidated amorphous solids with a densely closed surface and exhibit no internal fractures. The latter mentioned morphology of Np(IV) silica particles might facilitate the migration behavior of Np(IV) in a stabilized colloidal form under environmental conditions. The silica-enriched particles with densely closed surface are long-term stabilized as colloidal dispersion (>1 year) due to repulsion effects caused by significant surface charge. Particles synthesized from Si/Np = 9/1 carry exclusively negative surface charge in nearly the whole pH range from pH 3 to pH 10 with  $\zeta = (-) 5$  to  $(-) 30$  mV. The zeta potentials of all particle systems containing silica are significantly shifted to more negative values below pH 7 where the isoelectrical point shifts from pH = 8.0 to 2.6 effecting negative charge under ambient conditions which supports electrostatic stabilization of Np(IV) particles. Particle surface charge at the slipping plane, particle size and shape necessarily depend on the initial magnitude of Si content in solution during particle formation. Particular changes of the morphology and internal structure of different Np(IV) silica colloids by aging are indicated by TEM and XPS. The composition and the crystallinity state of the initially formed amorphous phases partially changed into well-ordered nanocrystalline units characterized with fcc structure.

The presence of silicate under conditions expected in a nuclear waste repository significantly influences the solubility of Np(IV) and provoke the stabilization of waterborne Np(IV) up to concentrations of  $10^{-3}$  M, exceeding Np's solubility limit by a factor of up 10.000.

Neptunium and silicate significantly interact with each other, and thereby changing their individual hydrolysis and polymerization behavior. Silicate prevents the intrinsic formation of NpO<sub>2</sub> NCs in fcc-structure, and at the same time, Np(IV) prevents the polymerization of silicate. Both processes result in the formation of Np(IV) silica colloids which possibly influence the migration behavior and fate of Np in the waste repositories and surrounding environments. For tetravalent actinides in general, the most significant transport in the environment would occur by colloidal particles. Therefore, Np(IV) silica colloids could have a significant implication in the migration of Np, the important minor actinide in the waste repositories, via colloidal transport.

---

## 6 Experimental details

**Caution!**  $^{237}\text{Np}$  is a radioactive isotope and an  $\alpha$ -emitter. It should be handled in dedicated facilities with appropriate equipment for radioactive materials to avoid health risks caused by radiation exposure. Experiments were almost always performed in inert glove box.

### 6.1 Solutions

#### 6.1.1 Neptunium stock solutions

As Np stock an acidic solution of Np(V)  $5.6 \cdot 10^{-2}$  M in nitric acid 1M (Merck, p.a.) was provided by HZDR. Purified tetravalent Np was synthesized by potentiostatic electrolysis in nitric acid (c.f. section 6.2.1). Np(V) dissolved in nitric acid was electrochemically reduced on a platinum working electrode to Np(III) and afterward quantitatively oxidized to Np(IV) using methods previously reported.[65, 172, 173] UV-vis absorbance spectroscopy was applied to monitor the Np oxidation states during electrolysis. The purity of the tetravalent state of the Np ion was verified by the absorbance at 591 nm and the absence of shoulders at 551 nm of Np(III) and 617 nm of Np(V) (Figure 43).

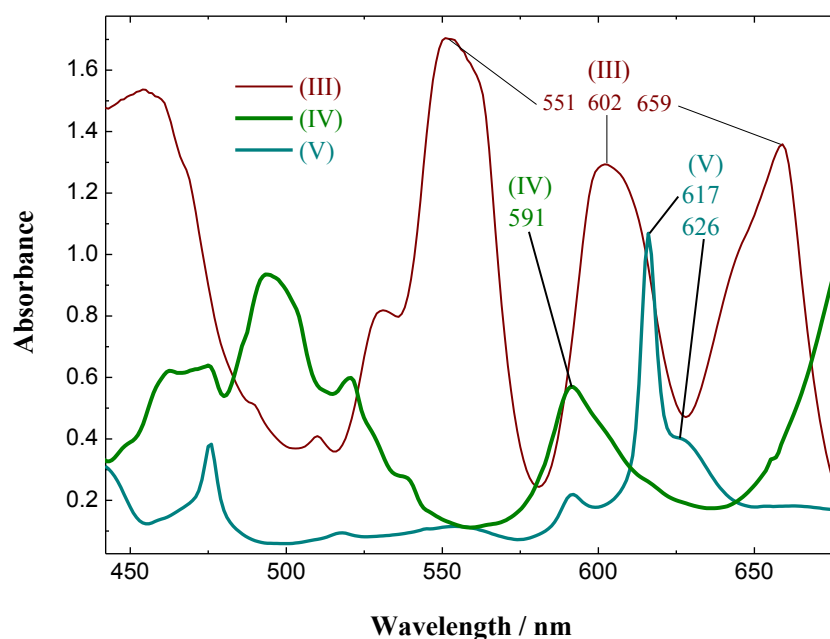


**Figure 43. Visible absorption spectra of Np in dependence on valency in acidic solution**

Visible absorption spectra of trivalent (red-brown), tetravalent (olive green) and pentavalent (emerald green) Np in acidic solution ( $[\text{Np}] = 5.6 \cdot 10^{-2}$  M in  $\text{HNO}_3$  1M). The spectra color reflects the actual color of the respective redox state of Np in solution; corresponding sample appearances are displayed in Appendix in Figure 53.

The acidic Np(IV) stock solution ( $[\text{Np}] = 5.6 \cdot 10^{-2} \text{ M}$  in  $\text{HNO}_3$  1.0 M) was diluted [174, 175] by adding it to a 1.0 M sodium bicarbonate solution (Merck, p.a.). The resulting solutions of Np(IV) carbonate complexes [26, 57-59, 176, 177] were filtered through 5-kDa (cut-off 1.5 nm) ultrafiltration devices (Vivaspin, Sartorius) to yield a particle/colloid-free solution of dissolved Np(IV) carbonate ( $[\text{Np}] = 9.8 \cdot 10^{-3} \text{ M}$  in  $\text{NaHCO}_3$  1.0 M). This alkaline Np solution was further used as the precursor solution for dilution experiments as a function of carbonate concentration and for Np(IV) nanoparticle synthesis. The purity of this alkaline precursor solution was verified by visible absorbance spectroscopy and EXAFS. The spectra of Np oxidation states III, IV and V in acidic solution were in excellent accordance with corresponding spectra published by other researchers.[156, 174, 178-182] From the spectra of the acidic Np(IV) solutions it can be deduced that a high purity of Np(IV) was reached by the two-step electrolysis (degree of purity min. 95%).

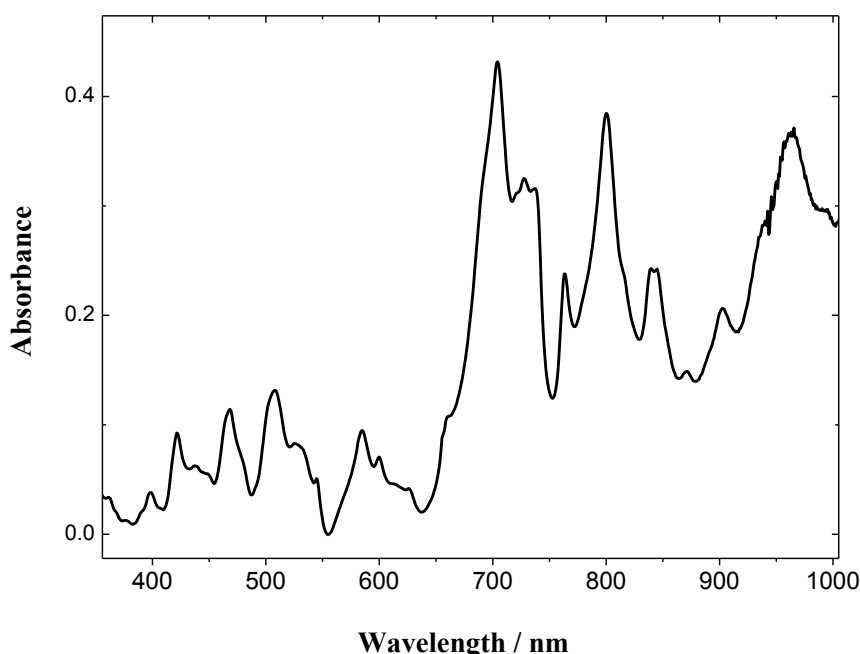


**Figure 44. Visible-NIR absorption spectra of tetravalent Np in slightly alkaline solution**

The spectrum was recorded from a particle-free solution after filtration through a 5-kDa membrane ( $[\text{Np}] = 9.8 \cdot 10^{-3} \text{ M}$  in  $\text{NaHCO}_3$  1M, pH = 9.0).

The characteristic spectrum of tetravalent Np carbonate complexes is shown in Figure 44. Corresponding absorbance properties are in very good accordance to reference data of Np(IV) carbonate complexes.[181, 182] The internal structure was investigated in more detail by EXAFS (cf. section 3.1). The missing of a peak of axial O atoms ( $\text{O}_{\text{ax}}$ ) at the Np ions at around  $R+\Delta=1.4 \text{ \AA}$  in the EXAFS results (Figure 10) provides further evidence that the pentavalent neptunium was absent and the Np was tetravalent.[26, 119, 153, 156] The complex structure of

the alkaline Np precursor was identified as Np(IV) pentacarbonate complex  $\text{Np}(\text{CO}_3)_5^{6-}$  in bidentate coordination mode.

### 6.1.2 Silicate stock solution

Silicic acid solutions were freshly prepared by the hydrolysis of tetramethyl orthosilicate (TMOS),  $\text{Si}(\text{OCH}_3)_4$  (Aldrich, 98% purity) by dilution in sodium bicarbonate (Merck, p.a.) solution. [49]

### 6.1.3 Np(IV) silicate samples

Evolution of Np(IV)-silica particles was initiated by the dilution of the Np(IV) stock solution (see section 6.1.1) in freshly hydrolysed solutions of silicic acid. Appropriate aliquots of the Np(IV) stock solution were mixed with dissolved silicic acid resulting in dispersions possessing concentrations of  $[\text{Np}] = 3.1 \cdot 10^{-4} \text{ M}$  or  $1.0 \cdot 10^{-3} \text{ M}$  and  $[\text{Si}] = 0.7\text{-}8.6 \cdot 10^{-3} \text{ M}$  with a background of 0.1 M or 1 M bicarbonate ( $\text{NaHCO}_3$ ).

#### 6.1.3.1 Np(IV) silica colloids above the MWSA

Neptunium (IV) carbonate solutions were mixed with silicic acid and respective amounts of  $\text{NaHCO}_3$  (0.1 or 1 M) to reach Np concentrations of around  $10^{-3} \text{ M}$  and Si concentrations of  $> 2 \cdot 10^{-3} \text{ M}$ . The latter concentration is also called the 'mononuclear wall' of silicic acid, i.e., it is the limit above which silicic acid solutions are expected to contain polymers. This is of relevance to the reaction with actinides because the affinity of metal ions to polysilicic acid is much higher than the affinity to monosilicic acid.[55, 56] The formation of a solid phase (Np(IV) nanoparticles) is induced by decreasing the complexant (the carbonate) concentration when mixing the solutions. In contrast to similar experiments with U(IV)[49] and Th(IV)[50], for Np(IV) at  $10^{-3} \text{ M}$ , it was observed that colloids formed immediately after mixing the solutions at slightly alkaline pH ( $\text{pH} > 8.5$ ).

#### 6.1.3.2 Np(IV) silica colloids below the MWSA

A silicic acid concentration above the MWSA is, though not impossible in nature, relatively far from typical environmental conditions. Therefore, experiments were conducted at silicic acid concentrations below the MWSA. In such solutions only traces of polysilicic acid can be present.[183] The Np(IV) concentration, too, was reduced in this case ( $3.1 \cdot 10^{-4} \text{ M}$ ). In these experiments, the Np(IV) silica colloids did not form immediately after mixing the reactants. The colloids formed after reducing the pH to  $< 8.5$  using 0.1 M  $\text{HNO}_3$ .

## 6.2 Chemical and physical characterization of solutions, colloidal solutions and isolated nanoparticles

### 6.2.1 Electrolysis setup - electrochemical preparation of Np solutions

A homemade electrolysis cell setup for purification of desired Np redox states in solution was designed and installed to perform electrochemical experiments under inert gas atmosphere. The principles of the homemade electrolysis cell setup are shown in Figure 45. The counter electrode (CE) and the counter electrolyte solution compartment define together the base of the electrochemical cell in comparison to standardized electrochemical setups. Containing the analytical solution (Np solution), the working electrode (WE) and the reference electrode (RE) the working side compartment is directly positioned in the voluminous counter electrolyte solution. The solutions are separated and communicate through a G5 diaphragm membrane. Platinum electrodes are positioned in each cell compartment. During electrolysis the actinide solution was stirred by nitrogen gas bubbling via an installed gas line. The Np(IV) stock solutions were synthesized by controlled potentiostatic two step electrolysis (potentiostat PS 6 (Meinsberg), with a counter and a Ag/AgCl reference electrode (ALS)) in nitric acid (Merck, p.a.) and dilution in sodium bicarbonate (Merck, p.a.) solution. A Np(V) stock solution in nitric acid was reduced to Np(III) (potential =  $-275$  mV, duration: 20 min) and further quantitatively oxidized to Np(IV) (potential =  $+100$  mV, duration: 30 min). UV-vis absorbance spectroscopy was applied to monitor the Np oxidation states during electrolysis and to verify the purity as well as the valence of Np in solutions. The as-prepared acidic Np(IV) stock solution ( $[\text{Np}] = 5.6 \cdot 10^{-2}$  M in  $\text{HNO}_3$  1 M) was further used to prepare Np(IV) bicarbonate solutions (cf. section 6.1.1.).

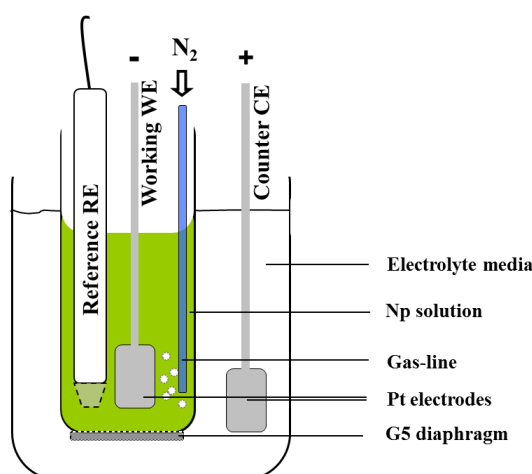


**Figure 45. Principle scheme of electrolysis cell setup**

Reference electrode (RE), working electrode (WE), and counter electrode (CE) in defined positions.

### 6.2.2 UV-vis spectroscopy

Spectra of Np stock solutions and of supernatant of dispersed or settled Np(IV) particle solutions were recorded in cuvettes with path length of 10 mm (Brandt) by a TIDAS 100 (J&M Analytik) connected with optical fiber in an anoxic glove box (nitrogen atmosphere,  $O_2 < 10$  ppm).

### 6.2.3 Photon correlation spectroscopy – particle size distribution in solution

Light scattering and Dynamic light scattering (or photon correlation spectroscopy) were performed at 25°C with standard setups, such as BI-90 (Brookhaven Instruments, U.S.A.) or Zetasizer Nano ZS (Malvern Instruments, U.K.) with disposable polystyrene cuvettes. An ALV CGS Goniometer was applied for long-term monitoring the SLI and PSD of Np silica colloids in round cuvettes in a toluene bath in dependence on angle of detection (30°, 90°, 150°, 173°).

A comprehensive description of the principles of PCS can be found in literature.[61, 63]

Recorded scattered light intensity fluctuations are calculated by autocorrelation function  $C(\tau)$ . The faster the  $C(\tau)$  decays to baseline, the faster (due to Brownian particle movement) and the smaller are the particles. For deriving the PSD from the obtained  $C(\tau)$ , the cumulant expansion and the CONTIN deconvolution were used. The latter calculates a PSD in dependence on the effective particles hydrodynamic sphere shape in solution (Stokes diameter).

### 6.2.4 Laser Doppler velocimetry – determination of particle surface charge at the shear plane

To characterize the colloidal stability of Np(IV) particle systems the surface charge of the particles is of particular interest. The charge of the actual surface of the particles is not directly accessible by *in-situ* methods due to irreversible adsorption of counter ions on the negatively charged surface of the dispersed particles in solution. The attraction of opposite charged ions on the surface of the particles and repulsion of similar charged ions leads to the formation of the diffused electrical double layer that consist of the charged surface, neutralizing counter ions and co-ions distributed in a diffuse manner.[132] An appropriate way to describe the magnitude of surface charge is to determine the potential of the electrical net charge at the shear plane / slipping plane in dependence on bulk fluid around the particles interface, which is defined as zeta potential ( $\zeta$ -potential) as shown in Figure 46.[132, 133] The  $\zeta$ -potential is the electrostatic potential at some distance away from the charged surface roughly equal to the thickness and potential of the Stern Layer.[132] The term particle surface charge used in the present thesis refers the effective hydrodynamic surface described by the zeta potential.

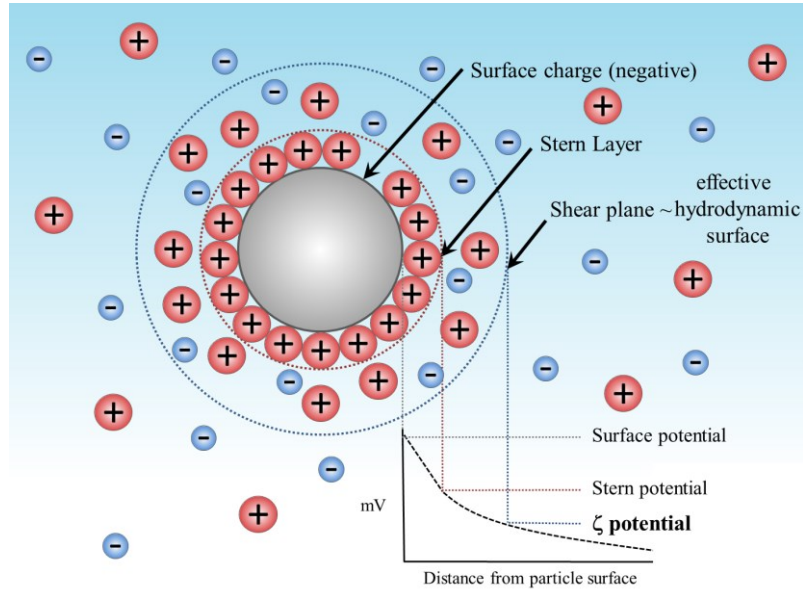


**Figure 46. The structure of colloid interface**

Distribution of electrical potential in the double-layer region surrounding a charged particle in solution (or a polar medium); ionic concentration and potential difference as a function of distance from the charged surface.

The zeta potential was determined using laser Doppler velocimetry by measuring the electrophoretic mobility.[19, 184] The electrophoretic mobility was converted to  $\zeta$ -potential using an algorithm based on the Smoluchowski theory. [133, 143-145] Measurements of Np(IV) nanoparticle dispersions were performed using a Zetasizer Nano ZS (Malvern Instruments, Malvern, U.K.) with disposable capillary cells. Four Np(IV) dispersions were prepared, as described in section 6.1.3, with different silica content and molar Si/Np composition. The pH of sample aliquots was adjusted with HNO<sub>3</sub> and NaOH in the range of 2.5-10.5 to determine the pH dependence of the zeta potential. Agglomerated and sedimented particles/colloids were re-suspended by weak ultrasonic treatment before measurement (treatment with 45 watt and 30 kHz in ca. 3 seconds, device UP50H, Hilscher, Germany) assuming that the colloid composition is homogeneous and re-dispersion does not change the original surface characteristics. The measurements were repeated tenfold at every pH value. The temperature was maintained at  $25.0 \pm 0.1$  °C.

The velocity is dependent on the strength of the electric field, dielectric constant of the fluid, viscosity of the fluid and the zeta potential. The electrophoretic mobility is described by the Henry equation (Equation ), where  $z$  is the zeta potential,  $U_E$  is the electrophoretic mobility,  $\epsilon$  is the dielectric constant,  $\eta$  is the viscosity and  $f(ka)$  is the Henry's function.

$$U_E = \frac{2\epsilon z f(ka)}{3\eta}$$

**Equation 1**

### 6.2.5 Transmission electron microscopy

Samples for TEM measurements were prepared by dropping defined volumes (1-3  $\mu\text{l}$ ) of dispersions containing Np(IV) particles onto a 400 mesh carbon-coated copper grid (400 mesh, S 160, Plano GmbH) and drying it under an inert atmosphere. The samples were kept anoxic until mounting them in a double tilt analytical sample holder and insertion into the column of the microscope ( $< 1$  min exposure to air). TEM micrographs and electronic properties were collected on an image-corrected Titan 80-300 microscope (FEI) operated at an accelerating voltage of 300 kV. Besides bright-field TEM imaging at medium magnification and high-resolution TEM at enhanced magnification (HR-TEM), selected area electron diffraction (SAED) was performed with the smallest available SAED aperture having a diameter of 10  $\mu\text{m}$  to study the microstructure of the nanoparticles formed. Employing a Li-drifted silicon detector (EDAX) in scanning TEM mode, energy-dispersive X-ray spectroscopy (EDXS) measurements were performed for qualitative chemical analysis.

### 6.2.6 X-ray absorption spectroscopy - neptunium valency and internal structure

During XAS, the intensity of the absorption coefficient  $\mu$  is measured as a function of energy of the X-ray photon  $E_x$ . Thereby, the focus is on energies just above absorption edges. Absorption edges appear in the spectrum when the X-ray energy is equal to the binding energy of the electron. The energies of the absorption edges are element specific tabulated values (e.g., neptunium  $L_{\text{III}}$ -edge at 17.1610 keV corresponding to an electron from the 2p ( $^2P_{3/2}$ ) orbital). The measurement of the X-ray fluorescence is favored in case of thick samples and low concentrations of the absorbing atom. It is detected in a right angle set-up to the incident beam.

The resulting X-ray absorption spectrum is divided in two parts: X-ray absorption near-edge structure (XANES) and extended X-ray absorption fine-structure (EXAFS) (Figure 47). XANES is strongly sensitive to formal oxidation state and coordination chemistry of the absorbing atom and is investigated typically within 30 eV of the main absorption edge and EXAFS. EXAFS spectroscopy was used to determine the distances, coordination number, and species of the neighbor atoms of the absorbing atom.[185]

Without prior separation procedures, *in-situ* metal valence determination using XANES spectroscopy is a powerful analytical tool in heterogeneous systems. In general, the ionization energy increases with increase of the valence state of the absorbing atom. Actinides ionization energies in the tetravalent and the pentavalent state are special cases. This is related to the different structures of the free Np(IV) ion with high charge density and the actinyl oxo structures of Np(V/VI) cations exhibiting different electronic configurations. So the sequence of ionization energies follows  $\text{Np(V)} < \text{Np(IV)} < \text{Np(VI)}$  from lower to higher energy.



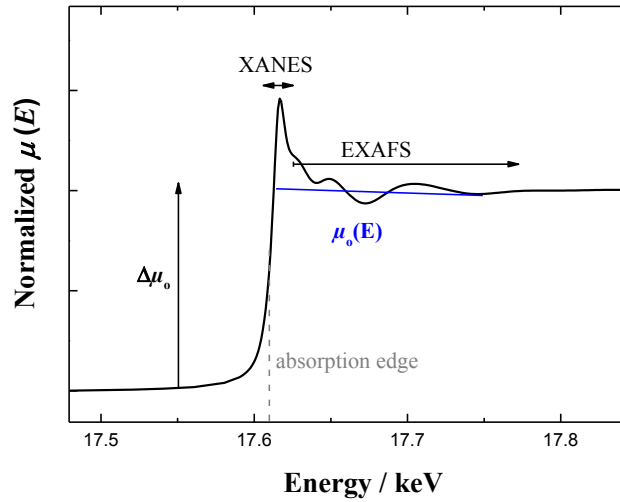


**Figure 47. X-ray absorption spectrum of Np(V)**

The neptunium absorption edge, the XANES and EXAFS regions, the edge-step  $\Delta\mu_0(E_0)$ , and the smooth background function  $\mu_0(E)$  are denoted ( $[\text{Np}] = 2.0 \cdot 10^{-2} \text{ M}$  in  $\text{HNO}_3$  1 M).

The EXAFS fine-structure function  $\chi(E)$  is defined in Equation as

$$\chi(E) = \frac{\mu(E) - \mu_0(E)}{\Delta\mu_0(E_0)}$$

**Equation 2**

where  $\mu_0(E)$  represents a smooth background function describing the absorption of an isolated atom without any interference with neighbor atoms and  $\Delta\mu_0$  is the jump of the absorption coefficient at the absorption edge with the threshold energy  $E_0$  (cf. Figure 47).

Due to the wave behavior of the emitted photo-electrons, the X-ray energy  $E$  is commonly expressed by the wave number of the photo-electron,  $k$ , as follows in Equation ,

$$k = \sqrt{\frac{2m(E - E_0)}{\hbar^2}}$$

**Equation 3**

where  $m$  means the electron mass and  $\hbar$  is the reduced Planck constant. The resulting oscillations as a function of wave number  $\chi(k)$  are very small, thus they are often  $k$ -weighted (multiplied with  $k^2$  or  $k^3$ ) to intensify them. The frequencies of the oscillations in  $\chi(k)$  can be attributed to the various coordination shells of the neighboring atoms and are expressed by the EXAFS equation (Equation 4):

$$\chi(k) = \sum_j \frac{N_j S_0^2(k) f_j(k) e^{-2k^2 \sigma_j^2}}{k R_j^2} \sin[2kR_j + \delta_j(k)]$$

**Equation 4**

thereby  $S_0^2$  represents the amplitude reduction factor,  $f(k)$  is the backscattering amplitude, and  $\delta(k)$  describes the total phase-shift.  $f(k)$  and  $\delta(k)$  have to be known to determine the number of neighbor atoms,  $N$ , the distance to the neighboring atom,  $R$ , and the disorder in the neighbor distance,  $\sigma^2$ , also known as Debye-Waller factor. Furthermore, EXAFS gives information about the atomic species of the neighboring atom, since  $f(k)$  and  $\delta(k)$  are a function of its atomic number. By Fourier transformation of the  $\chi(k)$  function into  $R$ -space the different coordination shells around the absorbing atom can be visualized.

XAS measurements were carried out at the Rossendorf Beamline of the European Synchrotron Radiation Facility.[186] The beamline is equipped with a water-cooled Si(111) double-crystal monochromator. Beam collimation and suppression of higher-order harmonics is achieved with two Pt-coated mirrors. The spectra were collected in fluorescence mode. The incoming intensity ( $I_0$ ) was registered with an ionization chamber filled with 20% argon and 80% nitrogen.

The aqueous dispersed Np(IV) silica colloid sample, the aqueous Np(IV) bicarbonate stock solution and the aqueous Np(V) reference solution in nitric acid were measured under ambient conditions, the wet precipitate of NpO<sub>2</sub> NCs sample and the NpO<sub>2</sub> reference powder were measured in a closed-cycle He cryostat at 15 K. Energy calibration of the EXAFS spectra was performed by measurement of the K-edge of a Y metal foil (first inflection point is defined at 17038 eV). Multi electron excitation effects [187, 188] were considered during data extraction. The EXAFS oscillations were extracted from the raw absorption spectra by standard methods including a  $\mu_0$  spline approximation for the atomic background using WinXAS software.[189] The EXAFS data was fitted with EXAFSPAK [190] using theoretical phase and amplitude functions calculated with the FEFF 8.20 code.[191] Phase and amplitude functions were calculated by using the crystal structure data of NpO<sub>2</sub> [79] and USiO<sub>4</sub> [192] where U was replaced by Np. A reference compound of NpO<sub>2</sub> powder was provided from CEA Cadarache. The lattice parameter obtained for this NpO<sub>2</sub> ( $Fm\bar{3}m$ , 5.434(1) Å) in agreement with the reported value for NpO<sub>2</sub>. [193] The amplitude reduction factor,  $S_0^2$ , was defined as 0.9 in the data fits. The Np threshold energy,  $E_{k=0}$ , was defined at 17625 eV and varied as a global fit parameter resulting in the energy shift  $\Delta E_{k=0}$ . The overall goodness of the fits,  $F$ , is given by  $\chi^2$  weighted by the magnitude of data. For EXAFS sample preparation also see Table 12.

**Table 12. XAS samples. Details of sample preparation for the XAS experiments**

Sample	Type of sample	Preparation
Np(IV) (aq) in 1 M NaHCO <sub>3</sub>	Aqueous Np(IV) solution stabilized as pentacarbonate complexes	Stock solution of $5.6 \cdot 10^{-2}$ M Np(IV) in 1 M HNO <sub>3</sub> was diluted with 1 M NaHCO <sub>3</sub> to $10.0 \cdot 10^{-3}$ M Np
Wet precipitate of diluted sample	Wet paste of NpO <sub>2</sub> NCs precipitated from alkaline region by dilution	Stock solution of $9.8 \cdot 10^{-2}$ M Np(IV) in 1 M NaHCO <sub>3</sub> was diluted with pure water to $1.0 \cdot 10^{-3}$ M Np, a precipitate forms at origin pH $\sim 7.5$
NpO <sub>2</sub> reference material	Reference powder of NpO <sub>2</sub>	Already prepared sample filled with reference NpO <sub>2</sub> powder, sealed and provided by CEA, Cadarache
Np(IV) silica colloids	Dispersion of stable Np(IV)-silica colloids (molar Si/Np ratio 1.3)	Stock solution of $5.6 \cdot 10^{-2}$ M Np(IV) in 1 M HNO <sub>3</sub> was diluted with 1 M NaHCO <sub>3</sub> to $10.0 \cdot 10^{-3}$ M Np, Np(IV)-silica colloids form after dilution to $1.0 \cdot 10^{-3}$ M Np with $3.0 \cdot 10^{-3}$ M Si (pH 8.5 – 9.0)
Np(V) (aq) in 1 M HNO <sub>3</sub>	Aqueous Np(V) in acidic solution	Stock solution of $5.6 \cdot 10^{-2}$ M Np(IV) in 1 M HNO <sub>3</sub> was diluted with 1 M HNO <sub>3</sub> to $2.0 \cdot 10^{-2}$ M Np

For a comprehensive introduction into XAS (XANES and EXAFS) in more detail the reader is referred to several book sections[185, 194-196].

### 6.2.7 X-ray photoelectron spectroscopy – binding energies of Np and oxygen core levels

XPS was measured in the 0-1200 eV binding energy range from NpO<sub>2</sub> NCs and longterm stabilized Np(IV) silica colloids. A dispersion of cleaned NCs were deposited drop-wise on HOGP (highly ordered pyrolytic graphite) coated sample holder and dried under nitrogen atmosphere. The spectra were recorded with a Microlab 310 F (FISONS/ThermoFischer) using monochromatized Mg K<sub>α</sub> radiation ( $h\nu = 1253.6$  eV) under  $10^{-7}$  Pa at room temperature. The binding energies were indicated relative to the binding energy of C 1s electrons (285.0 eV) originated from the HOPG sample holders surface and specified with NIST-Database[197] after performing baseline correction in accordance to Shirley et al..[198]

### 6.2.8 Element analysis

The Np and Si concentrations in solution and in the solid-state were determined by inductively coupled plasma-mass spectroscopy. Np concentrations were additionally assayed by liquid scintillation counting. For LSC measurements a TriCarb 3100 TR from Perkin Elmer was applied. A liquid scintillation cocktail was used (Ultima Gold™), containing diisopropylnaphthalene as solute, 2,5-diphenyloxazole as primary scintillator, and 1,4-bis(5-phenyl-2-oxazolyl)benzene as secondary scintillator. For each measurement, a small aliquot of the respective liquid sample solution was added to the scintillation cocktail and a homogeneous mixture was prepared. The composition of Np solutions and dispersions was determined by ICP-MS (mod. ELAN 9000, Perkin Elmer, Boston, U.S.A., error 10 %) in combination with ultrafiltration (UF) and ultracentrifugation (UC) techniques. Particle compositions concerning [Np] and [Si] were derived from the solution concentrations before and after applying UF or UC. In accordance to reference [49], UF was performed with disposable filtration units (Microsep, Pall Corp.) with a molecular cut-off of 5-kDa. The filtrations were carried out by centrifugation at 3500g in a glove box under inert gas. For separation with UC, aliquots of samples were centrifuged at an acceleration of 100,000g for 5 h in an Optima XL 100K type centrifuge (Beckman Coulter, U.S.A.). Well-defined volumes of the centrifugate (the upper 50% of the supernatant volume) were carefully removed from the centrifugal tubes via a pipette under inert gas in a glove box and those supernatants were further investigated and characterized.

### 6.2.9 Determination pH and $E_h$

The pH values were measured using a laboratory pH meter (mod. Inolab pH 720, WTW, Weilheim, Germany) with Blue line electrodes (Schott, Mainz, Germany), calibrated using standard buffers (WTW) at pH 4, 7, and 9, equilibrated at 25 °C. If necessary, the pH values were adjusted using HNO<sub>3</sub> and NaOH solutions (Merck, p.a.). The potential (in millivolts) of the samples was recorded relative to the standard half-cell potential of reference electrodes Blue electrode (Orion™ 96-78 combination electrode or ALV Ag/AgCl electrode in 3 M KCl; Meinsberg potentiostat) and corrected relative to the standard hydrogen electrode according to Langmuir. [199] There, the emf or  $E_{\text{measured}}$  is the electromotive force or potential (in millivolts) of the water measured at the sample temperature and  $E_{\text{ref}}$  is the reference electrode potential.

$$E_h = emf + E_{ref}$$

Equation 5

---

## Appendix

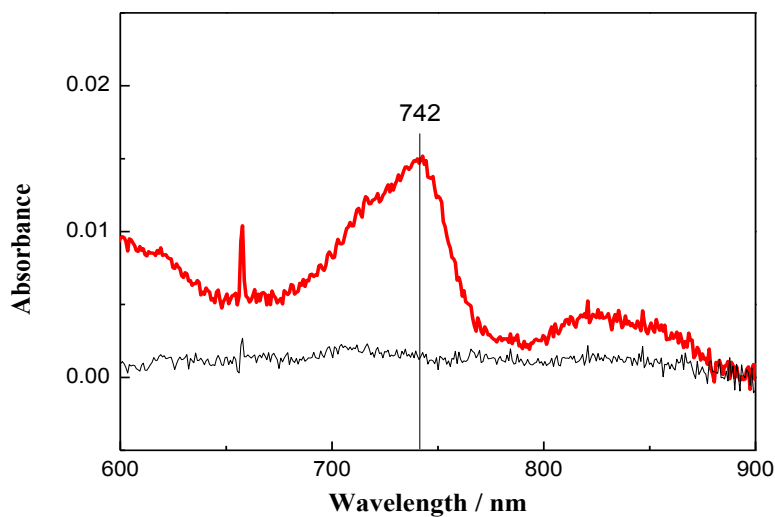


**Figure 48. Visible absorption spectra of a Np(IV) silica sample before and after ultrafiltration**

([Np] =  $3.1 \cdot 10^{-4}$  M, [Si] =  $1.53 \cdot 10^{-3}$  M and  $1 \cdot 10^{-4}$  M  $\text{HCO}_3^-$ ; Sample 4 of Table 1) before (red spectrum) and after (black spectrum) ultrafiltration through a 5-kDa membrane.

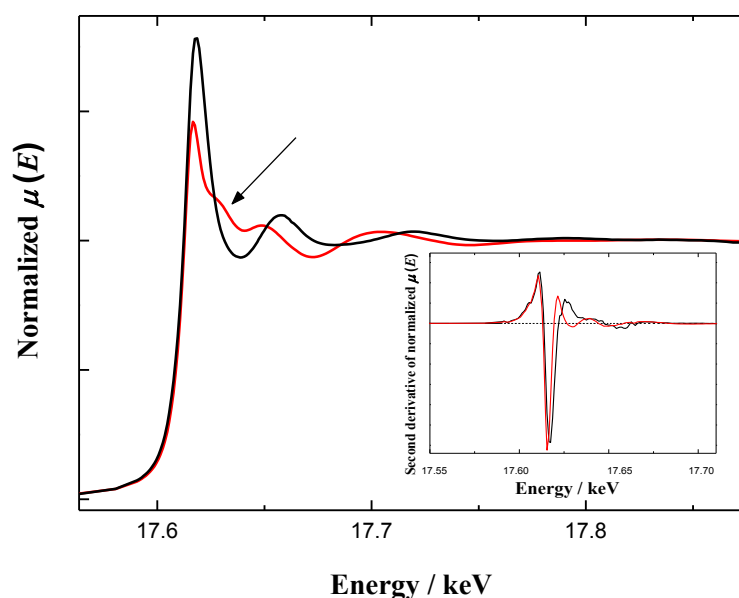


**Figure 49. Normalized Np  $L_{III}$ -edge XANES spectra of Np(IV) silica nanoparticle solution and Np(V) reference**

$[(\text{Np},\text{Si})\text{O}_n(\text{OH})_{4-n} \cdot x\text{H}_2\text{O}]^{4-2n-(4-n)}$  precipitated in 0.1 M  $\text{NaHCO}_3$  (black) and reference Np(V) solution with [Np] =  $2.0 \cdot 10^{-2}$  M in 1 M  $\text{HNO}_3$  (red) and their corresponding second derivatives (inset).

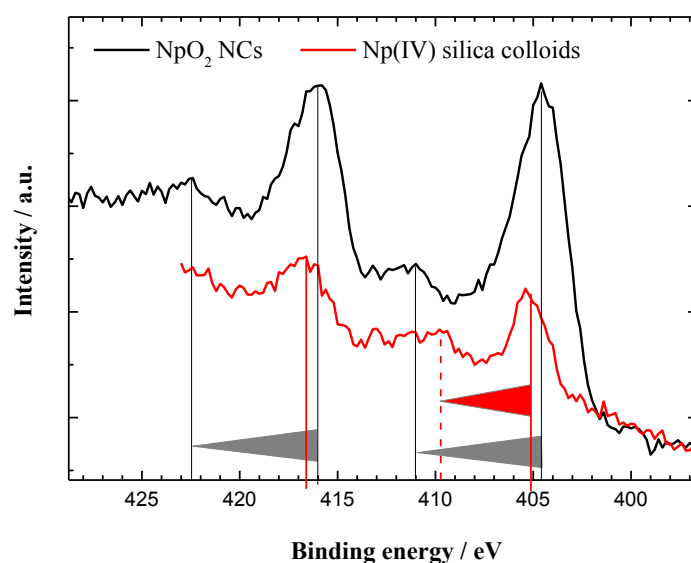


**Figure 50. XPS Np 4f core level spectra of NpO<sub>2</sub> NCs and stabilized Np(IV) silica colloids**  
Corresponding shake-up satellites are highlighted by a shift of energies corresponding to 4f core level split (resolution BE = 0.2 eV).

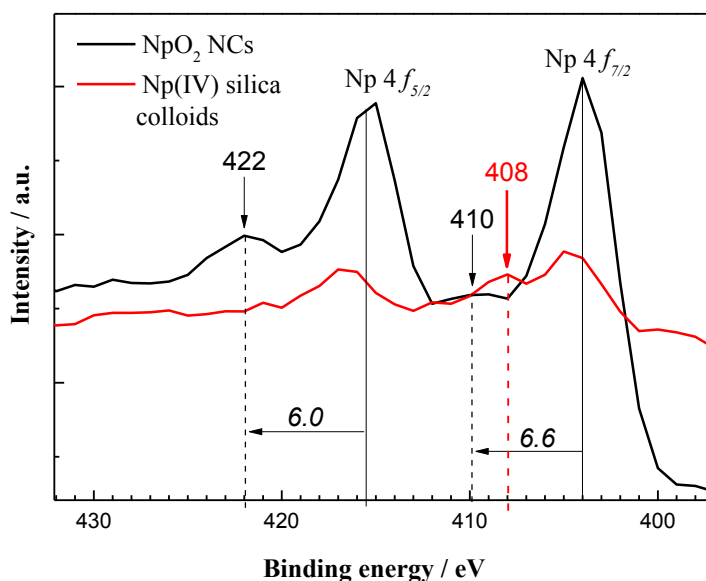


**Figure 51. XPS Np 4f core level spectra of NpO<sub>2</sub> NCs and stabilized Np(IV) silica colloids**  
Displayed spectra are details of survey XPS records (Figure 14 and Figure 32; resolution BE = 1 eV).  
Note, that survey XPS spectra are recorded with a resolution in BE = 1 eV. The Np 4f<sub>5/2</sub> and Np 4f<sub>7/2</sub> level satellites are observed in the survey spectrum at higher BE, too (approximately with  $\Delta E_{sat} \sim 6$  eV for Np 4f<sub>5/2</sub> satellite and with  $\Delta E_{sat} \sim 7$  eV for Np 4f<sub>7/2</sub> satellite). Both distances fit well (within an error  $\pm 1$  eV in BE) in indicating shake-up satellites as turning points and therefore internal fluorite structure.

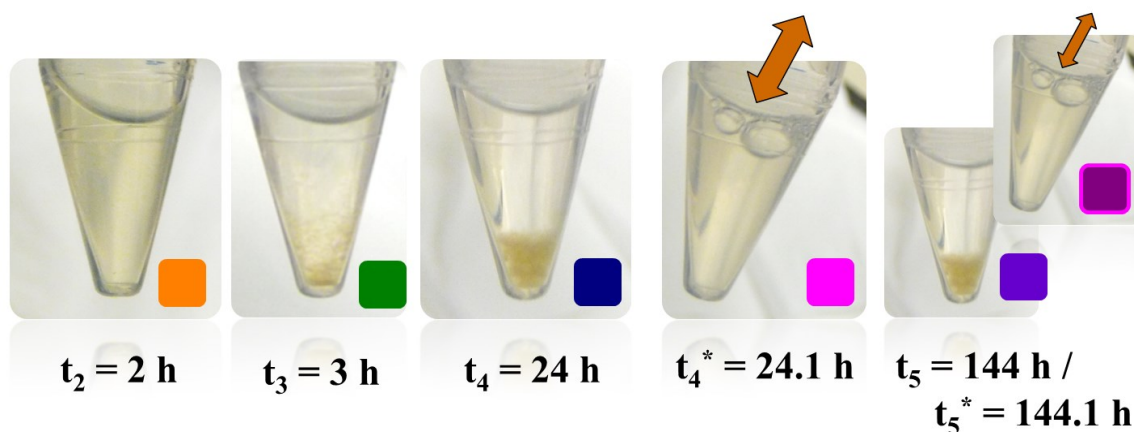


**Figure 52. Appearance of Np(IV) sample in dependence on time after initial hydrolysis**  
 $[\text{Np}] = 1 \cdot 10^{-3} \text{ M}$  in  $0.1 \text{ M HCO}_3^-$ ;  $t_4^*/t_5^*$ : sample appearance after re-dispersion.  
 Colors correlate with the PSD of  $\text{NpO}_2$  NC agglomerates in **Figure 17**.

## Neptunium redox states

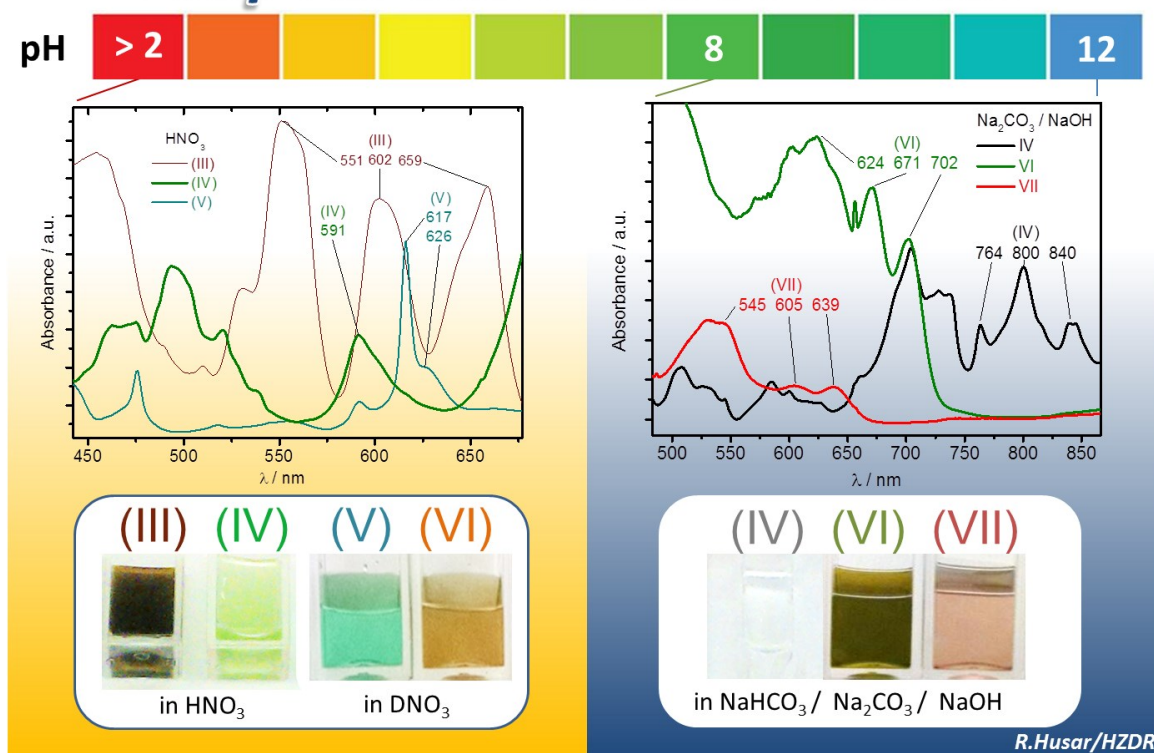


**Figure 53. UV-vis spectra of Np redox states and corresponding sample appearance in dependence on sample composition and pH.**

---

## References

1. Kim, J.I., *Significance of actinide chemistry for the long-term safety of waste disposal*. Nuclear Engineering and Technology, 2006. **38**(6): p. 459-482.
2. DOE, *Yucca Mountain Science and Engineering Report DOE/RW-0539-1*. 2002, U.S. Department of Energy: North Las Vegas, Nevada, U.S.A.
3. Dozol, M. and R. Hagemann, *Radionuclide migration in groundwaters: review of the behaviour of actinides*. Pure and Applied Chemistry, 1993. **65**(5): p. 1081-1102.
4. Thakur, P. and G.P. Mulholland, *Determination of Np-237 in environmental and nuclear samples: A review of the analytical method*. Applied Radiation and Isotopes, 2012. **70**(8): p. 1747-1778.
5. Zhao, P., et al., *Analysis of trace neptunium in the vicinity of underground nuclear tests at the Nevada National Security Site*. Journal of Environmental Radioactivity, 2014. **137**: p. 163-172.
6. IAEA, *Status of Minor Actinide Fuel Development*. IAEA Nuclear Energy Series NF-T-4.6. 2009, Vienna, Austria: International Atomic Energy Agency - IAEA.
7. IAEA, *Nuclear Fuel Cycle Simulation System (VISTA)*. Vol. IAEA-TECDOC-1535. 2007, Vienna, Austria: International Atomic Energy Agency - IAEA. 95.
8. OECD/NEA, *Physics and safety of transmutation systems - A status report*. 2006, NEA: Paris.
9. Assinder, D.J., *A review of the occurrence and behaviour of neptunium in the Irish Sea*. Journal of Environmental Radioactivity, 1999. **44**(2-3): p. 335-347.
10. Lindahl, P., et al., *Studies of Np and Pu in the marine environment of Swedish-Danish waters and the North Atlantic Ocean*. Journal of Environmental Radioactivity, 2005. **82**(3): p. 285-301.
11. Novikov, A.P., et al., *Evolution of actinide partitioning with colloidal matter collected at PA "Mayak" site as studied by sequential extraction*. Journal of Radioanalytical and Nuclear Chemistry, 2009. **280**(3): p. 629-634.
12. Novikov, A.P., et al., *Concentration of neptunium from the ground waters of the Karachai Lake contamination area*. Journal of Radioanalytical and Nuclear Chemistry, 2011. **289**(2): p. 431-436.
13. Fitts, C.R., *Groundwater Science*, in *Groundwater Science (Second Edition)*, C.R. Fitts, Editor. 2013, Academic Press: Boston. p. 1-677.
14. Kim, B.Y., et al., *Effect of carbonate on the solubility of neptunium in natural granitic groundwater*. Nuclear Engineering and Technology, 2010. **42**(5): p. 552-561.
15. Kim, S.S., M.H. Baik, and K.C. Kang, *Solubility of neptunium oxide in the KURT (KAERI underground research tunnel) groundwater*. Journal of Radioanalytical and Nuclear Chemistry, 2009. **280**(3): p. 577-583.
16. DeNovio, N.M., J.E. Saiers, and J.N. Ryan, *Colloid movement in unsaturated porous media: Recent advances and future directions*. Vadose Zone Journal, 2004. **3**(2): p. 338-351.
17. Robinson, B.A., C.H. Li, and C.K. Ho, *Performance assessment model development and analysis of radionuclide transport in the unsaturated zone, Yucca Mountain, Nevada*. Journal of Contaminant Hydrology, 2003. **62-3**: p. 249-268.
18. Choppin, G.R., *Actinide speciation in the environment*. Journal of Radioanalytical and Nuclear Chemistry, 2007. **273**(3): p. 695-703.
19. Maher, K., J.R. Bargar, and G.E. Brown, *Environmental Speciation of Actinides*. Inorganic Chemistry, 2013. **52**(7): p. 3510-3532.
20. Guillaumont, R., et al., *Update on the chemical thermodynamics of uranium, neptunium, plutonium, americium and technetium*. . Chemical Thermodynamics Vol. 5. Vol. 5. 2003, Elsevier: OECD Nuclear Energy Agency. 960.



21. Neck, V. and J.I. Kim, *Solubility and hydrolysis of tetravalent actinides*. Radiochimica Acta, 2001. **89**(1): p. 1-16.
22. Neck, V., et al., *Solubility of amorphous Th(IV) hydroxide - application of LIBD to determine the solubility product and EXAFS for aqueous speciation*. Radiochimica Acta, 2002. **90**(9-11): p. 485-494.
23. Rai, D., J.L. Swanson, and J.L. Ryan, *Solubility of NpO<sub>2</sub>.CHI-H<sub>2</sub>O(am) in the presence of Cu(I)/Cu(II) redox buffer*. Radiochimica Acta, 1987. **42**(1): p. 35-41.
24. Ryan, J.L. and D. Rai, *The solubility of uranium(IV) hydrous oxide in sodium-hydroxide solutions under reducing conditions*. Polyhedron, 1983. **2**(9): p. 947-952.
25. Opel, K., et al., *Study of the solubility of amorphous and crystalline uranium dioxide by combined spectroscopic methods*. Radiochimica Acta, 2007. **95**(3): p. 143-149.
26. Rai, D., et al., *A thermodynamic model for the solubility of NpO<sub>2</sub>(am) in the aqueous K<sup>+</sup>-HCO<sub>3</sub><sup>-</sup>-CO<sub>3</sub><sup>2-</sup>-OH<sup>-</sup>-H<sub>2</sub>O system*. Radiochimica Acta, 1999. **84**(3): p. 159-169.
27. Rai, D., A.R. Felmy, and J.L. Ryan, *Uranium hydrolysis constants and solubility product of UO<sub>2</sub>.XH<sub>2</sub>O(am)*. Inorganic Chemistry, 1990. **29**(2): p. 260-264.
28. Buddemeier, R.W. and J.R. Hunt, *Transport of colloidal contaminants in groundwater: Radionuclide migration at the Nevada test site*. Applied Geochemistry, 1988. **3**(5): p. 535-548.
29. Kersting, A.B., et al., *Migration of plutonium in ground water at the Nevada Test Site*. Nature, 1999. **397**(6714): p. 56-59.
30. Novikov, A.P., et al., *Colloid transport of plutonium in the far-field of the Mayak Production Association, Russia*. Science, 2006. **314**(5799): p. 638-641.
31. Kersting, A.B., *Plutonium Transport in the Environment*. Inorganic Chemistry, 2013. **52**(7): p. 3533-3546.
32. Kim, J.I., *Actinide colloids in natural aquifer systems*. MRS Bulletin, 1994. **19**(12): p. 47-53.
33. Powell, B.A., et al., *Stabilization of Plutonium Nano-Colloids by Epitaxial Distortion on Mineral Surfaces*. Environmental Science & Technology, 2011. **45**(7): p. 2698-2703.
34. Ryan, J.N. and M. Elimelech, *Colloid mobilization and transport in groundwater*. Colloids and Surfaces a-Physicochemical and Engineering Aspects, 1996. **107**: p. 1-56.
35. Walther, C. and M.A. Denecke, *Actinide Colloids and Particles of Environmental Concern*. Chemical Reviews, 2013. **113**(2): p. 995-1015.
36. Clark, D.L., D.E. Hobart, and M.P. Neu, *Actinide carbonate complexes and their importance in actinide environmental chemistry*. Chemical Reviews, 1995. **95**(1): p. 25-48.
37. Altmaier, M., X. Gaona, and T. Fanghanel, *Recent Advances in Aqueous Actinide Chemistry and Thermodynamics*. Chemical Reviews, 2013. **113**(2): p. 901-943.
38. Kaszuba, J.P. and W.H. Runde, *The aqueous geochemistry of neptunium: Dynamic control of soluble concentrations with applications to nuclear waste disposal*. Environmental Science & Technology, 1999. **33**(24): p. 4427-4433.
39. Knope, K.E. and L. Soderholm, *Solution and Solid-State Structural Chemistry of Actinide Hydrates and Their Hydrolysis and Condensation Products*. Chemical Reviews, 2013. **113**(2): p. 944-994.
40. Wilson, R.E., et al., *Structures of dimeric hydrolysis products of thorium*. Inorganic Chemistry, 2007. **46**(7): p. 2368-2372.
41. Takao, K., et al., *Formation of Soluble Hexanuclear Neptunium(IV) Nanoclusters in Aqueous Solution: Growth Termination of Actinide(IV) Hydrous Oxides by Carboxylates*. Inorganic Chemistry, 2012. **51**(3): p. 1336-1344.
42. Soderholm, L., et al., *The structure of the plutonium oxide nanocluster [Pu<sub>38</sub>O<sub>56</sub>Cl<sub>15</sub>(H<sub>2</sub>O)<sub>8</sub>]/14*. Angewandte Chemie - International Edition, 2008. **47**(2): p. 298-302.
43. Abdel-Fattah, A.I., et al., *Dispersion Stability and Electrokinetic Properties of Intrinsic Plutonium Colloids: Implications for Subsurface Transport*. Environmental Science & Technology, 2013. **47**(11): p. 5626-5634.

44. Artinger, R., et al., *Humic colloid-borne Np migration: Influence of the oxidation state*. Radiochimica Acta, 2000. **88**(9-11): p. 609-612.
45. Friese, J.I., et al., *Report PNNL 14307*. 2003, Pacific Northwest Laboratory: Richland, Washington, U.S.A.
46. Mori, A., et al., *The colloid and radionuclide retardation experiment at the Grimsel Test Site: influence of bentonite colloids on radionuclide migration in a fractured rock*. Colloids and Surfaces a-Physicochemical and Engineering Aspects, 2003. **217**(1-3): p. 33-47.
47. Kalmykov, S.N. and M.A. Denecke, *Actinide Nanoparticle Research*. Heidelberg Dordrecht London New York: Springer.
48. Siever, R., *Silicon-abundance in natural waters*, in *Handbook of Chemistry*, K.H. Wedepohl, Editor., Springer.
49. Dreissig, I., et al., *Formation of uranium(IV)-silica colloids at near-neutral pH*. Geochimica Et Cosmochimica Acta, 2011. **75**(2): p. 352-367.
50. Hennig, C., et al., *Solid-state properties and colloidal stability of thorium(IV)-silica nanoparticles*. Geochimica Et Cosmochimica Acta, 2013. **103**: p. 197-212.
51. Degueldre, C., et al., *Colloid properties in granitic groundwater systems. II: Stability and transport study*. Applied Geochemistry, 1996. **11**(5): p. 697-710.
52. Degueldre, C., et al., *Groundwater colloid properties: A global approach*. Applied Geochemistry, 2000. **15**(7): p. 1043-1051.
53. Elimelech, M. and C.R. Omelia, *Kinetics of deposition of colloidal particles in porous media*. Environmental Science & Technology, 1990. **24**(10): p. 1528-1536.
54. McDowell-Boyer, L.M., *Chemical mobilization of micron-sized particles in saturated porous media under steady flow conditions*. Environmental Science and Technology, 1992. **26**(3): p. 586-593.
55. Iler, R.K., *The Chemistry of Silica*. 1979, New York: John Wiley & Sons.
56. Taylor, P.D., R. Jugdaohsingh, and J.J. Powell, *Soluble silica with high affinity for aluminum under physiological and natural conditions*. Journal of the American Chemical Society, 1997. **119**(38): p. 8852-8856.
57. Kitamura, A. and Y. Kohara, *Solubility of Neptunium(IV) in Carbonate Media*. Journal of Nuclear Science and Technology, 2002. **39**(sup3): p. 294-297.
58. Kitamura, A. and Y. Kohara, *Carbonate complexation of neptunium(IV) in highly basic solutions*. Radiochimica Acta, 2004. **92**(9-11): p. 583-588.
59. Moriyama, H., M.I. Pratopo, and K. Higashi, *The solubility and colloidal behavior of neptunium(IV)*. Science of the Total Environment, 1989. **83**(3): p. 227-237.
60. Zeh, P., et al., *The reduction of Np(V) in groundwater rich in humic substances*. Radiochimica Acta, 1999. **87**(1-2): p. 23-28.
61. Ford, N.C., *Light Scattering Apparatus*. Dynamic Light Scattering: Application of PCS, ed. R. Pecora. 1985, New York, U.S.A.: Plenum Press.
62. Schurtenberger, P. and M.E. Newman, *Characterization of Biological and Environmental Particles using Static and Dynamic Light Scattering*, in *Environmental Particles*, J. Buffle and H.P. van Leeuwen, Editors. 1993, CRC Press: Boca Raton. p. 37-115.
63. Tscharnuter, W., *Photon Correlation Spectroscopy in Particle Sizing*, in *Encyclopedia of Analytical Chemistry*, R.A. Meyers, Editor. 2000, John Wiley & Sons: Chichester., p. 5469-5485.
64. Provencher, S.W., *CONTIN - A general purpose constrained regularization program for inverting noisy algebraic and integral-equations*. Computer Physics Communications, 1982(27): p. 229-242.
65. Neck, V., et al., *A spectroscopic study of the hydrolysis, colloid formation and solubility of Np(IV)*. Radiochimica Acta, 2001. **89**(7): p. 439-446.
66. Bohren, C.F. and D.R. Huffman, *Absorption and scattering of light by small particles*. 1998, Weinheim, Germany: Wiley-VCH Verlag GmbH Co KG.
67. Hennig, C., et al., *Comparative investigation of the solution species  $[U(CO_3)_5]^{6-}$  and the crystal structure of  $Na_6[U(CO_3)_5] \cdot 12H_2O$* . Dalton Trans., 2010. **39**(15): p. 3744-3750.

- 
68. Clark, D.L., et al., *Identification of the limiting species in the plutonium(IV) carbonate system. Solid state and solution molecular structure of the [Pu(CO<sub>3</sub>)<sub>5</sub>]<sup>6-</sup> ion.* Inorg. Chem., 1998. **37**(12): p. 2893-2899.
69. Hennig, C., et al., *Comparative investigation of the solution species U(CO<sub>3</sub>)<sub>5</sub> (6-) and the crystal structure of Na-6 U(CO<sub>3</sub>)<sub>5</sub> center dot 12H(2)O.* Dalton Transactions, 2010. **39**(15): p. 3744-3750.
70. Rai, D., et al., *A thermodynamic model for the solubility of PuO<sub>2</sub>(am) in the aqueous K+HCO<sub>3</sub>--CO<sub>3</sub><sup>2-</sup>--OH--H<sub>2</sub>O system.* Radiochimica Acta, 1999. **86**(3-4): p. 89-99.
71. Schofield, E.J., et al., *Structure of biogenic uraninite produced by Shewanella oneidensis strain MR-1.* Environ. Sci. Technol., 2008. **42**(21): p. 7898-7904.
72. Rothe, J., et al., *XAFS investigation of the structure of aqueous thorium(IV) species, colloids, and solid thorium(IV) oxide/hydroxide.* Inorg. Chem., 2002. **41**(2): p. 249-258.
73. Rothe, J., et al., *XAFS and LIBD investigation of the formation and structure of colloidal Pu(IV) hydrolysis products.* Inorg. Chem., 2004. **43**(15): p. 4708-4718.
74. Ikeda-Ohno, A., et al., *Speciation and structural study of U(IV) and -(VI) in perchloric and nitric acid solutions.* Inorg. Chem., 2009. **48**(15): p. 7201-7210.
75. Guillaumont, R., et al., *Update on the chemical thermodynamics of uranium, neptunium, plutonium, americium and technetium.* Chemical Thermodynamics, ed. F.J. Mompean, et al. Vol. 5. 2003, Amsterdam, The Netherlands: Elsevier B.V.
76. Rand, M., et al., *Chemical Thermodynamics of Thorium.* Chemical Thermodynamics, ed. F.J. Mompean, J. Perrone, and M. Illemassène. Vol. 11. 2007, OECD-NEA: OECD-NEA.
77. Dahou, S., et al., *Short note on the hydrolysis and complexation of neptunium(IV) in HEPES solution.* Radiochimica Acta, 2013. **101**(6): p. 367-372.
78. Ekberg, C., et al., *The structure of plutonium(IV) oxide as hydrolysed clusters in aqueous suspensions.* Dalton Transactions, 2013. **42**(6): p. 2035-2040.
79. Taylor, D., *Binary oxides with the fluorite and rutile structures and the antiferroite structures.* Transactions and Journal of the British Ceramic Society, 1984. **83**(2): p. 32-37.
80. Porter, J.A., *Production of neptunium dioxide.* Ind. Eng. Chem. Process Des. Dev., 1964. **3**(4): p. 289-292.
81. Naegele, J.R., *Photoemission spectroscopy of actinide intermetallics.* Physica B & C, 1985. **130**(1-3): p. 52-55.
82. Naegele, J.R., L.E. Cox, and J.W. Ward, *Photoelectron spectroscopy (UPS/XPS) study of Np<sub>2</sub>O<sub>3</sub> formation on the surface of neptunium metal.* Inorganica Chimica Acta, 1987. **139**(1-2): p. 327-329.
83. Seibert, A., T. Gouder, and F. Huber, *Reaction of neptunium with molecular and atomic oxygen: Formation and stability of surface oxides.* Journal of Nuclear Materials, 2009. **389**(3): p. 470-478.
84. Teterin, Y., et al., *X-ray photoelectron spectra structure and chemical bond nature in NpO<sub>2</sub>.* Physical Review B - Condensed Matter and Materials Physics, 2014. **89**(3).
85. Veal, B.W., et al., *X-ray photoelectron-spectroscopy study of oxides of the transuranium elements Np, Pu, Am, Cm, Bk, and Cf.* Physical Review B, 1977. **15**(6): p. 2929-2942.
86. Pan, P. and A.B. Campbell, *The Characterization of Np<sub>2</sub>O<sub>5</sub>(c) and Its Dissolution in CO<sub>2</sub>-Free Aqueous Solutions at pH 6 to 13 and 25 °C.* Radiochimica Acta, 1998. **81**(2): p. 73-82.
87. Briggs, D. and M.P. Seah, *Auger and X-Ray Photoelectron Spectroscopy.* 2. ed. Practical Surface Analysis. Vol. 1. 1990, Chichester: John Wiley & Sons.
88. Briggs, D.G., John T., *Surface Analysis by Auger and X-Ray Photoelectron Spectroscopy.* 2003: IM Publications LLP.
89. Wong, K., S. Vongehr, and V.V. Kresin, *Work functions, ionization potentials, and in between: Scaling relations based on the image-charge model.* Physical Review B, 2003. **67**(3).
90. Schindler, M., et al., *XPS spectra of uranyl minerals and synthetic uranyl compounds. II: The O 1s spectrum.* Geochimica Et Cosmochimica Acta, 2009. **73**(9): p. 2488-2509.
-

91. Vandenborre, J., B. Grambow, and A. Abdelouas, *Discrepancies in Thorium Oxide Solubility Values: Study of Attachment/Detachment Processes at the Solid/Solution Interface*. Inorganic Chemistry, 2010. **49**(19): p. 8736-8748.
92. Hudry, D., et al., *Non-aqueous Synthesis of Isotropic and Anisotropic Actinide Oxide Nanocrystals*. Chemistry-a European Journal, 2012. **18**(27): p. 8283-8287.
93. Hudry, D., et al., *Controlled Synthesis of Thorium and Uranium Oxide Nanocrystals*. Chemistry-a European Journal, 2013. **19**(17): p. 5297-5305.
94. Albrecht, A.J., et al., *The crystal chemistry of four thorium sulfates*. Journal of Solid State Chemistry, 2011. **184**(7): p. 1591-1597.
95. Knope, K.E., et al., *Synthesis and characterization of thorium(IV) sulfates*. Inorganic Chemistry, 2011. **50**(17): p. 8621-8629.
96. Wilson, R.E., et al., *Structure of the homoleptic thorium(IV) aqua ion  $[Th(H_2O)_{10}]Br_4$* . Angewandte Chemie - International Edition, 2007. **46**(42): p. 8043-8045.
97. Aghabozorg, H., R.C. Palenik, and G.J. Palenik, *A ten-coordinate oxo-bridged thorium complex with an unusual coordination polyhedron*. Inorganica Chimica Acta, 1983. **76**(C): p. L259-L260.
98. Efremova, O.A., et al., *Crystal Structure of  $(H_3O)_4[(C_2H_5)_4N]_6 [Th_2Cl_4(H_2O)_{12}O]_3[Re_4Se_4(CN)_{12}]_4$* . Journal of Structural Chemistry, 2010. **51**(4): p. 782-784.
99. Takao, S., et al., *First Hexanuclear U-IV and Th-IV Formate Complexes - Structure and Stability Range in Aqueous Solution*. European Journal of Inorganic Chemistry, 2009(32): p. 4771-4775.
100. Knope, K.E. and L. Soderholm, *Plutonium(IV) Cluster with a Hexanuclear  $Pu_6(OH)_4O_4$  (12+) Core*. Inorganic Chemistry, 2013. **52**(12): p. 6770-6772.
101. Magini, M., A. Cabrini, and G. Scibona, *Structure of colloidal thorium solutions*. Acta Crystallographica Section A, 1975. **31**: p. S164-S164.
102. Magini, M., et al., *Structure of highly hydrolyzed thorium salt-solutions*. Acta Chemica Scandinavica Series a-Physical and Inorganic Chemistry, 1976. **30**(6): p. 437-447.
103. Haire, R.G., et al., *Aging of hydrous plutonium dioxide*. Journal of Electron Microscopy, 1971. **20**(1): p. 8.
104. Rothe, J., et al., *XAFS and LIBD investigation of the formation and structure of colloidal  $Pu(IV)$  hydrolysis products*. Inorganic Chemistry, 2004. **43**(15): p. 4708-4718.
105. Fujiwara, K., et al., *Solubility product of plutonium hydrous oxide and its ionic strength dependence*. Radiochimica Acta, 2002. **90**(12): p. 857-861.
106. Ikeda-Ohno, A., et al., *Hydrolysis of Tetravalent Cerium for a Simple Route to Nanocrystalline Cerium Dioxide: An In Situ Spectroscopic Study of Nanocrystal Evolution*. Chemistry-a European Journal, 2013. **19**(23): p. 7348-7360.
107. Ikeda-Ohno, A., et al., *Dinuclear complexes of tetravalent cerium in an aqueous perchloric acid solution*. Dalton Transactions, 2012. **41**(24): p. 7190-7192.
108. Strickert, R.G., D. Rai, and R.W. Fulton, *Effect of aging on the solubility and crystallinity of  $Np(IV)$  hydrous oxide*. ACS Symp. Ser., 1984. **246**: p. 136-145.
109. Cleveland, J.M. and T.F. Rees, *Characterization of plutonium in Maxey Flats radioactive trench leachates*. Science, 1981. **212**(4502): p. 1506-1509.
110. Dai, M., J.M. Kelley, and K.O. Buesseler, *Sources and migration of plutonium in groundwater at the Savannah River Site*. Environ. Sci. Technol., 2002. **36**(17): p. 3690-3699.
111. Ikeda-Ohno, A., et al., *Solution speciation of plutonium and Americium at an Australian legacy radioactive waste disposal site*. Environ. Sci. Technol., 2014. **48**(17): p. 10045-10053.
112. Husar, R., et al., *Formation of Neptunium(IV)-Silica Colloids at Near-Neutral and Slightly Alkaline pH*. Environmental Science & Technology, 2014. **49**(1): p. 665-671.
113. Charbonneau, C., R. Gauvin, and G.P. Demopoulos, *Nucleation and growth of self-assembled nanofibre-structured rutile ( $TiO_2$ ) particles via controlled forced hydrolysis of titanium tetrachloride solution*. J. Cryst. Growth, 2009. **312**(1): p. 86-94.

114. Cölfen, H., et al., *Particle growth kinetics in zirconium sulfate aqueous solutions followed by dynamic light scattering and analytical ultracentrifugation: Implications for thin film deposition*. Langmuir, 2002. **18**(9): p. 3500-3509.
115. Afanasiev, P., *Zr(IV) basic carbonate complexes as precursors for new materials: synthesis of the zirconium-surfactant mesophase*. Mater. Res. Bull., 2002. **37**(12): p. 1933-1940.
116. Hudry, D., et al., *Synthesis of transuranium-based nanocrystals via the thermal decomposition of actinyl nitrates*. Rsc Advances, 2013. **3**(40): p. 18271-18274.
117. Lloyd, M.H. and R.G. Haire, *A sol-gel process for preparing dense forms of PuO<sub>2</sub>*. Nuclear Applications, 1968. **5**(3): p. 114-&.
118. Nenoff, T.M., et al., *Synthesis and Low Temperature In Situ Sintering of Uranium Oxide Nanoparticles*. Chemistry of Materials, 2011. **23**(23): p. 5185-5190.
119. Roberts, K.E., et al., *Precipitation of crystalline neptunium dioxide from near-neutral aqueous solution*. Radiochimica Acta, 2003. **91**(2): p. 87-92.
120. Rousseau, G., et al., *Synthesis and characterization of nanometric powders of UO<sub>2+x</sub>, (Th,U)O<sub>2+x</sub> and (La,U)O<sub>2+x</sub>*. Journal of Solid State Chemistry, 2009. **182**(10): p. 2591-2597.
121. Strickert, R.G., D. Rai, and R.W. Fulton, *Effect of aging on the solubility and crystallinity of Np(IV) oxide*. ACS Symposium Series, 1984. **246**: p. 135-145.
122. Dzimitrowicz, D.J., P.J. Wiseman, and D. Cherns, *An electron-microscope study of hydrous thorium-dioxide ThO<sub>2</sub>nH<sub>2</sub>O*. Journal of Colloid and Interface Science, 1985. **103**(1): p. 170-177.
123. Nothwang, T.A., et al. *Particle size and morphology of MA-MOX precursor powders*. in *Proceedings of the 2008 Global Symposium on Recycling, Waste Treatment and Clean Technology, REWAS 2008*. 2008.
124. Keiser Jr, D.D., et al., *The development of metallic nuclear fuels for transmutation applications: Materials challenges*. JOM, 2008. **60**(1): p. 29-32.
125. Lebreton, F., et al., *Fabrication and characterization of americium, neptunium and curium bearing MOX fuels obtained by powder metallurgy process*. Journal of Nuclear Materials, 2012. **420**(1-3): p. 213-217.
126. Jovani-Abril, R., *Synthesis and characterization of nanocrystalline UO<sub>2</sub> ceramics*. 2014, Universidad de Santiago de Compostela (USC) and Institute for Transuranium Elements (ITU): Santiago de Compostela, Spain. p. 204.
127. Choppin, G.R., P. Pathak, and P. Thakur, *Polymerization and Complexation Behavior of Silicic Acid: A Review*. Main Group Metal Chemistry, 2008. **31**(1-2): p. 53-71.
128. Stumm, W., H. Huper, and R.L. Champlin, *Formulation of polysilicates as determined by coagulation effects*. Environmental Science & Technology, 1967. **1**(3): p. 221-227.
129. Efurud, D.W., et al., *Neptunium and plutonium solubilities in a Yucca Mountain groundwater*. Environmental Science & Technology, 1998. **32**(24): p. 3893-3900.
130. Buffle, J. and G.G. Leppard, *Characterization of aquatic colloids and macromolecules - 2. Key role of physical structures on analytical results*. Environmental Science & Technology, 1995. **29**(9): p. 2176-2184.
131. Weiner, B.B. and W.W. Tscharnuter, *Uses and abuses of photon-correlation spectroscopy in particle sizing*. ACS Symposium Series, 1987. **332**: p. 48-61.
132. Birdi, K.S., *Handbook of Surface and Colloid Chemistry*. third edition ed. 2009: CRC Press. 756.
133. Hunter, R.J., R.H. Ottewill, and R.L. Rowell, *Zeta Potential in Colloid Science*. 1981, Academic Press Limited: London.
134. Silva, R.J. and H. Nitsche, *Actinide environmental chemistry*. Radiochimica Acta, 1995. **70-1**: p. 377-396.
135. Jada, A., et al., *Adsorption and surface properties of silica with transformer insulating oils*. Fuel, 2002. **81**(9): p. 1227-1232.

136. Pettersson, A. and J.B. Rosenholm, *Adsorption of alkyltrimethylamine and alkyltrimethylphosphine oxides at curved aqueous solution/silica interfaces, studied using microcalorimetry*. Langmuir, 2002. **18**(22): p. 8436-8446.
137. Kim, J. and D.F. Lawler, *Characteristics of zeta potential distribution in silica particles*. Bulletin of the Korean Chemical Society, 2005. **26**(7): p. 1083-1089.
138. Cho, G., et al., *Characterization of surface charge and zeta potential of colloidal silica prepared by various methods*. Korean Journal of Chemical Engineering, 2014. **31**(11): p. 2088-2093.
139. Bergna, H.E. and W.O. Roberts, *Colloidal Silica: Fundamentals and Applications*. Surfactant Science Series. Vol. 131. 2005: CRC Press. 944.
140. Chorom, M. and P. Rengasamy, *Dispersion and zeta potential of pure clays as related to net particle charge under varying pH, electrolyte concentration and cation type*. European Journal of Soil Science, 1995. **46**(4): p. 657-665.
141. Franks, G.V., *Zeta potentials and yield stresses of silica suspensions in concentrated monovalent electrolytes: Isoelectric point shift and additional attraction*. Journal of Colloid and Interface Science, 2002. **249**(1): p. 44-51.
142. Baik, M.H. and S.Y. Lee, *Colloidal stability of bentonite clay considering surface charge properties as a function of pH and ionic strength*. Journal of Industrial and Engineering Chemistry, 2010. **16**(5): p. 837-841.
143. Elimelech, M., et al., *Particle Deposition and Aggregation: Measurement, Modelling and Simulation* 1998, Oxford: Elsevier. 464.
144. Hiemenz, P.C. and R. Rajagopalan, *Principles of Colloid and Surface Chemistry*. Third Edition ed. 1997, Boca Raton: CRC Press.
145. Israelachvili, J., *Intermolecular and Surface Forces*. Third Edition ed. 2011, London: Academic Press.
146. Zänker, H., S. Weiß, and C. Hennig, *On the stability of thorium(IV)-silica colloids, in Annual Report 2012 of the Institute of Resource Ecology*. 2013: Dresden-Rosendorf. p. 40.
147. Grebenshchikova, V.I. and Y.P. Davydov, *State of Pu(IV) in region of pH = 1.0 – 12.0 at a Plutonium concentration of  $2 \times 10^{-5}$  M*. Radiokhimiya, 1965. **7**: p. 191-195.
148. Vitorge, P. and C. Poinssot, *Comparing the chemical behaviours of Neptunium and Plutonium in natural ground-waters*. Actualite Chimique, 2005: p. 54-59.
149. Schmeide, K. and G. Bernhard, *Redox stability of neptunium(V) and neptunium(IV) in the presence of humic substances of varying functionality*. Radiochimica Acta, 2009. **97**(11): p. 603-611.
150. Denecke, M.A., K. Dardenne, and C.M. Marquardt, *Np(IV)/Np(V) valence determinations from Np L3 edge XANES/EXAFS*. Talanta, 2005. **65**(4): p. 1008-1014.
151. Clark, D.L., et al., *A multi-method approach to actinide speciation applied to pentavalent neptunium carbonate complexation*. New Journal of Chemistry, 1996. **20**(2): p. 211-220.
152. Clark, D.L., et al., *EXAFS studies of pentavalent neptunium carbonate complexes. Structural elucidation of the principal constituents of neptunium in groundwater environments*. Journal of the American Chemical Society, 1996. **118**(8): p. 2089-2090.
153. Ikeda-Ohno, A., et al., *Neptunium Carbonato Complexes in Aqueous Solution: An Electrochemical, Spectroscopic, and Quantum Chemical Study*. Inorganic Chemistry, 2009. **48**(24): p. 11779-11787.
154. Rothe, J., et al., *XAFS Investigation of the Structure of Aqueous Thorium(IV) Species, Colloids, and Solid Thorium(IV) Oxide/Hydroxide*. Inorganic Chemistry, 2002. **41**(2): p. 249-258.
155. Antonio, M.R., et al., *Neptunium redox speciation*. Radiochimica Acta, 2001. **89**(1): p. 17-25.
156. Ikeda-Ohno, A., et al., *Electrochemical and complexation behavior of neptunium in aqueous perchlorate and nitrate solutions*. Inorganic Chemistry, 2008. **47**(18): p. 8294-8305.

- 
157. Lam, D.J., A.P. Paulikas, and B.W. Veal, *X-ray photoemission spectroscopy studies of soda aluminosilicate glasses*. *Journal of Non-Crystalline Solids*, 1980. **42**(1-3): p. 41-47.
158. Lam, D.J., B.W. Veal, and A.P. Paulikas, *X-ray photoemission spectroscopy (XPS) study of uranium, neptunium, and plutonium oxides in silicate-based glasses*. *ACS Symposium Series*, 1983. **216**: p. 145-154.
159. Knoblich, B. and T. Gerber, *The arrangement of fractal clusters dependent on the pH value in silica gels from sodium silicate solutions*. *Journal of Non-Crystalline Solids*, 2001. **296**(1-2): p. 81-87.
160. Utsunomiya, S., et al., *Uraninite and fullerene in atmospheric particulates*. *Environmental Science & Technology*, 2002. **36**(23): p. 4943-4947.
161. Weyland, M. and P.A. Midgley, *Electron tomography*. *Materials Today*, 2004. **7**(12): p. 32-40.
162. Midgley, P.A., et al., *High-Resolution Scanning Transmission Electron Tomography and Elemental Analysis of Zeptogram Quantities of Heterogeneous Catalyst*. *Journal of Physical Chemistry B*, 2004. **108**(15): p. 4590-4592.
163. Mobus, G. and B.J. Inkson, *Three-dimensional reconstruction of buried nanoparticles by element-sensitive tomography based on inelastically scattered electrons*. *Applied Physics Letters*, 2001. **79**(9): p. 1369-1371.
164. Weyland, M. and P.A. Midgley, *Extending Energy-Filtered Transmission Electron Microscopy (EFTEM) into Three Dimensions Using Electron Tomography*. *Microscopy and Microanalysis*, 2003. **9**(6): p. 542-555.
165. Cakir, P., et al., *Surface reduction of neptunium dioxide and uranium mixed oxides with plutonium and thorium by photocatalytic reaction with ice*. *Journal of Physical Chemistry C*, 2015. **119**(3): p. 1330-1337.
166. Kunze, P., et al., *The influence of colloid formation in a granite groundwater bentonite porewater mixing zone on radionuclide speciation*. *Journal of Contaminant Hydrology*, 2008. **102**(3-4): p. 263-272.
167. Schaefer, T., et al., *Nanoparticles and their influence on radionuclide mobility in deep geological formations*. *Applied Geochemistry*, 2012. **27**(2): p. 390-403.
168. Wold, S. and T.E. Eriksen, *Diffusion of lignosulfonate colloids in compacted bentonite*. *Applied Clay Science*, 2003. **23**(1-4): p. 43-50.
169. Holmboe, M., S. Wold, and M. Jonsson, *Colloid diffusion in compacted bentonite: microstructural constraints*. *Clays and Clay Minerals*, 2010. **58**(4): p. 532-541.
170. Wold, S. and T. Eriksen, *Diffusion of humic colloids in compacted bentonite*. *Physics and Chemistry of the Earth*, 2007. **32**(1-7): p. 477-484.
171. Kurosawa, S., et al., *The effect of montmorillonite partial density on the role of colloid filtration by a bentonite buffer*. *Journal of Nuclear Science and Technology*, 2006. **43**(5): p. 605-609.
172. Kitatsuji, Y., T. Kimura, and S. Kihara, *Reduction behavior of neptunium(V) at a gold or platinum electrode during controlled potential electrolysis and procedures for electrochemical preparations of neptunium(IV) and (III)*. *Journal of Electroanalytical Chemistry*, 2010. **641**(1-2): p. 83-89.
173. Schmeide, K., et al., *Neptunium(IV) complexation by humic substances studied by X-ray absorption fine structure spectroscopy*. *Radiochimica Acta*, 2005. **93**(4): p. 187-196.
174. Li, Y.D., Y. Kato, and Z. Yoshida, *Electrolytic preparation of neptunium species in concentrated carbonate media*. *Radiochimica Acta*, 1993. **60**(2-3): p. 115-119.
175. Ueno, K. and A. Saito, *Solubility and absorption-spectra of carbonate complex of pentavalent neptunium*. *Radiochemical and Radioanalytical Letters*, 1975. **22**(2): p. 127-133.
176. Eriksen, T.E., et al., *Solubility of redox-sensitive radionuclides Tc99 and Np-237 under reducing conditions in neutral to alkaline solutions*. 1993, Swedish Nuclear Fuel and Waste Management Co.: Stockholm.
-

177. Pratopo, M.I., H. Moriyama, and K. Higashi, *Carbonate complexation of neptunium(IV) and analogous complexation of groundwater uranium*. *Radiochimica Acta*, 1990. **51**(1): p. 27-31.
178. Hagan, P.G. and Clevelan.Jm, *Absorption spectra of neptunium ions in perchloric acid solution*. *Journal of Inorganic & Nuclear Chemistry*, 1966. **28**(12): p. 2905-&.
179. Kim, J.I., et al., *Untersuchung der Übertragbarkeit von Labordaten (Löslichkeiten und Sorptionskoeffizienten) auf natürliche Verhältnisse am Beispiel von Gorleben Aquifer-Systemen*. 1999, Forschungszentrum Karlsruhe: Karlsruhe.
180. Sjoblom, R. and J.C. Hindman, *Spectrophotometry of neptunium in perchloric acid solutions*. *Journal of the American Chemical Society*, 1951. **73**(4): p. 1744-1751.
181. Varlashkin, P.G., et al., *Electrochemical and spectroscopic studies of neptunium in concentrated aqueous carbonate and carbonate-hydroxide solutions*. *Radiochimica Acta*, 1984. **35**(2): p. 91-96.
182. Wester, D.W. and J.C. Sullivan, *Electrochemical and spectroscopic studies of neptunium(VI),-(V) and -(IV) in carbonate-bicarbonate buffers*. *Journal of Inorganic & Nuclear Chemistry*, 1981. **43**(11): p. 2919-2923.
183. Panak, P.J., et al., *Complexation of Cm(III) with aqueous silicic acid*. *Radiochimica Acta*, 2005. **93**(3): p. 133-139.
184. O'Brien, R.W. and L.R. White, *Electrophoretic mobility of a spherical colloidal particle*. *Journal of the Chemical Society, Faraday Transactions 2: Molecular and Chemical Physics*, 1978. **74**(0): p. 1607-1626.
185. Newville, M., *Fundamentals of XAFS*. 2004, Consortium for Advanced Radiation Sources, University of Chicago, Chicago, IL, U.S.A.
186. Matz, W., et al., *ROBL - a CRG beamline for radiochemistry and materials research at the ESRF*. *Journal of Synchrotron Radiation*, 1999. **6**: p. 1076-1085.
187. Hennig, C., *Evidence for double-electron excitations in the L-3-edge x-ray absorption spectra of actinides*. *Physical Review B*, 2007. **75**(3).
188. Hennig, C., S. Skanthakumar, and L. Soderholm, *Double photoexcitation of 2p and 4f electrons in curium*. *Journal of Electron Spectroscopy and Related Phenomena*, 2010. **180**(1-3): p. 17-20.
189. Ressler, T., *WinXAS: a program for X-ray absorption spectroscopy data analysis under MS-Windows*. *Journal of Synchrotron Radiation*, 1998. **5**: p. 118-122.
190. George, G.N.P., I. J., *EXAFSPAK, a suite of computer programs for analysis of X-ray absorption spectra*. 2000: Stanford.
191. Ankudinov, A.L., et al., *Real-space multiple-scattering calculation and interpretation of x-ray-absorption near-edge structure*. *Physical Review B*, 1998. **58**(12): p. 7565-7576.
192. Fuchs, L.H. and E. Gebert, *X-ray studies of synthetic coffinite, thorite and uranothorites*. *American Mineralogist*, 1958. **43**(3-4): p. 243-248.
193. Lander, G.H. and M.H. Mueller, *Magnetically induced lattice distortions in actinide compounds*. *Physical Review B*, 1974. **10**(5): p. 1994-2003.
194. Kelly, S.D., D. Hesterberg, and B. Ravel, *Analysis of Soils and Minerals - Using X-ray Absorption Spectroscopy*, in *Methods of Soil Analysis*. 2008, Soil Science Society of America: Madison, U.S.A. p. 387-468.
195. Koningsberger, D.C., et al., *XAFS spectroscopy; fundamental principles and data analysis*. *Topics in Catalysis*, 2000. **10**(3-4): p. 143-155.
196. Koningsberger, D.C. and R. Prins, *X-ray Absorption: Principles, Applications, Techniques of EXAFS, SEXAFS, and XANES*. *Chemical Analysis: A Series of Monographs on Analytical Chemistry and Its Applications* (ed. D.C. Koningsberger and R. Prins. Vol. 92. 1987: John Wiley & Sons. 688.
197. *NIST X-ray Photoelectron Spectroscopy Database*, N.I.o.S.a. Technology, Editor. 2003, Standard Reference Data Group: Gaithersburg, U.S.A.
198. Shirley, D.A., *High-resolution x-ray photoemission spectrum of valence bands of gold*. *Physical Review B*, 1972. **5**(12): p. 4709-&.
-



199. Langmuir, D., *Eh-pH determination*, in *Procedures in Sedimentary Petrology*, R.E. Carver, Editor. 1971, Wiley: New York. p. 597-634.

---

## List of Figures

Figure 1. Worldwide cumulative minor actinide discharges .....	1
Figure 2. Schematic illustration of model nuclear waste repository with example of environmental groundwater composition .....	3
Figure 3. An(IV) cluster structures (A) and An(IV) colloids (B) in the nanoscale.....	4
Figure 4. Schematic illustration of dispersed nanoparticles with selected chemical and physical parameters.....	5
Figure 5. Solubility of neptunium(IV) in dependence on carbonate/bicarbonate concentration .....	8
Figure 6. UV-vis absorbance spectra of $1.4 \cdot 10^{-3}$ M Np(IV) solutions as a factor of time and carbonate and silicate concentrations .....	10
Figure 7. PCS autocorrelation functions and CONTIN deconvolutions (light-intensity weighted PSD) of Np(IV)-silica colloids .....	11
Figure 8. UV-vis absorption spectra of Np(IV) in diluted carbonate environment and sample appearance in dependence on time .....	14
Figure 9. Normalized Np L <sub>III</sub> -edge XANES spectra for Np(IV) samples.....	15
Figure 10. EXAFS of Np(IV) precursor solution, wet Np(IV) precipitate and NpO <sub>2</sub> powder.....	16
Figure 12. TEM data of re-dispersed Np(IV) precipitate – NpO <sub>2</sub> NCs.....	20
Figure 13. TEM data of Np(IV) precipitate isolated from dispersion– NpO <sub>2</sub> NCs.....	21
Figure 14. Survey XPS of NpO <sub>2</sub> NCs .....	22
Figure 15. Np 4 <i>f</i> core level XPS of Np(IV) precipitate. ....	23
Figure 16. XPS O 1 <i>s</i> core level of NpO <sub>2</sub> NCs. ....	25
Figure 17. PSD of NpO <sub>2</sub> NCs agglomerates in dependence on time .....	26
Figure 18. HR-TEM micrographs of NpO <sub>2</sub> NCs in dependence on aging time .....	28
Figure 19. UV-visible absorption spectra of hydrolyzed Np(IV) and NpO <sub>2</sub> NCs in solution in dependence on time .....	29
Figure 20. SAED patterns of Np(IV) precipitates in dependence on aging time.....	31
Figure 22. HR-TEM micrograph of NpO <sub>2</sub> NC and sub-nanometer-sized Np(IV)-species .....	34
Figure 23. Time dependence of the SLI in different silicate samples.....	41
Figure 24. Visible absorption spectra of Np(IV) in dependence on initial silica concentration .....	43

---

Figure 25. Dependence of SLI and particle size (PCS) of the Np(IV) silica particles on the initial concentration of silicic acid .....	44
Figure 26. Time dependence of the SLI for three systems of Np(IV) silica colloids in dependence on silica content .....	45
Figure 27. Hydrodynamic diameter of Np(IV) silica colloids in dependence on time and the initial silicate concentration (PCS) .....	46
Figure 28. Size distribution of Np(IV) silica colloids in dependence on initial silicate concentration and time .....	47
Figure 29. Zeta-potential of Np(IV) nanoparticles in dependence on pH and silicate content .....	49
Figure 30. Normalized Np L <sub>III</sub> -edge XANES spectrum for Np(IV) silica nanoparticles. ....	53
Figure 31. EXAFS of Np(IV) silica colloids.....	54
Figure 32. Survey XPS of potentially long term stabilized Np(IV) silica colloids.....	55
Figure 33. Np 4 <i>f</i> core level XPS of long term stabilized Np(IV) silica colloids.....	56
Figure 34. XPS O 1 <i>s</i> core level of aged Np(IV) silica colloids.....	57
Figure 35. TEM data of silica-enriched Np(IV) silica colloids.....	58
Figure 36. HAADF-STEM micrograph and EDX of silica-enriched Np(IV) silica colloid.....	59
Figure 37. TEM data of silica-poor Np(IV) silica particle .....	60
Figure 38. Morphology of silica-enriched Np(IV) silica colloid structure versus structure silica-poor Np(IV) silica particle .....	61
Figure 39. TEM data of silica-enriched Np(IV) silica colloids.....	62
Figure 40. HAADF-STEM micrographs of aged Np(IV) silica colloids in different magnifications: (A) 160kx and (B) 1300kx.....	63
Figure 41. TEM-Micrograph of potentially long-term stabilized Np(IV) silica colloids.....	64
Figure 42. HR-TEM of potentially long-term stabilized Np(IV) silica colloids .....	65
Figure 43. Visible absorption spectra of Np in dependence on valency in acidic solution.....	70
Figure 44. Visible-NIR absorption spectra of tetravalent Np in slightly alkaline solution .....	71
Figure 45. Principle scheme of electrolysis cell setup.....	73
Figure 46. The structure of colloid interface .....	75
Figure 47. X-ray absorption spectrum of Np(V).....	77
Figure 48. Visible absorption spectra of a Np(IV) silica sample before and after ultrafiltration...	81

---

Figure 49. Normalized Np L<sub>III</sub>-edge XANES spectra of Np(IV) silica nanoparticle solution and Np(V) reference..... 81

Figure 50. XPS Np 4*f* core level spectra of NpO<sub>2</sub> NCs and stabilized Np(IV) silica colloids..... 82

Figure 51. XPS Np 4*f* core level spectra of NpO<sub>2</sub> NCs and stabilized Np(IV) silica colloids..... 82

Figure 52. Appearance of Np(IV) sample in dependence on time after initial hydrolysis..... 83

Figure 53. UV-vis spectra of Np redox states and corresponding sample appearance in dependence on sample composition and pH..... 83

---

## List of tables

Table 1. Colloid characterization by nephelometry, ultracentrifugation (5 h, 100 000 × g) and ultrafiltration (5-kDa).....	8
Table 2. XANES edge positions at the Np L <sub>III</sub> -edge for the spectra given in Figure 9 and a Np(V) reference (Figure 49). The edge position is defined at the first inflection point.....	15
Table 3. EXAFS structural parameters obtained from theoretical curve fitting.....	17
Table 4. Electron BE of core level in Np-precipitate at near-neutral pH at 1253.6 eV.....	24
Table 5. Electron BEs of Np 4 <i>f</i> <sub>7/2</sub> core level for a series of Np-oxides with different valencies..	24
Table 6. Coherences in PSD, UV-vis absorbance of Np(IV) solutions and sediment occurrence .	30
Table 7. Molar Si/Np ratio of the Np(IV) silica colloids in dependence on the initial Si and Np solution concentrations [Si] and [Np] .....	42
Table 8. Isoelectric points of actinide oxide particles, An(IV) silica colloids and silica particles.	50
Table 9. XANES edge position at Np L <sub>III</sub> -edge.....	53
Table 10. Structural parameters of Np(IV) silica particles [(Np,Si)O <sub>n</sub> (OH) <sub>4-n</sub> ·xH <sub>2</sub> O] <sup>4-2n-(4-n)</sup> obtained from theoretical curve fitting.....	54
Table 11. Electron BE of long-term stabilized Np(IV) silica colloids at 1253.6 eV .....	56
Table 12. XAS samples. Details of sample preparation for the XAS experiments .....	79

---

## Publications

Selected work shown herein was presented to the scientific community on several conferences and workshops and published in peer-reviewed journals.

### Journal articles

*Intrinsic formation of nanocrystalline neptunium dioxide in the neutral aqueous condition relevant to deep geological repositories*

in Chemical Communications, 2015. 51(7): p. 1301-1304., IF<sub>2014</sub> 6.7

DOI: 10.1039/C4CC08103J

*Formation of neptunium(IV)-silica colloids at near-neutral and slightly alkaline pH*

in Environmental Science and Technology, 2014. 49(1): p. 665-671., IF<sub>2014</sub> 5.4

DOI: 10.1021/es503877b

### Presentations

*Investigation into the formation of Np(IV) silica colloids*

Oral presentation on Migration Conference 2013, Brighton, U.K.

*Intrinsic formation of Np(IV) nanoparticles: from Np(IV)-silica colloids and NpO<sub>2</sub> nanocrystals.*

Poster presentation on Plutonium Futures 2014, ANS, Las Vegas, U.S.A.

*A kinetic insight into the formation of NpO<sub>2</sub> nanocrystals*

Poster presentation on Advanced Techniques in Actinide Spectroscopy (ATAS), 2014, Dresden, Germany

*Investigation into the formation of Np(IV) silica colloids*

Poster presentation on Advanced Techniques in Actinide Spectroscopy (ATAS), 2012, Dresden, Germany

Rewarded with **Best Poster Award** by selection of workshop participants

---

## Acknowledgements

Each successfully finished scientific work always started with a great sparking initiative idea:

I want to thank emeritus professor Dr. Gert Bernhard, former director of the Institute of Radiochemistry, and retired Dr. Harald Zänker, former supervisor in the division of surface processes, for providing me with the actinide silica topic. I gratefully thank them for the scientific freedom to start my ambitious investigation into neptunium chemistry, which was successfully completed under the supervision of Prof. Dr. Thorsten Stumpf, director of Institute of Resource Ecology and the heads of the divisions of Surface Chemistry, Dr. Vinzenz Brendler and Chemistry of the f-elements, Dr. Atsushi Ikeda-Ohno.

I want to thank the referees of the dissertation Prof. Dr. Thorsten Stumpf and Prof. Dr. Alexander Eychmüller, Physical Chemistry, Department Chemistry and Food Chemistry, TU Dresden.

In the following I want to gratefully thank,

- Dr. Vinzenz Brendler for steady scientific encouragement and support at any time
- Dr. Atsushi Ikeda-Ohno for his enthusiastic engagement and support during my last year in PhD as a member of the recently founded division chemistry of the f-elements and for sharing the same passion of neptunium chemistry
- Dr. René Hübner for his expertise, encouragement and the outstanding support with TEM measurements, which were crucial to the discovery of intrinsic formed  $\text{NpO}_2$  NCs
- Dr. Christoph Hennig and Stephan Weiss for their great competence and pragmatic support in EXAFS and colloid experiments
- Dr. Harald Zänker for ambitious discussions about controversial An(IV) chemistry and for his great expertise in PCS
- Dr. Stefan Facsko and Benjamin Schreiber, Institute of Ion Beam Physics, HZDR for fruitful discussions about bonding natures and electronic structures of nanomaterial and especially Stefan for the XPS measurements
- Martin Ihrig for assistance in investigating the zetapotential and PSD of Np(IV) particles and everybody else who contributed important puzzle pieces that were essential to the comprehensive understanding of this work.

A successful thesis in actinide chemistry is not possible without nuclear safety, bureaucracy and motivation: therefore, I gratefully thank the team safety group of Mrs. Heim and technician staff for pragmatic support in radiochemistry laboratories, especially Anette Rumpel, Christa Müller,

Sylvia Gürtler, Steffen Henke, Dirk Falkenberg and retired Bernd Hiller who all supported me in laboratory and constantly filled the interior of HZDR's glove boxes with inert gas but ensured that the exterior was constantly saturated with great humoristic atmosphere.

Bureaucracy and other difficulties were counterbalanced by the outstanding support of Jana Gorzitze, Ronny Berndt and other colleagues who shared the ups and downs during coffee breaks, Friday-Fridays, wine/beer seminars, especially Dr. Tobias Günther, Dr. Robin Steudtner, Jérôme Kretzschmar, Björn Drobot, Dr. Katharina Müller, Dr. Harald Förstendorf, Dr. Carola Franzen, Dr. Satoru Tsushima, Dr. Erik Johnstone, Dr. Moritz Schmidt and all people whom I did not mention.

I could always count on my dear family and girlfriend Josephine for motivation, relentless support in any situation and the sometimes necessary diversion from work so new sparks could be ignited. Thank you all for that!



---

## **Versicherung**

Hiermit versichere ich, dass ich die vorliegende Arbeit ohne unzulässige Hilfe Dritter und ohne Benutzung anderer als der angegebenen Hilfsmittel angefertigt habe; die aus fremden Quellen direkt oder indirekt übernommenen Gedanken sind als solche kenntlich gemacht. Die Arbeit wurde bisher weder im Inland noch im Ausland in gleicher oder ähnlicher Form einer anderen Prüfungsbehörde vorgelegt.

Die vorliegende Arbeit wurde am Helmholtz-Zentrum Dresden-Rossendorf, Institut für Ressourcenökologie in der Zeit von Juni 2011 bis Dezember 2014 unter der wissenschaftlichen Betreuung von Herrn Prof. Dr. Thomas Stumpf, Herrn Dr. Vinzenz Brendler und Herrn Dr. Atsushi Ikeda-Ohno angefertigt.

Ich erkenne die Promotionsordnung der Technischen Universität Dresden Fakultät Mathematik und Naturwissenschaften vom 23.02.2011 in geänderter Fassung vom 15.06.2011 und 18.06.2014 an.

Dresden, den 07.07.2015

Richard Husar